2009

Feedforward control approach to precision trajectory design and tracking : Theory and application to nano-mechanical property mapping using Scanning Probe Microscope

Kyongsoo Kim
Iowa State University

Feedforward control approach to precision trajectory design and tracking :

Theory and application to nano-mechanical property mapping

using Scanning Probe Microscope

by

Kyongsoo Kim

A dissertation submitted to the graduate faculty

in partial fulfillment of the requirements for the degree of

DOCTOR OF PHILOSOPHY

Major: Mechanical Engineering

Program of Study Committee:
Qingze Zou, Major Professor
Atul Kelkar
Greg R. Luecke
Pranav Shrotriya
Balaji Narasimhan

Iowa State University

Ames, Iowa

2009

DEDICATION

I would like to dedicate this thesis to my wife Sunki and my son Youngsung for their endless support with love and cheering to my study. I would like to thank my advisor Qingze Zou for his sincere guidance of my work.

TABLE OF CONTENTS

LIST OF TABLES

LIST OF FIGURES

ABSTRACT

The output tracking problem has been extensively studied. The linear system case has been addressed by B. A. Francis. (1976) by converting the tracking problem to a regulator problem. Such an approach was later extended to nonlinear systems by A. Isidori. et al. (1990). On the feedforward control side, the stable inversion theory solved the challenging output tracking problem and achieved exact tracking of a given desired output trajectory for nonminimum phase systems (linear and nonlinear). The obtained solution is noncausal and requires the entire desired trajectory to be known a priori. This noncausality constraint has been alleviated through the development of the preview-based inversion approach, which showed the precision tracking can be achieved with a finite preview of the future desired trajectory, and the effect of the limited future trajectory information on output tracking can be quantified. Moreover, optimal scan trajectory design and control method provided a systematic approach to the optimal output-trajectory-design problem, where the output trajectory is repetitive and composed of pre-specified trajectory and unspecified trajectory for transition that returns from ending point to starting point in a given time duration.

This dissertation focuses on the development of novel inversion-based feedforward control technique, with applications to output tracking problem with tracking and transition switchings, possibly non-repetitive. The motivate application examples come from atomic force microscope (AFM) imaging and material property measurements. The raster scanning process of AFM and optimal scan trajectory design and control method inspired the repetitive output trajectory tracking problem and attempt to solve in frequency domain. For the output tracking problem, especially for the AFM, there are several issues that have to be addressed. At first, the shape of the desired trajectory must be designed and optimized. Optimal output-trajectory-design problem provided a systematic approach to design the desired trajectory by minimizing the total input energy. However, the drawback is that the desired trajectory

becomes very oscillatory when the system dynamics such as the dynamics of the piezoelectric actuator in AFM is lightly damped. Output oscillations need to be small in scanning operations of the AFM. In this dissertation, this problem is addressed through the pre-filter design in the optimal scan trajectory design and tracking framework, so that the trade off between the input energy and the output energy in the optimization is achieved. Secondly, the dissertation addressed the adverse effect of modeling error on the performance of feedforward control. For example, modeling errors can be caused in process of curve fitting.

The contribution of this dissertation is the development of novel inversion based feedforward control techniques. Based on the inversion-based iterative learning control (S. Tien. et al. (2005)) technique, the dissertation developed enhanced inversion-based iterative control and the model-less inversion-based iterative control. The convergence of the iterative control law is discussed, and the frequency range of the convergence as well as the effect of the disturbance/noise to signal ratio is quantified. The proposed approach is illustrated by implementing them to high-speed force-distance curve measurements by using atomic force microscope (AFM). Then the control approach is extended to high-speed force-volume mapping. In high-speed force-volume mapping, the proposed approach utilizes the concept of signal decoupling-superimposition and the recently-developed model-less inversion-based iterative control (MIIC) technique. Experiment of force-volume mapping on a Polydimethylsiloxane (PDMS) sample is presented to illustrate the proposed approach. The experimental results show that the mapping speed can be increased by over 20 times.

CHAPTER 1. Introduction

Most of the control issues might be finding a way how to regulate a plant, or a way how to track given reference trajectory. Then the secondary question might be the issues of stability and the tracking error. This dissertation seeks a systematic feedforward control method in frequency domain for high-speed precision output trajectory tracking. The control method is tested and implemented in atomic force microscope. Then the proposed feedforward control technique is applied in material property measurement. The complexity mostly due to their vibrational dynamics and nonlinearities is handled by the notion of system inversion and iterative learning control. To reduce modeling error effect in inversion of the system, iterative control technique is blended on top of the system inversion technique. The system inversion with iterative control technique is implemented for the repetitive trajectory tracking first. Then the testing trajectory is extended to non-repetitive trajectory. The precision trajectory tracking requirements and convergence conditions are analyzed. Application to force volume measurement shows that the proposed control technique can improve the measurement speed up to 20 times faster than the commercial device.

1.1 Study of system inversion and iterative control technique: a brief review

Several approaches have been proposed to tackle the output tracking problem. One of the major groups tried to track output trajectory by feedback control which is called regulation theory. The output regulation was achieved by B. A. Francis. (1976) for the linear system, and A. Isidori. et al. (1990) for the nonlinear system. The uncertainty of the desired trajectory was considered by A. Serrani. et al. (2001). A benefit of the approach based on regulation theory was the easiness of the controller design by solving a set of matrix differential equation. However, asymptotic tracking of the desired trajectory was a major advantage in a sense of robustness and disadvantage in tracking precision with

respect to its speed. And also designing nonlinear regulator is still challenging because of the difficulty in solving the first order partial differential equations. In contrast to regulation theory, the system inversion theory (R. M. Hirschorn. (1979); M. Silverman. (1969)) achieves exact output tracking of minimum-phase system. Since the conventional system inversion theory generates unbounded input for the nonminimum-phase system, implementation of the theory was limited. This limitation was solved by the development of the stable inversion theory (Devasia, S. et al. (1996, 1998); L. R. Hunt et al. (1996)). Despite the stable inversion theory achieves exact output trajectory tracking for minimum/nonminimum phase system, the performance of the stable-inversion feedforward approach can be limited by the modeling error and/or disturbance effects.

Iterative learning control(ILC) is an approach to improve the system performance that operates repetitively. Based on the concept of practice, learning controllers corrects the performance of a system on a given trajectory by learning process. Major benefit of the learning control is the effectiveness of implementation over a system that cannot be modeled accurately. With a feedback controller alone, the identical task generates the same tracking error in every repeated trial. In contrast, a learning controller can use the information from the previous executions to improve the tracking performance in the next execution. First ILC was introduced by M. Uchiyama. (1978) and Arimoto et al. (1984). And the ILC was further developed by many researchers later (S. Kawamura. (1988); C. Atkeson. (1986); P. Bondi et al. (1988)). It has been shown that iterative learning control (ILC) is quite efficient in tracking repetitive trajectories (R. Horowitz. et al. (1991); K. Krishnamoorthy. et al. (2004); M. R. Graham. et al. (2006); L. Moore. et al. (2000)). Limits, however, exist in conventional ILC designs (M. Verwoerda. et al. (2006)) because causal controllers were used in these designs. As a result, the noncausality (i.e., the “preview” of the future desired trajectory as well as the predicted output of the system) was not exploited to improve the tracking, particularly for nonminimum-phase systems (M. Verwoerda. et al. (2006)). Such a limit is alleviated by ILC in frequency domain (J. Ghosh. et al. (2002); S. Tien. et al. (2005)).

1.2 Precision tracking for periodic and non-periodic trajectory using ILC

Conventional iterative learning control (ILC) technique starts from modeling of the plant. Based on the assumption that the model is not accurate, the ILC develops the iterative updating law with the proper choice of iterative learning gain. However, there are two challenges. Time consumption for learning process, which is a main drawback of the ILC, depends on the model accuracy and its updating law, especially depends on iterative learning gain. In contrast to the major advantage of ILC that the ILC is used for any system that the model is not correct, convergence condition for the frequency domain ILC analyzed by S. Tien. et al. (2005) showed that the modeling phase error should be less than $\pi/2$ for the bounded convergence. And also the smaller the iterative learning gain, the more precise convergence is achieved with the consumption of longer learning process. Inspired by the inversion-based iterative control (IIC) technique by S. Tien. et al. (2005), the research effort to remove the convergence condition for modeling phase variation resulted in invention of enhanced inversion-based iterative control (EIIC) technique by separation of the iterative control law in magnitude from the iterative control law in phase. The EIIC mitigates the convergence condition batter than IIC and the EIIC techniques utilize the noncausality to improve the tracking precision, as illustrated in (Y. Wu. et al. (2007)). However, their performance depends on the quality of the system dynamics model, and the modeling process as the preparation process of the ILC is time-consuming and prone to errors. As the another evolution of the EIIC, model-less inversion based iterative learning control (MIIC) technique is invented and removed modeling process completely. Experimental results show that the MIIC technique can be effectively implemented into the output trajectory tracking problem with the complete knowledge of the repetitive desired trajectory. The MIIC control techniques extended from the repetitive trajectory tracking to non-repetitive trajectory tracking problem in force volume mapping application. The non-periodic trajectory problem is shown in switching motion based force-volume mapping mode that we proposed. The vertical trajectory of the measurement probe motion for the force volume mapping is decoupled into the element trajectory. The inverse inputs achieved from the MIIC control technique for each element trajectory are superimposed to track non-periodic sampling point tracking trajectory and periodic force curve measurement trajectory. The experimental results reveal efficacy of the proposed control technique.

1.3 Dissertation overview

The rest of this dissertation is organized as follows. In chapter 2, two issues encountered in the design and track of repetitive scan trajectories are addressed. The first arising issue is how do we systematically determine the desired trajectory. The repetitive trajectory inspired by the raster scan motion of the AFM, which is composed of active scan trajectory that is pre-specified by user, and transition section that brings the end of active scan states to the origin of the active scan states, is tested. The main designing problem lies on finding transition trajectory, boundary states and the resulting input that tracks the desired trajectory exactly. Based on stable inversion theory, optimal scan trajectory design and control technique (OSDC, H. Perez. et al. (2004)) presented an analytical approach by minimizing input energy. Despite the OSDC technique gives an systematic approach of the transition trajectory design, unacceptable large output oscillations for the low damped system such as piezo actuators and flexible structures, that, in turn, shortens the life span of mechanical systems like piezo actuators, must be treated properly. This problem is analyzed mathematically and suggest a solution in terms of output energy minimization by differently penalizing each frequency component. The second arising issue is about the model uncertainty and its correction. In this case, the model uncertainty includes the uncertainty of the system dynamics, the disturbances (e.g., sensor noise), and the errors from the modeling process (e.g., curve fitting the experimental frequency response to obtain a low-order transfer function). This chapter propose a novel enhanced inversion-based iterative control (EIIC) method, and integrate it with the OSDC technique. This EIIC algorithm extends the inversion-based iterative control algorithm proposed in literature. (S. Tien. et al. (2005)). The optimal scan trajectory and the optimal control input, obtained from the OSDC technique, are used as the desired trajectory and the initial input in the EIIC algorithm, respectively. Then the control technique is implemented in high-speed adhesion force measurement, and shows that output oscillations during the transition section can be minimized and the output tracking errors caused by model uncertainties are dramatically reduced. In chapter 3, the EIIC is implemented to achieve high-speed force-curve measurement on a commercial atomic force microscope (AFM), through the measurement of time-dependent properties (e.g., elastic modulus) of poly(dimethylsiloxane) (PDMS) as an example. The measured values of the elastic modulus are compared with the results obtained from the dynamic mechanical analysis (DMA) test of the PDMS. In

chapter 4, model-less inversion-based iterative control (MIIC) technique which eliminates the need for the dynamics model is proposed for high-speed precise repetitive output tracking while further enhances the output tracking performance. Two types of trajectories are used to evaluate the tracking performance with comparison to the IIC algorithm: triangular trajectories and band-limited white-noise type of trajectories. Experimental results show that precise output tracking is achieved in both cases, whereas the IIC algorithm failed to track the complicated band-limited white-noise trajectories. Moreover, the MIIC algorithm is also implemented to compensate-for the hysteresis effect when tracking large-range triangle trajectory at high-speed. Experimental results show that precise output tracking can also be achieved. In chapter 5, MIIC technique is extended to high-speed force-volume mapping on atomic force microscopy (AFM). Achieving high-speed force-volume mapping is challenging in three-fold: (1) high-speed force-curve measurement at each sample point, (2) rapid transition of the probe from one sample point to the next while compensating for the sample topography difference between the two points, with no sliding of the probe on the sample, and (3) seamless integration of the above two motions. The main contribution of the chapter is the development of a novel switching-motion based force-volume mapping mode. The proposed mode consists of stop-and-go switching motion in lateral scanning, synchronized with the vertical probe motion switching between force-curve measurement and point-to-point output transition. To achieve precision tracking in the lateral scanning as well as in the vertical switching motion, we propose to combine the utilization of the notion of superimposition with the recently-developed MIIC technique. The a priori sample topography knowledge is utilized in the proposed mode, which can be obtained by using high-speed AFM imaging technique. To implement switching-motion based force-volume mapping mode, first, the sample topography is simplified by digitizing the sample surface by its measurement point. Secondly, the vertical motion of the probe is decoupled as the summation of elements of force-curve measurement and elements of output transition at one sample point. Then, the MIIC technique is implemented to obtain the control input to track the element force-curve, and to achieve the element output-transition (at one point) as well. Finally, the control is achieved by superimposing these element inputs together appropriately. In superimposition of the vertical motion for the output transition from one sample point to the next, generated non-repetitive trajectory tracking problem is treated in terms of superimposition. The proposed method is illustrated

by implementing it in experiments to obtain force-volume mapping of a Polydimethylsiloxane (PDMS) sample. The experimental results show that the speed of force-volume mapping can be achieved over 20 times with large lateral scan range (40 μm) and high spatial resolution (128 number of force curves measured per scan line). Finally, the conclusion is given in chapter 6.

CHAPTER 2. A New Approach to Scan-Trajectory Design and Track: AFM Force Measurement Example

A paper published in ASME Journal of Dynamic Systems, Measurement and Control

Abstract

In this chapter, two practical issues encountered in the design and track of scan trajectories are studied: One issue is related to the large output oscillations occurring during the scanning, and the other one is the effect of modeling errors on the trajectory tracking. Output oscillations need to be small in scanning operations, particularly for lightly-damped systems such as piezoelectric actuators and flexible structures. Moreover, modeling errors are ubiquitous in practical applications. The proposed approach extends the recently-developed optimal scan trajectory design and control method, by introducing the pre-filter design into the design to reduce the output oscillations. Furthermore, a novel enhanced inversion-based iterative control (EIIC) algorithm is proposed. The EIIC algorithm is then integrated with the optimal scan trajectory design method to compensate for the effect of modeling errors on the scanning. The convergence of the iterative control law is discussed, and the frequency range of the convergence is quantified. The proposed approach is illustrated by implementing it to high-speed adhesion force measurements by using atomic force microscope (AFM). Simulation and experimental results are presented and discussed to demonstrate the efficacy of the proposed approach.

2.1 Introduction

In this chapter, two issues encountered in the design and track of scan trajectories are addressed: One issue is related to the large output oscillations occurring during the scanning, and the other one is the

effect of modeling errors on the trajectory tracking. It is noted that scanning operations are involved in many applications, including (a) the nano-scale topography imaging (e.g. R. Wiesendanger. (1994)) and material property measurements (i.e., (Kees O. van Werf. et al. (1994)) using atomic force microscope (AFM); (b) the scanning mechanism on MEMS-based micro-mirrors (F. Filhol. et al. (2005); F. Zimmer. et al. (2005)); (c) the quick-return mechanisms and cams in manufacturing (R.-F. Fung. et al. (2000)); and (d) the manufacturing process in rapid prototyping (S. Huang. et al. (2005)). A typical scanning operation consists of two sections: (1) the active-scan section, during which a pre-specified, desired output trajectory must be tracked precisely, followed by (2) the output transition section, during which the output needs to be returned to a setpoint value (for repeating the active scan in the next cycle). While the desired output for the active-scan section is usually specified by the application, the output trajectory during the transition section is often not specified and thereby can be designed to optimize the performance. In this chapter, we introduce the design of a prefilter into the recently-developed optimal scan trajectory design and control (OSDC) technique (H. Perez. et al. (2004)), with an aim to minimize the output oscillations during the transition section. Moreover, a novel inversion-based iterative control algorithm is introduced and integrated with the OSDC technique to further improve the tracking precision. The proposed technique is illustrated by implementing it on high-speed adhesion force measurements using AFM. Simulation and experimental results are presented and discussed to demonstrate the efficacy of the proposed method to compensate for the two practical issues.

The development of the OSDC technique (H. Perez. et al. (2004)) provides a systematic approach to solve the scanning problem. Although previous methods based on trajectory smoothing and polynomial function optimizations (C. Cloet. et al. (2001); A. Piazzi. et al. (2000); A. V. Dowd. et al. (2000)) can lead to an acceptable output tracking, these methods require the user to choose an initial set of acceptable output trajectories. Such a choice, however, was *ad hoc*, and can be challenging. On the contrary, in the OSDC technique, the optimal output trajectory was found as the result of an input-energy minimization process, thereby eliminating the need to choose the initial output trajectories. Moreover, conventionally the optimal output-transition problem was converted and solved as the optimal state-transition problem, by first, pre-specifying the boundary states at the beginning and the end of the output-transition section, and secondly, performing an optimal state transition (e.g., (F. L.

Lewis. et al. (1995))). However, the boundary states are usually unknown *a priori*, thereby the choice of the boundary states was *ad hoc*, and may not be optimal. Instead, in the OSDC technique, such unknown boundary states (i.e., the initial and the final states of the output-transition section) were treated as the variables to be optimized when minimizing the total input energy during the entire scanning period (i.e., both active-scan and output-transition are included) (H. Perez. et al. (2004)). The efficacy of the OSDC technique has been experimentally demonstrated also (H. Perez. et al. (2004)).

Challenges, however, may arise when implementing the OSDC technique in practices. First, the obtained optimal output transition trajectory may contain large oscillations during the output-transition section, not desirable for systems such as piezo actuators and flexible structures. This is because excessive output oscillations may induce overheating of the structure and fatigues of the materials, which in turn, shortens the life span of mechanical systems like piezo actuators. The dynamics of these systems tends to have one or multiple lightly-damped (i.e., high-Q) resonant peak(s), characterized by a dramatic gain increase accompanied by a rapid phase drop. The dramatic gain increase at the resonant peak(s) implies that the output transition can be achieved with a small amount of input energy, provided that the main frequency components of the input are concentrated around the resonant peak(s), i.e., a minimal input-energy transition. Such an input was obtained with the OSDC technique via the minimization of the input-energy (H. Perez. et al. (2004)). However, the low-damping at the resonant peak implies that when such a minimal-energy input is used, large output oscillations will occur during the transition section. This is illustrated in this chapter by using a piezotube actuator as an example. Secondly, output errors can also be generated due to the model uncertainty. Model uncertainty generally exist in practices, because of the uncertainty of the system dynamics, the disturbances (e.g., sensor noise), and the errors from the modeling process (e.g., curve fitting the experimental frequency response to obtain a low-order transfer function). Although such model-uncertainty-caused output errors can be reduced, in general, by augmenting a feedback controller to the optimal feedforward control input (H. Perez. et al. (2004); Q. Zou. et al. (2004)), there are applications where the feedback compensation is challenging, because of, for example, the lack of sensors (H. Perez. et al. (2004)), or the nature of the operation. One example for the latter case (adhesion force measurements using AFM) is discussed in this chapter. Therefore, there exists a need to account for these two practical issues (output oscillations

and model uncertainty) in the design and track of optimal scan trajectories.

The contribution of this chapter is a systematic approach to account for the above two practical issues in the design and tracking of scan trajectories. First, we introduce the prefilter design into the OSDC technique (H. Perez. et al. (2004)). It is shown that by applying the OSDC technique to the augmented system (i.e., the prefilter followed by the system to be controlled), the minimization of the input-energy (in the original OSDC technique (H. Perez. et al. (2004))) can be transformed to the minimization of the output-energy with frequency-dependent weights. Therefore, the minimization of output-oscillations and its trade-off with the minimization of input-energy can be achieved in the OSDC technique framework through the design of the prefilter. Secondly, to further reduce the output errors caused by the model uncertainty, we propose a novel enhanced inversion-based iterative control (EIIC) method, and integrate it with the OSDC technique. This EIIC algorithm extends the inversion-based iterative control algorithm proposed in Ref. (S. Tien. et al. (2005)). The optimal scan trajectory and the optimal control input, obtained from the OSDC technique, are used as the desired trajectory and the initial input in the EIIC algorithm, respectively. We illustrate the proposed technique by implementing it to the high-speed adhesion-force measurements using AFM. Simulation and experimental results are presented to show that output oscillations during the transition section can be minimized, and the output tracking errors caused by model uncertainties are dramatically reduced. As a result, high-speed force measurements can be achieved by using the proposed technique.

2.2 Iteration-based Output Transition with Output Oscillation Minimization

2.2.1 Problem Formulation

Consider a linear, time invariant square system $G(s) = C(sI - A)^{-1}B$ with $\{A,\ B,\ C\}$ in

$$\dot{x}(t) = Ax(t) + Bu(t), \quad y(t) = Cx(t), \tag{2.1}$$

where $x(t) \in \Re^n$ is the state, $u(t) \in \Re^p$ is the input, $y(t) \in \Re^p$ is the output. The system is square (i.e., the number of the inputs is the same as that of the outputs), controllable, and has a well defined relative degree $\rho := [\rho_1, \rho_2, \cdots, \rho_p]^T$ (e.g. (A. Isidori (1995))). Then the scanning problem is stated as follows:

The Scanning Problem Given 1) the time section for the output transition $[t_0,\ t_i)$, and 2) a desired output trajectory $y_{track}(t)$ to be tracked during the tracking section $t_i \le t < t_f$ (see Fig. 2.1), find a bounded pair of desired input-state trajectories, $\{u_{ff}(\cdot),\ x_{ref}(\cdot)\}$, such that:

1. The reset of the system output priori to the next scan is achieved during the transition section,

$$\begin{aligned} y_{tran}(t_i) \equiv y(t_i) = Cx_{ref}(t_i) = \lim_{t \to t_i^-} y_{track}(t) \equiv \bar{y} \\ y_{tran}(t_f) \equiv y(t_f) = Cx_{ref}(t_f) = \lim_{t \to t_0^+} y_{track}(t) \equiv \underline{y}; \end{aligned} \tag{2.2}$$

2. The system dynamics is satisfied by the desired input-state trajectories, i.e.,

$$\dot{x}_{ref}(t) = Ax_{ref}(t) + Bu_{ff}(t), \ \text{ for } t \in [t_i,\ t_f]; \tag{2.3}$$

3. Exact output tracking is achieved during the tracking section, i.e.,

$$y_{track}(t) = Cx_{ref}(t), \ \text{ for } t \in [t_i,\ t_f]. \tag{2.4}$$

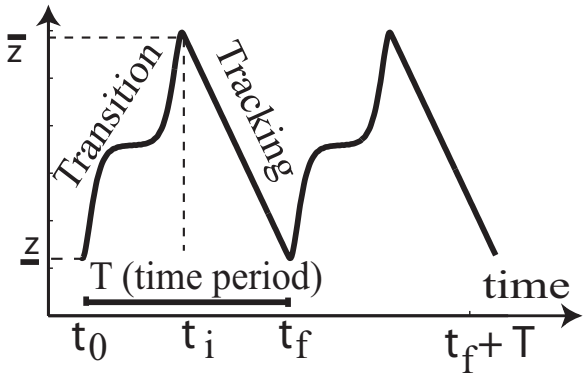

Figure 2.1 The scan trajectory consisting of a transition section (for $t_0 \le t < t_i$) and a tracking section (for $t_i \le t < t_f$), where the desired output trajectory is pre-specified for the tracking section only.

Acco unt of Practical Issues in the Scanning Problem In Ref. (H. Perez. et al. (2004)), the OSDC technique was proposed to systematically design the scan trajectory, and to obtain the corresponding control input. The OSDC technique integrated the system-inversion theory with the optimal control technique. In this chapter, we seek, through the extension of the OSDC technique (H. Perez. et al. (2004)), to

- minimize the output oscillations during the transition section through the design of a prefilter in the OSDC technique; and
- compensate for the output errors caused by model uncertainties through the integration with a novel EIIC technique.

2.2.2 Optimal Scan Trajectory Design with Frequency-Weighted Output-Energy Minimization

First, we will show that the minimization of the output oscillations during the transition section can be obtained through the design of a prefilter in the OSDC technique (H. Perez. et al. (2004)). Then secondly, the scanning problem will be solved by applying the OSDC technique to the augmented system consisting of the prefilter followed by the plant dynamics.

Prefilter Design for Output-Oscillation Minimization We consider augmenting an invertible prefilter of compatible dimension, $G_{pre}(s) \in \mathbb{C}^{p\times p}$, to the original system $G(s)$, and minimizing the energy of the input $u_a(t)$ to the augmented system (see Fig. 2.2), $G_a(s) \equiv G_{pre}(s)G(s)$,

$$J_{total} = \int_{t_0}^{t_f} u_a(t)^T u_a(t) dt. \tag{2.5}$$

In Eq. (2.5), a unit weight $R = \mathbf{I} \in \Re^{p\times p}$ is chosen to simplify the presentation (Similar derivation can be carried out for non-unit weights).

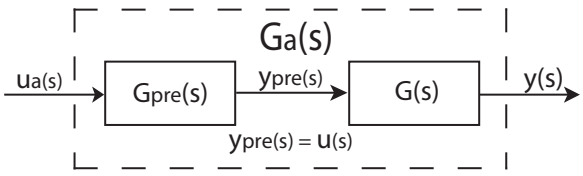

Figure 2.2 The augmented system consisting of a prefilter $G_{pre}(s)$ followed by the plant dynamics $G(s)$

The following development will show that minimizing the above cost function (2.5) is equivalent to minimizing the output energy with a frequency-dependent weight (where the weight is specified by the prefilter $G_{pre}(s)$). We consider that the following input $\bar{u}_a(\cdot)$

$$\bar{u}_a(t) = u_a(t), \text{ for } t \in [t_0, t_f], \text{ and } \bar{u}_a(t) = 0, \text{ otherwise,} \tag{2.6}$$

is applied to the augmented system $G_a(s)$ with the same initial state when the the input $u(t)$ is applied, and denote the corresponding output as $\bar{y}(t)$. Then, the cost given by Eq. (2.5) can be rewritten as

$$J_{total} = \int_{t_0}^{t_f} \bar{u}_a(t)^T \bar{u}_a(t) dt = \int_{-\infty}^{\infty} \bar{u}_a(t)^T \bar{u}_a(t) dt, \tag{2.7}$$

and the output

$$\bar{y}(t) = y(t), \ \text{ for } t \in [t_0,\ t_f]. \tag{2.8}$$

By Parseval's Theorem (e.g., (W. Rudin (1966))), Equation (2.7) leads to

$$\begin{aligned}
J_{total} &= \int_{-\infty}^{\infty} \bar{u}_a(t)^T \bar{u}_a(t) dt = \int_{-\infty}^{\infty} \bar{u}_a(j\omega)^* \bar{u}_a(j\omega) d\omega \\
&= \int_{-\infty}^{\infty} \bar{y}_{pre}(j\omega)^* G_{pre}^{-1}(j\omega)^* G_{pre}^{-1}(j\omega) \bar{y}_{pre}(j\omega) d\omega \\
&\qquad (\text{by } \bar{y}_{pre}(j\omega) = G_{pre}(j\omega)\bar{u}_a(j\omega), \text{ and } G_{pre}(j\omega) \text{ being invertible, see Fig. 2.2.}) \\
&= \int_{-\infty}^{\infty} \bar{y}(j\omega)^* \left[G_{pre}^{-1}(j\omega) G^{-1}(j\omega)\right]^* \left[G_{pre}^{-1}(j\omega) G^{-1}(j\omega)\right] \bar{y}(j\omega) d\omega \\
&\qquad (\text{by } \bar{y}(j\omega) = G(j\omega)\bar{y}_{pre}(j\omega), \text{ and } G(j\omega) \text{ being invertible.}) \\
&\equiv \int_{-\infty}^{\infty} \bar{y}(j\omega)^* \mathbf{W}(j\omega) \bar{y}(j\omega) d\omega \quad (\mathbf{W}(j\omega) \equiv G_{pre}^{-1}(j\omega) G^{-1}(j\omega)),
\end{aligned} \tag{2.9}$$

where '*' denotes the complex conjugate operation. Note that the system $G(j\omega)$ is invertible by Assumption (i.e., the system $G(j\omega)$ is square and has a well-defined relative-degree), and the prefilter $G_{pre}(j\omega)$ is invertible by design. Therefore, the frequency-dependent weight $\mathbf{W}(j\omega)$ in Eq. (2.9) is positive-definite, andEquation (2.9) implies that minimizing the original cost J_{total} is equivalent to minimizing the output energy with an frequency-dependent weight $\mathbf{W}(j\omega)$ when the input is $\bar{u}_a(t)$. Combining with Eq. (2.8), this shows that such a minimization also leads to the minimization of the system output $y(t)$ (with the same frequency-dependent weight $\mathbf{W}(j\omega)$) when the input is $u_a(t)$. Particularly, the frequency weight $\mathbf{W}(j\omega)$ can be manipulated to minimize output oscillations during the output-transition section. This is achieved through the design of the prefilter $G_{pre}(j\omega)$. For example, by rendering the prefilter $G_{pre}(j\omega)$ small (i.e., $|G_{pre}^{-1}(j\omega)|$ large) around the resonant peak(s) of the plant dynamics $G(j\omega)$, a large weight $\mathbf{W}(j\omega) = |G_{pre}^{-1}(j\omega)G^{-1}(j\omega)|^2$ around the resonant peaks of the plant dynamics $G(j\omega)$ is used when minimizing the cost function (2.5). As a result, the components of the output energy around the resonant peak(s) are minimized, and the output oscillation during the

output-transition section tends to be minimized. This idea is illustrated in Sec. 2.3.

Optimal Scan Trajectory for the Augmented System (H. Perez. et al. (2004)) Next, the scanning problem is solved by applying the OSDC technique to the augmented system, $G_a(s) = G_{pre}(j\omega)G(j\omega) = C_a(sI - A_a)^{-1}B_a$, where the state matrices $\{A_a,\ B_a,\ C_a\}$ are the minimal realization of the transfer function matrix $G_a(s)$,

$$\dot{x} = A_a x + B_a u_a, \quad y = C_a x. \tag{2.10}$$

The idea is to I) split the cost (2.5) into the cost for output-tracking, J_{track}, and the cost for output-transition, J_{tran},

$$J_{scan} = \int_{t_0}^{t_i} u_a^T u_a dt + \int_{t_i}^{t_f} u_a^T u_a dt = J_{trans} + J_{track}, \tag{2.11}$$

and then II) find the input for the output-transition, $u_{tran}(t)$ for time $t \in [t_0,\ t_i]$, as well as the input for the output-tracking, $u_{track}(t)$ for time $t \in [t_i,\ t_f]$, as affine functions of the boundary state at the time instants t_0 (i.e., t_f) and t_i. The transition input $u_{tran}(t)$ is obtained by using the optimal state transition method (e.g., (F. L. Lewis. et al. (1995))), and the tracking input $u_{track}(t)$ is unique and obtained by using the stable-inversion technique. Subsequently, the optimal inputs, $u_{track}(t)$ and $u_{tran}(t)$, are obtained by I) substituting these two inputs (u_{tran} and u_{track} for the transition and the tracking section, respectively) back into Eq. (2.11) to present the cost function as a quadratic function of the boundary state; and then II) minimizing such a cost function to obtain the optimal boundary state. We summarize the results of the OSDC technique next. The readers are referred to Ref. (H. Perez. et al. (2004)) for details.

We start by transforming the state-space equation of the augmented system (2.10) into the *output-tracking form*: If the system has a well-defined relative degree, then there exist 1) a coordinate transformation, Φ,

$$x = \Phi \begin{bmatrix} \xi \\ \eta_s \\ \eta_u \end{bmatrix} \equiv \begin{bmatrix} \Phi_\xi, \Phi_{\eta_s}, \Phi_{\eta_u} \end{bmatrix} \begin{bmatrix} \xi \\ \eta_s \\ \eta_u \end{bmatrix} \tag{2.12}$$

and 2) an inverse input $u_a(t) = u_{ff}(t)$,

$$u_{ff}(t) = \widehat{B_s}\eta_s(t) + \widehat{B_u}\eta_u(t) + \widehat{B_\xi}\mathbb{Y}_d(t), \tag{2.13}$$

such that by using the state-transformation Φ and the inverse input $u_{ff}(t)$, the system (2.10) can be transformed into the following output tracking form

$$\dot{\xi} = \dot{\xi}_d(t), \tag{2.14}$$

$$\begin{bmatrix} \dot{\eta}_s \\ \dot{\eta}_u \end{bmatrix} = \begin{bmatrix} A_s & 0 \\ 0 & A_u \end{bmatrix} \begin{bmatrix} \eta_s \\ \eta_u \end{bmatrix} + \begin{bmatrix} B_s \\ B_u \end{bmatrix} \mathbb{Y}. \tag{2.15}$$

In Eq. (2.15), ξ is the vector of the output and its derivatives up to one order less than the relative degree ρ,

$$\xi \equiv \left[y_1, \dot{y}_1, \cdots, \frac{d^{\rho_1-1}y_1}{dt^{\rho_1-1}}, \cdots, \dot{y}_2, \cdots, \frac{d^{\rho_2-1}y_2}{dt^{\rho_2-1}}, \cdots, y_p, \dot{y}_p, \cdots, \frac{d^{\rho_p-1}y_p}{dt^{\rho_p-1}} \right]^T, \tag{2.16}$$

$\mathbb{Y}$ is given by

$$\mathbb{Y}(t) = \left[\xi^T, \frac{d^{\rho_1}y_1}{dt^{\rho_1}}, \frac{d^{\rho_2}y_2}{dt^{\rho_2}}, \cdots, \frac{d^{\rho_p}y_p}{dt^{\rho_p}} \right]^T, \tag{2.17}$$

and for given desired trajectory,

$$\xi_d \equiv \xi \left|_{y(t)=y_d(t),\cdots}\right., \quad \mathbb{Y}_d(t) \equiv \mathbb{Y}(t) \left|_{y(t)=y_d(t),\cdots}\right. \tag{2.18}$$

Equation (2.15) is called the *internal dynamics* of the system (2.10), and η_s and η_u are the stable part and the unstable part of the internal dynamics of the system, respectively, with all the eigenvalues of A_s on the open left half of the complex plane, and all the eigenvalues of A_u on the close right half of the complex plane, respectively. Then, the solution of the OSDC technique is given in the following Theorem 1 (H. Perez. et al. (2004)).

Theorem 1 *The optimal solution to minimize the cost function (2.9) for the scanning problem is given as follows,*

1. *The total cost (Eq. (2.9)) is minimized by the following boundary condition Ψ^*:*

$$\Psi^* = \begin{bmatrix} \eta_s(t_0)^* \\ \eta_u(t_i)^* \end{bmatrix} = \begin{cases} \Lambda^{-1}b, & \textit{if } \Lambda \textit{ is invertible}, \\ \Lambda^{\dagger}b, & \textit{otherwise} \end{cases} \tag{2.19}$$

where $\Lambda^{\dagger}$ is the pseudo-inverse (J. M. Ortega (1987)) of Λ with Λ specified as follows,

$$\begin{aligned} \Lambda &= \Lambda_{track} + \Lambda_{tran} \\ where \quad \Lambda_{track} &= \int_{t_0}^{t_i} P(t)^T P(t) dt \\ \Lambda_{tran} &= H_2^T G_{(t_i,t_f)}^{-1} H_2 \end{aligned} \tag{2.20}$$

In Eq. (2.20), G_{t_i,t_f} is the invertible controllability Gramian,

$$G_{(t_i,t_f)} = \int_{t_i}^{t_f} e^{A(t_f-\tau)} B R^{-1} B^T e^{A^T(t_f-\tau)} d\tau, \tag{2.21}$$

and

$$\begin{aligned} P(t) &= \left[\widehat{B_s} e^{A_s(t-t_0)} \quad \widehat{B_u} e^{-A_u(t_i-t)}\right] \\ H_2 &= \left[-W_{\eta_s} K_s + \Phi_{\eta_s},\ \Phi_{\eta_u} K_u - W_{\eta_u}\right] \\ \left[W_\xi, W_{\eta_s}, W_{\eta_u}\right] &= e^{A_a(t_f-t_i)} \Phi \\ K_s &= e^{A_s(t_i-t_0)} \\ K_u &= e^{-A_u(t_i-t_0)} \\ \Lambda_s &= \int_{t_0}^{t_i} e^{A_s(t_i-\tau)} B_s \mathbb{Y}_d(\tau) d\tau \\ \Lambda_u &= -\int_{t_0}^{t_i} e^{-A_u(\tau-t_0)} B_u \mathbb{Y}_d(\tau) d\tau \end{aligned} \tag{2.22}$$

In Eq. (2.19), the term b is specified by

$$\begin{aligned} b &= b_{track} + b_{tran} \\ with \quad b_{trans} &= -H_2^T G_{(t_i,t_f)}^{-1} H_1 f \\ b_{track} &= -\int_{t_0}^{t_i} P(t)^T S(t) dt \end{aligned} \tag{2.23}$$

where H_2 and $P(t)$ are given by Eq. (2.20), and

$$\begin{aligned} H_1 &= \left[\Phi_\xi,\ \Phi_{\eta_u},\ -W_\xi,\ -W_{\eta_u}\right] \\ f &= \left[\xi_d(t_f),\ \Lambda_u,\ \xi_d(t_i),\ \Lambda_s\right]^T \end{aligned} \tag{2.24}$$

$$\begin{aligned} S(t) &= \widehat{B_s} \int_{t_0}^{t} e^{A_s(t-\tau)} B_s \mathbb{Y}(\tau) d\tau - \\ &\quad \widehat{B_u} \int_{t}^{t_i} e^{-A_u(\tau-t)} B_u \mathbb{Y}(\tau) d\tau + \widehat{B_\xi} \mathbb{Y}(t) \end{aligned} \tag{2.25}$$

2. *The optimal input $u^*_{ff}(t)$ is given by*

$$u^*_{ff}(t) = \begin{cases} u^*_{track}(t) = P(t)\Psi^* + S(t), & t_0 < t < t_i \\ u^*_{tran}(t), & t_i \le t \le t_f \end{cases} \tag{2.26}$$

where Ψ^*, $P(t)$, and $S(t)$ are given by Eq. (2.19, 2.22, 2.25), respectively, and

$$u^*_{tran}(t) = R^{-1}B^T e^{A^T(t_f-t)} G^{-1}_{(t_i,t_f)} \left[x^*(t_f) - e^{A_a(t_f-t_i)} x^*(t_i) \right] \tag{2.27}$$

with

$$\begin{aligned} x^*(t_f) &= \Phi \begin{bmatrix} \xi_d(t_f) \\ \eta^*_s(t_f) \\ \eta^*_u(t_f) \end{bmatrix} \\ x^*(t_i) &= \Phi \begin{bmatrix} \xi_d(t_i) \\ \eta^*_s(t_i) \\ \eta^*_u(t_i) \end{bmatrix} \\ \eta^*_s(t_i) &= K_s \eta^*_s(t_0) + \Lambda_s \\ \eta^*_u(t_f) &= K_u \eta^*_u(t_i) + \Lambda_u \end{aligned} \tag{2.28}$$

3. *The corresponding reference state x_{ref} is given by:*

$$x_{ref}(t) = \Phi \begin{bmatrix} \xi \\ \\ e^{A_s(t-t_0)}\eta_s(t_0)^* + \\ \int_{t_0}^{t} e^{A_s(t_i-\tau)} B_s \mathbb{Y}_d(\tau) d\tau \\ \\ e^{-A_u(t_i-t)}\eta_u(t_i)^* - \\ \int_{t}^{t_i} e^{-A_u(\tau-t_0)} B_u \mathbb{Y}_d(\tau) d\tau \end{bmatrix}, \tag{2.29}$$

for $t \in (t_0,\ t_i)$, and

$$x_{ref}(t) = e^{A_a(t-t_i)} x(t_i)^* + \int_{t_i}^{t} e^{A(t-\tau)} B u^*_{tran}(\tau) d\tau \tag{2.30}$$

for $t \in [t_i,\ t_f]$. ■

2.2.3 Enhanced Inversion-based Iterative Control (EIIC)

In general, the model-uncertainty-caused output-tracking errors can be compensated for by using iterative control approaches (J. Ghosh. et al. (2000); L. Moore. et al. (2000)): the initial input for the first iteration is set as the optimal control input to the original system $G(s)$, $\hat{u}^*_{ff}(j\omega) = G_{pre}(j\omega)u^*_{ff}(j\omega)$ (see Fig. 2.2), where the optimal input $u^*_{ff}(j\omega)$ is obtained from Theorem 1; and the desired output trajectory is set as,

$$y_d(t) = C_a x_{ref}(t), \tag{2.31}$$

where $x_{ref}(t)$ is the optimal state trajectory obtained in Eqs. (2.29, 2.30). Next, we present a novel enhanced inversion-based iterative control (EIIC) algorithm for SISO systems, based on the extension of the IIC technique proposed in (S. Tien. et al. (2005)). The EIIC algorithm is given in the frequency-domain as follows,

$$u_0(j\omega) = \hat{u}^*_{ff}(j\omega), \qquad k = 0, \tag{2.32}$$

$$\begin{cases} |u_k(j\omega)| &= |u_{k-1}(j\omega)| + \rho(\omega)\left|G_m^{-1}(j\omega)\right|\left[|y_d(j\omega)| - |y_{k-1}(j\omega)|\right] \\ \angle u_k(j\omega) &= \angle u_{k-1}(j\omega) + (\angle y_d(j\omega) - \angle y_{k-1}(j\omega)) \end{cases} \qquad k \geq 1, \tag{2.33}$$

where $y_k(\cdot)$ denotes the input obtained by applying the iterative input $u_k(\cdot)$ to the actual system in the k^{th} iteration. The convergence of the EIIC law (Eqs. (2.32, 2.33)) is given by the following lemma.

Lemma 1 *For any given frequency value ω, let both the actual dynamics of the system $G(j\omega)$ and its model $G_m(j\omega)$ be stable and hyperbolic (i.e., have no zeros on the $j\omega$ axis), and also let the dynamics uncertainty $\Delta G(j\omega)$ be given as*

$$\Delta G(j\omega) \;=\; \frac{G(j\omega)}{G_m(j\omega)} = \frac{|G(j\omega)|e^{j\angle G(\omega)}}{|G_m(\omega)|e^{j\angle G(\omega)}} \equiv |\Delta G(\omega)|\, e^{j\Delta\angle G(j\omega)}. \tag{2.34}$$

Then, the iterative control law (2.32, 2.33) converges at frequency ω to the desired input $u_d(j\omega) \equiv G(j\omega)^{-1}y_d(j\omega)$, i.e., $\lim_{k\to\infty} u_k(j\omega) = u_d(j\omega)$, or equivalently,

$$\lim_{k\to\infty} |u_k(j\omega)| = |u_d(j\omega)|, \;\; \textit{and} \;\; \lim_{k\to\infty} \angle u_k(j\omega) = \angle u_d(j\omega),$$

if and only if the iterative coefficient $\rho(j\omega)$ is chosen as

$$0 < \rho(\omega) < \rho_{sup}(\omega) \equiv \frac{2}{|\Delta G(j\omega)|} \tag{2.35}$$

Proof: We first show that $\lim_{k\to\infty}|u_k(j\omega)| = |u_d(j\omega)|$ when the iterative coefficient $\rho(\omega)$ is chosen as in Eq. (2.35). Note that Eq. (2.33) can be rewritten as

$$\begin{aligned}
|u_{k+1}(j\omega)| - |u_d(j\omega)| &= |u_k(j\omega)| - |u_d(j\omega)| + \rho(\omega)\left|G^{-1}(j\omega)\right|[|y_d(j\omega)| - |y_k(j\omega)|] \\
&= |u_k(j\omega)| - |u_d(j\omega)| - \rho(\omega)\left|G^{-1}(j\omega)\right||G_a(j\omega)|[|u_k(j\omega)| - |u_d(j\omega)|] \\
&= [1-\rho(\omega)|\Delta G(j\omega)|][|u_k(j\omega)| - |u_d(j\omega)|] \\
&\quad\vdots \\
&= [1-\rho(\omega)|\Delta G(j\omega)|]^{k+1}[|u_0(j\omega)| - |u_d(j\omega)|]
\end{aligned} \tag{2.36}$$

Note that both $u_0(j\omega)$ (given by Eq. (2.32)) and $u_d(j\omega)$ are bounded, thus Eq. (2.36) shows that $\lim_{k\to\infty}|u_{k+1}(j\omega)| - |u_d(j\omega)| = 0$, if and only if $\lim_{k\to\infty}[1-\rho(\omega)|\Delta G(j\omega)|]^k = 0$, or equivalently,

$$|1-\rho(\omega)|\Delta G(j\omega)|| < 1. \tag{2.37}$$

Therefore, the range of $\rho(\omega)$ to guarantee the convergence of the magnitude part of the iterative control input (Eq. (2.35)), is obtained directly from Eq. (2.37). Next, the convergence of the phase part of the iterative control input can be verified directly from Eq. (2.33): since $\angle y_d(j\omega) = \angle G(j\omega) + \angle u_d(j\omega)$, and $\angle y_k(j\omega) = \angle G(j\omega) + \angle u_k(j\omega)$. Thus Eq. (2.33) can be rewritten as

$$\begin{aligned}
\angle u_{k+1}(j\omega) &= \angle u_k(j\omega) + (\angle y_d(j\omega) - \angle y_k(j\omega)) \\
&= \angle u_k(j\omega) + (\angle u_d(j\omega) + \angle G(j\omega) - \angle u_k(j\omega) - \angle G(j\omega)) \\
&= \angle u_d(j\omega)
\end{aligned} \tag{2.38}$$

Equation (2.38) shows that $\angle u_k(j\omega) = \angle u_d(j\omega)$ for all $k \geq 1$. This completes the proof. ■

Remark 1 *The iterative law (2.32, 2.33) extends the following inversion-based iterative control (IIC) law in (S. Tien. et al. (2005); Y. Wu. et al. (2007)),*

$$u_k(j\omega) = u_{k-1}(j\omega) + \rho(\omega)G_a^{-1}(j\omega)[y_d(j\omega) - y_{k-1}(j\omega)], \ \ (k \geq 1), \tag{2.39}$$

in two aspects: 1). The following phase condition needed for the convergence of the IIC law (2.39) is removed (in the EIIC law (2.33)): the size of the phase uncertainty must be less than $\pi/2$ (i.e., $|\Delta\angle G(j\omega)| < \pi/2$) for the IIC law (2.39) to converge (S. Tien. et al. (2005)); therefore, the frequency

range of the convergence is increased in the proposed EIIC law (2.32, 2.33); and 2). the range of the iterative coefficient $\rho(\omega)$ for convergence is also increased—for any nonzero phase uncertainty, the upper bound of the iterative coefficient $\rho(\omega)$ in the EIIC law (Eq. (2.35)) is larger than the upper bound of the iterative coefficient $\rho(\omega)$ in the IIC law (2.39), $\rho(j\omega) < 2\cos(\Delta G(j\omega))/|\Delta G(j\omega)|$.

Remark 2 *We note that the convergence of the phase part of the iterative control input is achieved after only one iteration, $k = 1$. However, in practical implementations, updating the phase of the iterative control input throughout the iteration process is desirable to remove the effects of disturbance and noise on the control input.*

We further note that the iterative control input is applied to the system as a feedforward control input, thus potential instability issues of the entire control system (controller plus the system dynamics) as encountered in feedback-control case is avoided. When the effect of noise is considered, it can be shown that the noise-caused input error at given frequency ω is bounded above by the ratio of the noise level to the system gain at the frequency ω. This is given by the following Corollary:

Corollary 1 *Let the conditions in Lemma 1 be satisfied, and consider that the system output $\tilde{y}(\cdot)$ is effected by measurement noise $y_n(\cdot)$ as*

$$\tilde{y}(t) = y(t) + y_n(t). \tag{2.40}$$

Then, for measurement noise bounded above by a frequency-dependent constant $\varepsilon(\omega)$ at any given frequency ω, $|y_n(j\omega)|_2 \leq \varepsilon(\omega)$, the error in the iteration control input is bounded as:

$$\lim_{k\to\infty}\Big||u_k(j\omega)| - |u_d(j\omega)|\Big| \leq |G^{-1}(j\omega)|\varepsilon(\omega) \tag{2.41}$$

$$|\angle u_k(j\omega) - \angle u_d(j\omega)| \leq \tan^{-1}\frac{\varepsilon(\omega)}{|y_d(j\omega)|}, \quad \textit{for } \forall k \geq 1. \tag{2.42}$$

Proof The proof is similar to the proof of Lemma 1 and is omitted. ■

Remark 3 *Corollary 1 provides a basic guideline to determine the frequency range over which the EIIC law should be implemented in practices: The EIIC law should be applied at frequencies where both the system gain $|G(j\omega)|$ and the size of the output (frequency components) are large enough when compared to the system noise level.*

2.3 Example: AFM Adhesion-Force Measurement

We illustrate the proposed optimal scan trajectory design and control technique by implementing it to the adhesion-force measurement using an AFM system (Dimension 3100, Veeco Inc.). We start by describing the operation of adhesion force measurement.

2.3.1 Adhesion-Force Measurement

Adhesion-Force Measurement Operation: To measure the adhesion force using AFM, the cantilever is driven by a piezoelectric actuator to approach and touch the sample surface till the cantilever deflection (i.e., the probe-sample interaction force) reaches the setpoint value (see Fig. 2.3). Then the piezoelectric actuator retraces to withdraw the cantilever from the sample surface and broke-out the probe-sample bonding. The adhesion force is then measured as the probe-sample interaction force at the break-out point, which is obtained from the cantilever deflection (B. Cappella. et al. (1999))(indicated as F_{adh} in Fig. 2.3). Such force-curve measurement using AFM enables the study of properties of a wide variety of materials at submicro- to nano- scale, making it a critical tool in areas such as materials science and biomedical imaging (e.g., (H.-J. Butt. et al. (2005); M. D. Louey. et al. (2001))).

Maintaining a constant pulling-up rate of the cantilever, or equivalently, a constant time-gradient of the pulling-up force, is critical in adhesion-force measurement. This is because the variations of the pulling-up rate (i.e., a non-zero acceleration of the pulling-up motion) will introduce extra external force to the probe-sample interaction, i.e., the non-zero acceleration implies a non-equilibrium force condition during the pulling-up (i.e., retrace) process, resulting in measurement errors in the obtained adhesion force. Currently, force-curve are measured on commercial AFM by simply driving the *z*-axis piezo actuator driven with the desired trajectory (i.e., a triangle trajectory) scaled by the DC-Gain of the *z*-axis AFM dynamics (called *DC-Gain method* in the following). Such an open-loop, DC-Gain method can maintain a constant pulling-up rate when the operation speed is slow, thereby the *z*-axis AFM dynamics is not excited. As the pulling-up rate is increased, however, the dynamics of the piezo actuator and the cantilever (along with the mechanical structure in between) can be excited, resulting in the dynamics-induced variations in the pulling-up rate. Therefore, the AFM dynamics effect must

be accounted for to achieve high-speed adhesion-force measurement.

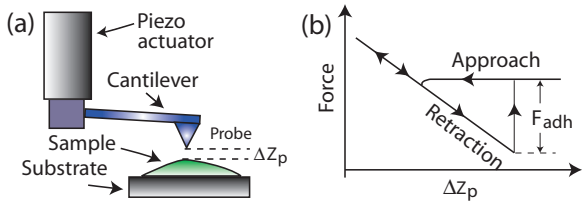

Figure 2.3 The scheme of AFM adhesion-force measurement (a), and a schematic drawing of the force-distance curve (b) to measure the adhesion force (denoted as F_{adh} in (b)).

Achieving high-speed force-curve measurement, however, is challenging. Feedback control approaches for force-curve measurements, by using the cantilever deflection signal as the feedback signal, are hindered by the following challenges: 1) The deflection signal is unchanged (i.e., close to zero) during the pushing-in (load) period until the probe "snaps" into the sample (B. Cappella. et al. (1999)). The "snap-in" point, however, is difficult to predict in practice and thereby unknown *a priori*; 2) The sample-probe break-out point during the pulling-up (unload) section is material dependent (B. Cappella. et al. (1999)), and thereby unknown in general also; and 3) To achieve high-speed force-curve measurements, the dynamics of the probe along with the associated mechanical structure must be accounted for in the controller design. However, such a dynamics can vary significantly whenever a probe is re-mounted or replaced. These feedback-control related issues, however, are avoided in the proposed feedforward control technique.

Finally, we note that High-speed measurement of adhesion force is needed in many applications. For example, to study the viscoelastic properties of a material, a maping of the adhesion force over the sample area needs to be obtained. This amounts to acquiring force curves at each location while scanning the sample in a rastern pattern (O. H. Willemsen. et al. (1998, 2004)), which is called the *force-volume* measurement. Thus, high-speed adhesion force is needed to achieve high-throughput in such force-volume measurement. Rapid adhesion force measurement is also needed to study the dependence of the adhesion force on the pulling-up rate (S.-J. Marrink. et al. (1998)).

Use of the Proposed Control Approach We note that the control objectives for adhesion-force measurement are: 1) During the approach section, the deflection signal needs to quickly reach the desired value without induced oscillations; and 2) During the retrace section, a constant pulling-up rate must be maintained. These control objectives were achieved by using the OSDC technique: The problem of adhesion-force measurement was solved as a scanning problem, where the approaching (load) section was mapped to the transition section, and the retrace (pull-up) section was mapped to the trajectory tracking section, respectively. Then the proposed EIIC algorithm was applied to further improve the positioning precision in the experiments.

2.3.2 Implementation of the Optimal Output Tracking Technique

Dynamics Modeling of AFM The dynamics of the AFM system with the input voltage to the vertical z-axis piezoelectric actuator to the cantilever deflection output was modeled experimentally using a dynamic signal analyzer (DSA) (Hewlett Packard 356653A). The cantilever was carefully lowered to establish a stable tip-sample contact with a samll load force (i.e., cantilever deflection value, tuned by using the AFM software). Then a small sinusoidal signal (with an amplitude of 40 mV) was generated by using the DSA and sent to the piezoelectric actuator. Then the measured deflection signal was sent back to the DSA and used to construct the frequency response of the AFM dynamics from the piezo actuator to the cantilever. The obtained frequency response, as shown in Fig. 2.4 (a), captured the AFM dynamics within the frequency range $\omega \in [0,\ 4.4]$ KHz. The following transfer function model, $G(s)$ was obtained via curve fitting the experimental frequency response, as compared in Fig. 2.4,

$$G(s) = \frac{d(s)}{u(s)} = K\frac{\prod_{q=1}^{4}(s-z_q)}{\prod_{r=1}^{6}(s-p_r)}. \tag{2.43}$$

In Eq. (2.43), the gain $K = 1.7398$, the zeros $z_q = \{18.9965, -0.0045 \pm 0.8948i, 0.0030\}$, the poles $p_r = \{-0.0170 \pm 2.2798i, -0.0041\ \ \pm 0.9097i, -0.8294, 0.0031\}$, and the unit of the Laplace variable is $rad/10^{-4}$ sec. (to reduce the numerical computation errors).

Note that our objective was to compensate for the AFM dynamics (from the piezo actuator to the cantilever) during high-speed adhesion force measurements, thus the transfer function in Eq. (2.43) should capture and only capture such an AFM dynamics. This was ensured by the experimental condition dur-

ing the modeling: the continuous contact of the cantilever with the sample was maintained during the entire experimental modeling process, and the sample material (silicon) was hard, thereby the obtained frequency response were mainly due to the dynamics from the piezoelectric actuator to the cantilever. Moreover, we also note that the first resonant frequency of the cantilever used in the experiments was at 20 KHz, over four times higher than the model frequency range of 4.4 KHz. Therefore, the frequency response in Fig. 2.4 captured the dynamics of the piezo actuator along with the mechanical connections from the piezo actuator to the cantilever. Particularly the dominant resonant peak at $\sim$3.6 KHz in Fig. 2.4 was due to the piezo actuator. Similar experimental approach has been used before in (S. Tien. et al. (2005)) for compensating for the vibrations caused by the cross-axis dynamics coupling (from x-axis to the z-axis) of a piezotube actuator. The efficacy of such a modeling approach was demonstrated in experiments (S. Tien. et al. (2005)).

Prefilter design To minimize output oscillations, a notch-filter type of prefilter $G_{pre}(s)$ was designed to counteract (i.e., cancel) the two dominant resonant peaks of the AFM dynamics captured in the model $G(s)$ at 1.4 KHz and 3.6 KHz, respectively:

$$G_{pre}(s) = \frac{s^2 + 5.198}{s^2 + 7.6s + 5.198} \; \frac{s^2 + 0.8275}{s^2 + 0.9097s + 0.8275} \tag{2.44}$$

The Laplace variable in Eq. (2.44) is in $rad/10^{-4}s$, and the bode plot of the augmented system model (the prefilter followed with the AFM dynamics model, see Fig. 2.2) is shown in Fig. 2.4 (b).

Implementation of the OSDC Technique The optimal control input to reduce the output oscillations, and the corresponding optimal output trajectory were obtained by applying the OSDC technique to the augmented system, $G_a(s) = G_{pre}(s)G(s)$. The state-space model of the augmented system, $G_a(s) = \{A_a, B_a, C_a\}$, was obtained from the state-space models of the prefilter, $G_{pre}(s) = \{A_{pre}, B_{pre}, C_{pre}\}$, and the AFM dynamics, $G(s) = \{A_{AFM}, B_{AFM}, C_{AFM}\}$, where

$$A_a = \begin{bmatrix} A_{AFM} & B_{AFM}C_{pre} \\ 0 & A_{pre} \end{bmatrix}, \quad B_a = \begin{bmatrix} B_{AFM} \\ B_{pre} \end{bmatrix}, \quad C_a = \begin{bmatrix} C_{AFM} & \mathbf{0} \end{bmatrix}. \tag{2.45}$$

Then the augmented system model (2.45) was used in the OSDC technique. The numerical results are omitted [1]. The readers are referred to Ref. (H. Perez. et al. (2004)) for the numerical results of a an

[1] The numerical results are available via email to kyongsoo@iastate.edu.

implementation of the OSDC algorithm .

Implementation of the EIIC algorithm The optimal output trajectory (see Eq. (2.31)) obtained from the OSDC technique were used as the desired trajectory in the EIIC algorithm, and the corresponding optimal control input was used as the initial control input for the first iteration (see Eq. (2.32)). To design the iterative coefficient $\rho(\omega)$ (see Eq. (2.33)), the magnitude uncertainty of the AFM frequency responses, as shown in Fig. 2.5, were estimated by measuring the frequency responses at two different sample locations with two different input levels (20mV, 40mV) respectively, and then finding the maximum magnitude difference among the four measured frequency responses. The upper bound of the iterative coefficient $\rho_{\text{sup}}(\omega)$ was computed according to Lemma 1. The value of the iterative coefficient $\rho(\omega)$ to maximize the convergence rate $|1-\rho(\omega)\Delta G(\omega)|$ was used in the experiments (see Fig. 2.5). Note that the chosen iterative coefficient is frequency-dependent.

To seek the converged control input for high-speed adhesion force measurements, the EIIC algorithm was applied to drive the AFM-probe under the *contact-mode condition*— the probe was in continuous-contact with the sample during the entire approach-retrace operation. This was achieved by adjusting the probe position to attain a small probe-sample force upon the control input was applied. The converged control input was applied later to measure the adhesion force by lifting up the probe above the sample before applying the control input. As a result, the probe broke out from sample during the retrace section.

We note that piezoelectric actuators present a non-trivial hysteresis effect in their input-output relation. Our recent work (Y. Wu. et al. (2007)) has shown that the IIC technique (see Eq. (2.39)) can be used to simultaneously compensate for both the vibrational dynamics and the hysteresis effects, provided that that the iterative coefficient ($\rho(\omega)$ in Eq. (2.39)) is chosen blow the upper bound. Such an upper bound, due to the hysteresis effect, is smaller than the bound for compensating for the dynamics effect only (Y. Wu. et al. (2007)). We expect that similar results hold for the EIIC technique. The focus of this chapter, however, is to propose the EIIC technique for dynamics compensation. Therefore, to eliminate

the hysteresis effects in the following experiments, the desired output trajectory of a small amplitude was chosen– as the hysteresis effect of piezo actuators is *range dependent* (Q. Zou. et al. (2004)), and becomes negligible when the displacement is small.

2.3.3 Simulation and Experimental Results & Discussion

Output Oscillation Reduction with the Designed Prefilter The optimal input to the piezoelectric actuator, obtained by applying the OSDC technique to the augmented system (the prefilter along with the AFM dynamics model, see Fig. 2.2), is compared with the control input obtained by applying the OSDC technique to the AFM dynamics model only in Fig. 2.6 (a). The scan rate (i.e., the rate of the whole approach-retrace operation) was 100 Hz, and the duty ratio R_d (i.e., the ratio of the tracking-section time over the entire approach-retrace period) was 50%. The corresponding optimal output trajectories obtained in the simulation, with and without the prefilter, are also compared in Fig. 2.6 (b). The simulation results show that by using the design of the prefilter, the output oscillations during the transition section were almost completely removed, whereas large output oscillations occurred when applying the OSDC technique to the AFM dynamics alone directly (see Fig. 2.6 (b)). Such large output oscillations is due to the utilization of the resonant peak of the AFM dynamics (see Fig. 2.4) in the OSDC technique to minimize the input-energy during the transition (approach) section—The oscillations were at the frequency of 3.5 KHz (close to the resonant peak of the AFM dynamics at 3.6 KHz, see Fig. 2.6). The corresponding input, with an input energy (2-norm of the entire approach-retrace period) at 0.6974, was almost zero during the transition section. The big "spike" at the beginning of the transition section, however, far exceeded the input voltage limit (see Fig. 2.6 (a)). Therefore, the optimal input obtained by using the OSDC technique directly on the AFM dynamics was not applicable in the experiments. On the contrary, with the designed prefilter, such large input "spike" as well as the large output oscillations were removed, while the input energy was only slightly increased by 14% (see Fig. 2.6). Therefore, the simulation results show that the output-oscillations can be frequency-weighted minimized through the design of a prefilter in the OSDC technique.

Experimental output tracking comparison The output tracking results, obtained by applying the control input to the piezoelectric actuator under the contact-mode condition (see Sec. 2.3.2), are com-

pared in Fig. 2.7 (left column) for the OSDC technique, the EIIC technique, and the DC-Gain method. Note the DC-Gain method does not account for the dynamics of the system, therefore the obtained output tracking quantitatively demonstrated the effects of the SPM dynamics on the positioning precision. In Fig. 2.7, the tracking results are shown for three different scan rates of 100 Hz, 260 Hz and 320 Hz, with the duty ratio at $R_d = 50\%,\ 50\%$, and 11%, respectively. The corresponding pulling-up rate were at 90.6 μm/s, 353.3 μm/s, and 724.8 μm/s, respectively (see Table 2.1). Note the transition (pulling-up) time was kept the same for the scan rate of 320 Hz and 260 Hz. This is because when applying the control input to the adhesion-force measurement later, the pulling-up time must be long enough to allow the cantilever's in-air free oscillations (governed by the cantilever dynamics) to decay away after the probe-sample break-out (see Fig. 2.8). In the right column of Fig. 2.7, the tracking errors obtained with the above three methods are also compared. The manufacturer spring constant of the cantilever ($k = 0.12\ N/m$) was used to convert the cantilever deflection sensor signal (in Volt) to the probe-sample force (in nano-Newton, nN). The use of the nominal spring constant serves our purpose of comparing the performance of the above three control methods. The performance with the three control methods are also compared in Table 2.1 in terms of the relative RMS error $E_2(\%)$ and the relative maximum error $E_\infty(\%)$, as defined blow,

$$E_2(\%) \equiv \frac{\|y_d(\cdot) - y(\cdot)\|_2}{\|y_d(\cdot)\|_2} \times 100\%, \quad E_\infty(\%) \equiv \frac{\|y_d(\cdot) - y(\cdot)\|_\infty}{\|y_d(\cdot)\|_\infty} \times 100\%. \tag{2.46}$$

When implementing the EIIC technique, the iteration was stopped when neither the relative RMS-tracking error nor the relative maximum-tracking-error decreased further. The number of iterations used in the experiment are listed in Table 2.1, where the pulling-up rate for the tracking section is also listed.

The experimental results demonstrate the efficacy of the proposed control approach to achieve high-speed precision-tracking of scan trajectory. At the scan rate of 100 Hz, the dynamics-effect on the output tracking was pronounced, resulting in large tracking errors (see the DC-Gain tracking result in Fig. 2.7 (a1) and (b1))—the relative maximum error $E_{max}(\%) = 19.75\%$ (see Table 2.1). However, such large tracking errors were significantly reduced by using the OSDC technique. As shown in Fig. 2.7 (a1) and (b1) and Table 2.1, the relative maximum error $E_{max}(\%)$ was reduced by $\sim$2.5

Table 2.1 Tracking performance comparison by using the OSDC technique, the EIIC technique, and the DC-Gain method, where the RMS-error $E_2(\%)$ and the maximum error $E_{max}(\%)$ are defined in Eq. (2.46). The number of iterations used are also listed.

Scan	P-U	E_2 (%)			E_{max} (%)			Iter.
Rate	Rate ($\mu m/s$)	DC-Gain	OSDC	EIIC	DC-Gain	OSDC	EIIC	No.
100 Hz	90.6	14.06	6.26	.69	19.75	8.80	1.20	6
260 Hz	353.3	25.96	11.27	1.19	24.14	13.01	2.29	6
320 Hz	724.8	50.10	11.48	2.84	46.80	13.15	3.81	6

times. The main frequency components of the tracking error (Fig. 2.7 (b1)), identified through the power spectrum (computated using MATLAB), were around the neighborhood of the resonant peak of the AFM-dynamics at 3.6 KHz — Note that the modeling errors tended to be large around the resonant peak of the AFM-dynamics (see Fig. 2.4 (a)). Such tracking errors caused by the model-uncertainty were removed by using the EIIC technique. As shown in Fig. 2.7 (b1), the tracking error of the EIIC technique was close to the signal noise level. As the scan rate was increased to 320 Hz, the pulling-up rate was increased by 8 times (see Table 2.1), resulting in much larger dynamics-caused tracking errors—the relative maximum error $E_{max}(\%)$ and the relative RMS-error $E_2(\%)$ were increased by over 2.5 times and 3.5 times, respectively (compare Fig. 2.7 (b1) with Fig. 2.7 (b3)). However, the OSDC technique still achieved much better tracking than the DC-Gain method—the maximum error was over 3.5 times smaller, which was even smaller than the error by the DC-Gain method at lower scan rate of 100 Hz. Such tracking errors were further reduced by using the EIIC method. At the high-speed pulling-up rate of 350 Hz, the relative maximum error obtained with the EIIC technique was still small (the relative maximum error $E_{max}(\%) = 3.81\%$). The power spectrum computation of the tracking error revealed that the main frequency components of the tracking error were at 4.6 KHz, which is outside the frequency range of the modeled AFM dynamics at 4.4 KHz. Moreover, such tracking precision achieved with the proposed technique compares very well with our previous results obtained by using the IIC technique (Y. Wu. et al. (2007)), which in turn, were more favorable than the results obtained with a robust control feedback design (M.-S. Tsai. et al. (2003)) and the results obtained with an advanced PID feedback control design (Q. Zou. et al. (2004)) (Readers are referred to (Y. Wu. et al. (2007)) for details). Therefore, the tracking experiments show that the proposed control approach can

achieve high-speed precision-tracking in scanning applications.

Experimental Adhesion Force Measurement The control inputs obtained by using the EIIC technique were used to measure the adhesion force between a silicon-nitride probe and a silicon sample in the ambient environment. We note that under the ambient environment, the measured adhesion force is dominant by the capillary force due to a thin layer of water formed on the sample surface (e.g., (B. L. Weeks. et al. (2005))). The obtained force-time curve (i.e., the probe-sample force vs. time) for the scan rates of 100 Hz, 260 Hz, and 320 Hz are shown in Fig. 2.8 (left column), where the force-time curves obtained with the DC-gain method are also compared. In the right column of Fig. 2.8, the deviations of the pulling-up force away from the constant force-rate during the pulling-up section, measured by curve fitting the force-time curve into a straight line, are compared for the EIIC technique and the DC-Gain method. Note that all the force-time curves were acquired in sequence within two minutes, under the same initial steady-state condition. Therefore, effects such as the environment variations were minimized, and the variation of the force-rate during the pulling-up section, if any, was mainly due to the AFM-dynamics vibration effects.

The experimental results show that the constant pulling-up rate at high-speed can be achieved by using the proposed control technique. As shown in Fig. 2.8 (a1) and (b1), the probe-sample force-rate was maintained as constant (during the pulling-up section) under the control of the EIIC input. The relative maximum variation of the force-rate is only $\sim 1\%$. On the contrary, the force-rate deviation was much larger (over 3 times larger) when using the DC-Gain method. Such force-rate deviation was more pronounced as the pulling-up rate was increased by almost 4 times at the scan rate of 260 Hz (see Fig. 2.8 (a2) and (b2)). However, by using the EIIC algorithm, the constant pulling-up (force-) rate was still maintained. Even as the pulling-rate was increased to 720 μ/m, the constant pulling-out rate was still well maintained. The relative maximum force-rate deviation was still only $\sim 4\%$. Note that the large-amplitude, high-frequency oscillations of the force curve in Fig. 2.8 were the free vibrations of the cantilever in air after the probe-sample bonding was broken. The settling-time of such oscillation was governed by the dynamics of the cantilever. Such constant pulling-out rate achieved in the adhesion force measurement when using the EIIC control input was the result of the precision tracking under the

contact-mode achieved earlier (compare Fig. 2.7 with Fig. 2.8). Therefore, the experimental results demonstrate the efficacy of the proposed control technique in achieving high-speed adhesion-force measurements.

2.4 Conclusions

This chapter studied the account of two practical issues in the design and control of scanning trajectories: the minimization of the output oscillation, and the rejection of the modeling error effect on the output tracking. The proposed approach was based on the extension of the recently-developed optimal scan trajectory design and control (OSDC) technique. First, the design of a prefilter was introduced in the OSDC technique to minimize the output oscillation by using the OSDC technique to the augmented system (of the prefilter cascaded with the system). Then, an enhanced inversion-based iterative control (EIIC) technique was proposed to remove the modeling error effect on the output positioning, further improving the positioning precision. The convergence of the EIIC algorithm was discussed, and the convergence range was quantified. The proposed approach was illustrated by implementing it to high-speed adhesion force measurement using AFM. The simulation and experimental results were presented and discussed to demonstrate the efficacy of the proposed approach to compensate for the two practical issues in scanning trajectory applications.

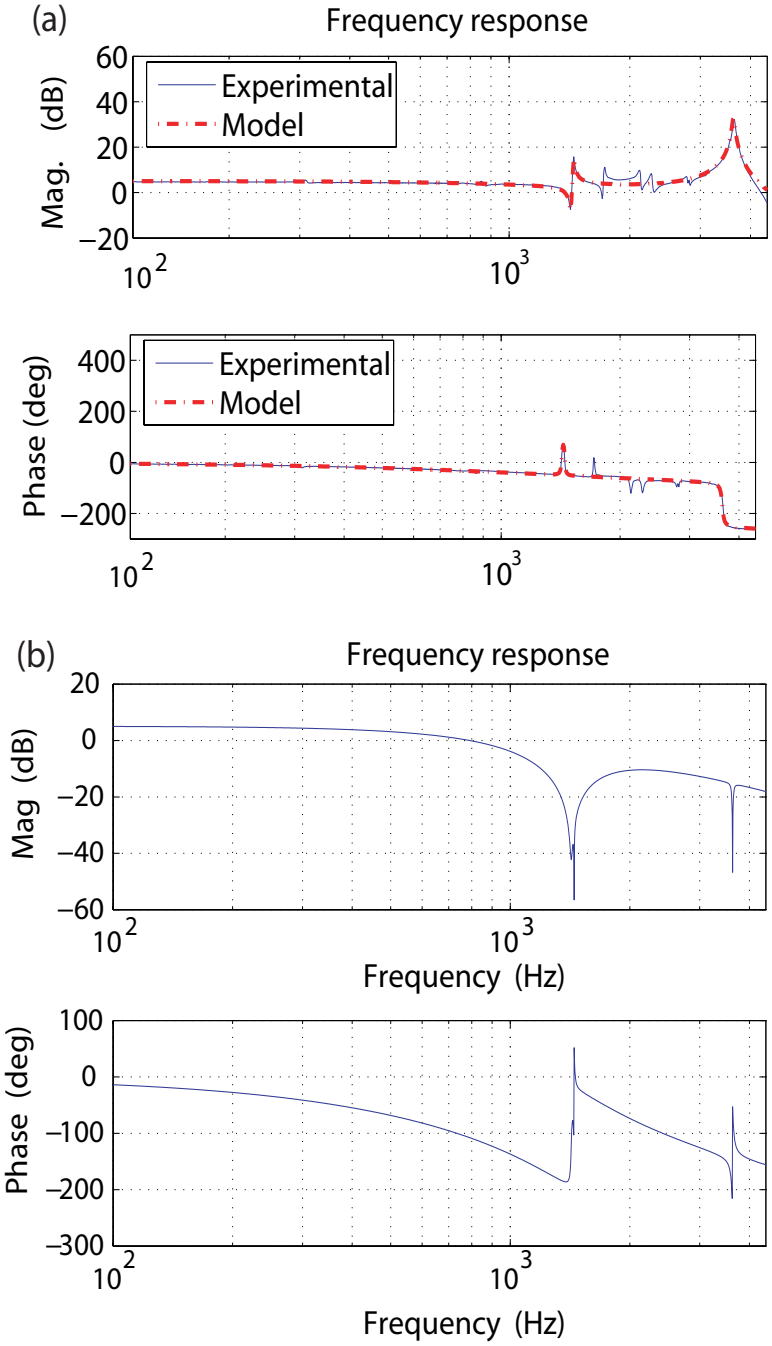

Figure 2.4 (a) Comparison of the experimentally measured frequency response of the z-axis AFM dynamics (from the piezo actuator input to the cantilever deflection output under the contact-mode condition) with the frequency response of the transfer function model obtained via curve–fitting method; and (b) the frequency response of the augmented system model (the prefilter followed by the AFM-dynamics model).

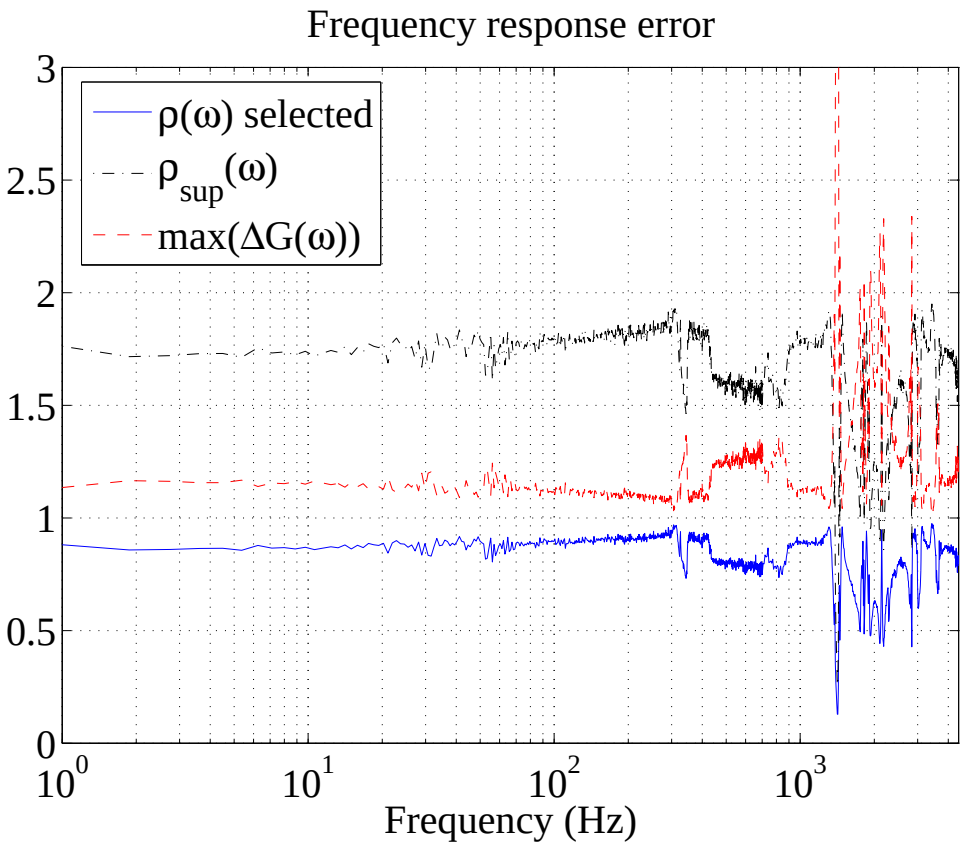

Figure 2.5 The estimated magnitude uncertainty of the AFM-dynamics (red-dotted), the upper bound of the iterative coefficient (green-dash-dotted), $\rho_{sup}(\omega)$ (see Eq. (2.35)), and the iterative coefficient used in the experiments (blue-solid), $\rho(\omega)$.

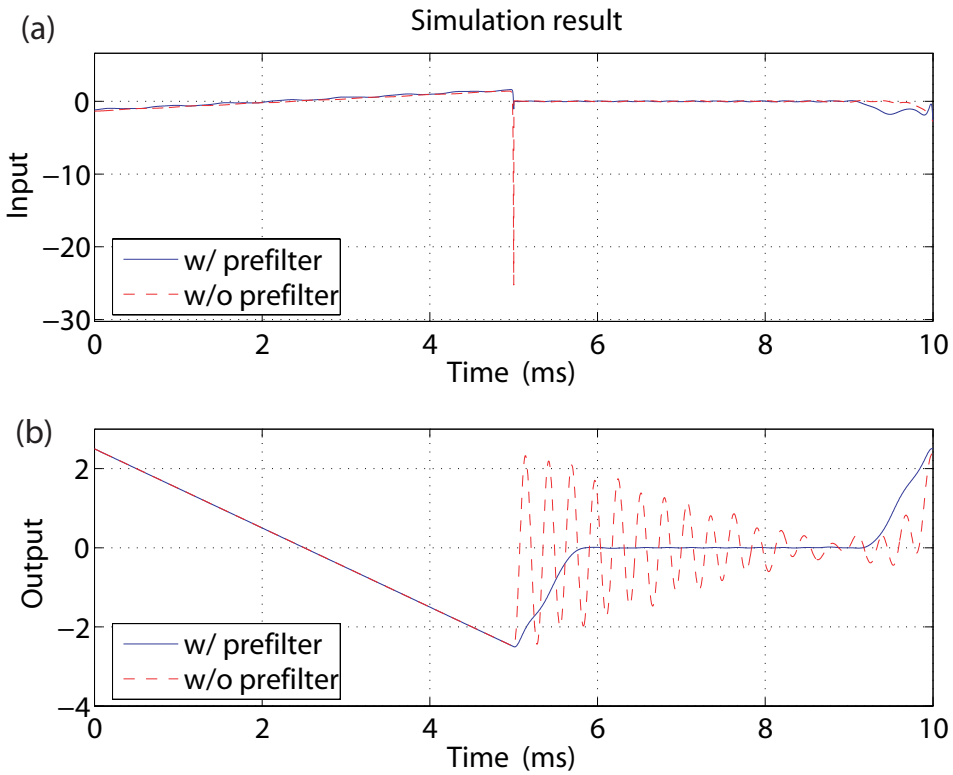

Figure 2.6 Comparison of the optimal inputs (plot (a)) and the corresponding optimal output trajectories (plot (b)) obtained by using the OSDC technique for the augmented system with (solid) and without (dashed) the prefilter. The signal frequency is 100 Hz with the duty ratio $R_d = 50\%$.

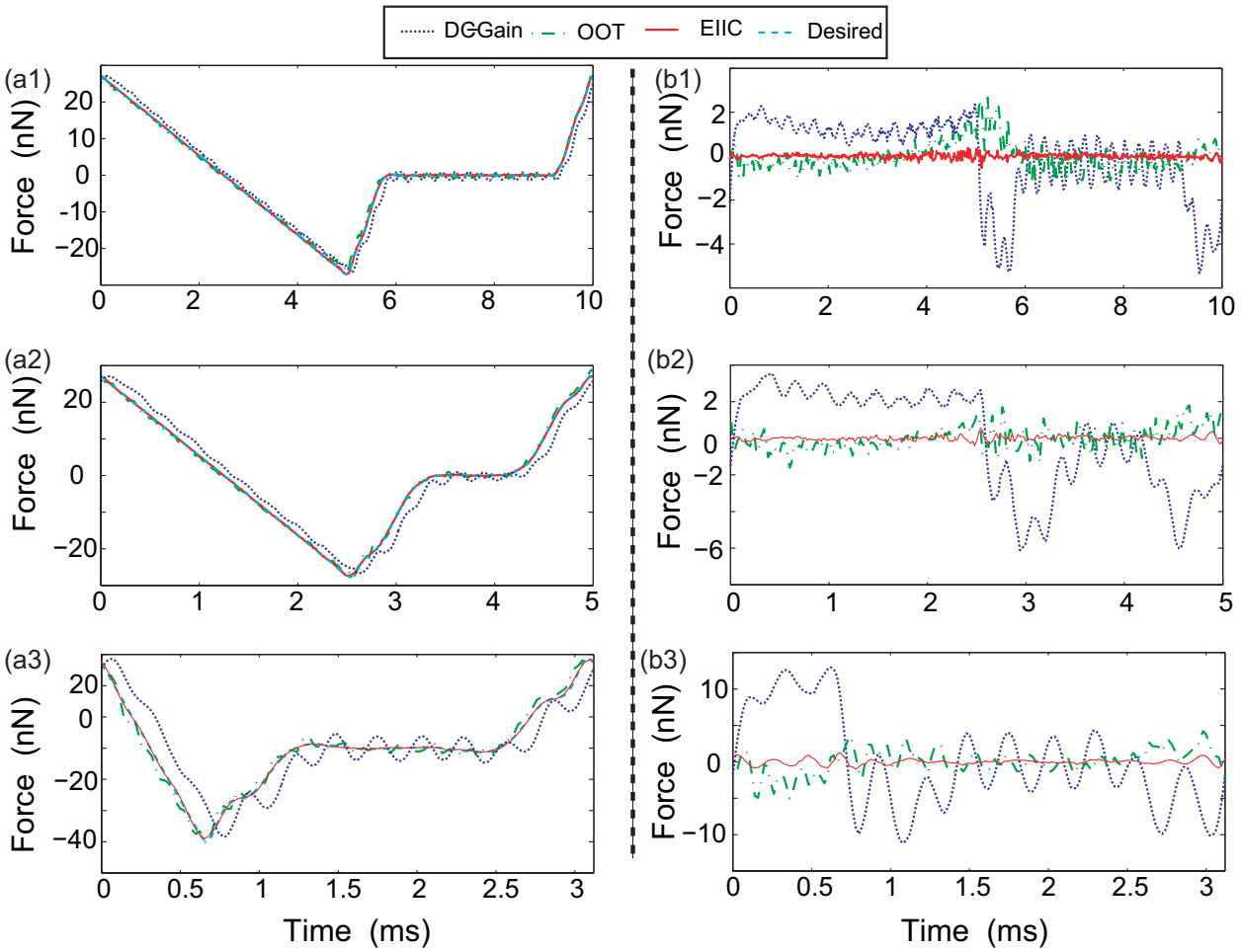

Figure 2.7 Comparison of the experimental tracking results obtained by using the DC-Gain method, the OSDC technique, and the EIIC technique for the scan rate of (a1) 100 Hz, (a2) 260 Hz, and (a3) 320 Hz; and the comparison of the corresponding tracking errors (right column).

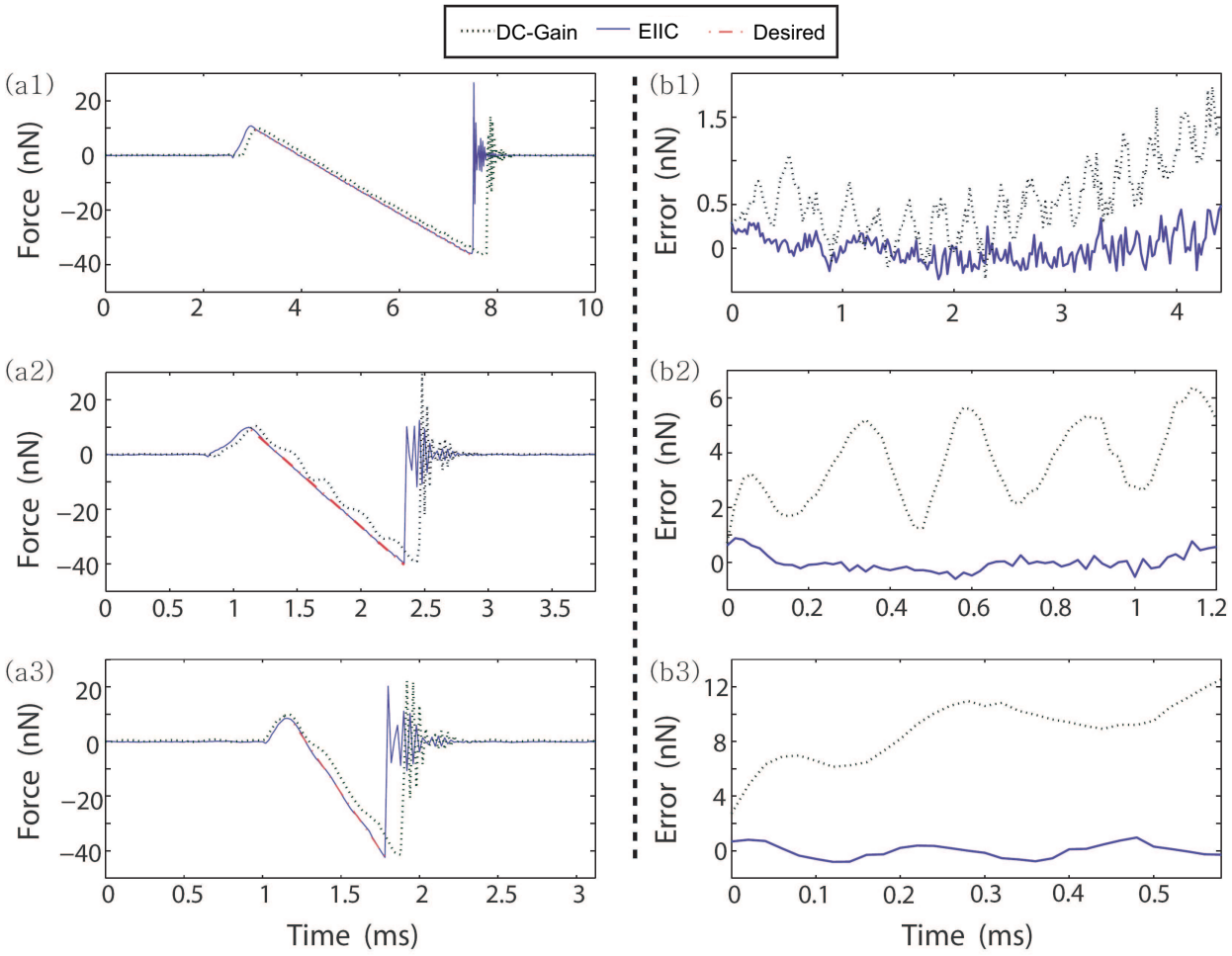

Figure 2.8 Left column: The comparison of the experimentally measured probe-sample force trajectory (i.e., force-time curve) for adhesion–force measurements, obtained by using the DC-Gain method with the curves by using the EIIC technique at the scan rates of (a1) 100 Hz, (b1) 260 Hz, and (c1) 320 Hz. Right column: The comparison of the corresponding deviations of the force-curve from the constant force-rate during the pulling-up section for the scan rates of (a2) 100 Hz, (b2) 260 Hz, and (c2) 320 Hz.

CHAPTER 3. Iterative Control Approach to High-Speed Force-Distance Curve Measurement Using AFM: Time Dependent Response of PDMS

A paper published in Ultramicroscopy

Abstract

Force-distance curve measurements using atomic force microscopy has been widely used in a broad range of areas. However, current force-curve measurement are hampered by its low speed. In this chapter, a novel inversion-based iterative control technique is proposed to dramatically increase the speed of force-curve measurements. Experimental results are presented to show that by using the proposed control technique, the speed of force-curve measurements can be increased by over 80 times—with no loss of spatial resolution—on a commercial AFM platform and with a standard cantilever. This control technique is further applied to quantitatively study the time-dependent elastic modulus of poly(dimethylsiloxane) (PDMS), by measuring the force-curves with a broad spectrum of push-in (load) rates, spanning two-order differences. The elastic modulus measured at low-speed compares well with the value obtained from dynamic mechanical analysis (DMA) test, and the value of the elastic modulus increases as the push-in rate increases, signifying that a faster external deformation rate transitions the viscoelastic response of PDMS from that of a rubbery material toward a glassy one.

3.1 Introduction

In this chapter, we illustrate the implementation of a novel inversion-based iterative control technique to achieve high-speed force-curve measurement on a commercial atomic force microscope (AFM), through the measurement of time-dependent properties (e.g., elastic modulus) of poly(dimethylsiloxane)

(PDMS) as an example. Force-curve measurements using AFM (A. L. Weisenhorn. et al. (1989, 1992); N. A. Burnham. et al. (1989)) has opened the door to experimentally study materials properties (H.-J. Butt. et al. (2005)) as well as physical and/or chemical interactions between materials (P. P. Lehenkari. et al. (2000)). However, such interrogations are currently hindered by the low-speed operation of AFM. This is because numerous force-curve measurements usually need to be obtained, particularly in the so-call force-volume imaging (O. H. Willemsen. et al. (2004)-E. A-Hassan. et al. (1989)), where a distributive mapping of force-curves over the sample is obtained. Since multiple force-curves need to be acquired at each sample point while the sample is scanned with a rastern pattern, currently force-volume imaging is time-consuming (S. A. Syed Asif. et al. (2001)). More fundamentally, the low-speed of force-curve measurements encumbers the study of time-dependent material properties/interactions at micro-/nano- scale (J. Zlatanovaa. et al. (2000); F. Schwesinger. et al. (2000)). For example, the force-curve measurement using AFM enabled the studies of the dependence of the unfolding force of a titin domain (E. Evans. et al. (1999)), or the unbinding force of a single DNA strand (T. Strunz. et al. (1999)), on the retraction/pulling rate. However, currently the achievable spectrum of the force (load)-rates in these studies is limited to the low-speed range (~ 10 μm/sec in (E. Evans. et al. (1999)) and ~ 2 μm/sec in (T. Strunz. et al. (1999))). Another example is the study of stress-induced chemical bond breaking of siloxane elastomers in the high force regime. To verify the theoretical prediction results (E.M. Lupton. et al. (2005)) obtained from molecular dynamics simulation, the force-curves of single molecule need to be measured at a daunting retraction (unload) rate of nearly m/s range, which is far beyond the achievable rate on current AFM. Clearly, there exist needs for high-speed AFM force-curve measurement.

The speed of force-curve measurement can be increased by using the force-modulation technique (S. A. Syed Asif. et al. (2001, 1999); W. C. Oliver. et al. (1992)), where a sinusoidal force signal (i.e., ac signal) of small amplitude is augmented with the displacement driven signal, and applied to the tip during the force-curve measurement. Then the amplitude change and phase shift of the tip oscillations, relative to the input driven force, are acquired and used to measure the elastic stiffness of the material (S. A. Syed Asif. et al. (1999); W. C. Oliver. et al. (1992)). Although the modulation frequency can be

changed from a few Hz to 200 Hz (S. A. Syed Asif. et al. (1999, 2001)), the equivalent push-in (load) and retraction (unload) rate is still low ($< 6\mu$m/sec), due to the small oscillation amplitude (< 30 nm). The push-in/retraction rate is further limited because only sinusoidal signal can be applied—methods to increase the rate by using other shape of trajectories (F. Schwesinger. et al. (2000)) cannot be implemented. Moreover, the force-modulation technique requires extra hardware and a complicated parameter calibration process (S. A. Syed Asif. et al. (1999, 2001)), and its efficiency is inherently limited because a de-modulation process is needed to accurately measure the amplitude and phase shift, which is time consuming. Therefore, techniques need to be developed to achieve high-speed force-curve measurement.

Recently, advanced control techniques (see, e.g., the tutorial paper (D. Abramovitch. et al. (2007)) and the references therein) have been proposed to improve the throughput of AFM imaging, or more generally, the nanopositioning of piezoelectric actuators (A. J. Fleming. et al. (2006)). For example, the system-inversion-based techniques (Q. Zou. et al. (2004))-(H. Perez. et al. (2004)) have been developed to find the output-tracking feedforward control input by feeding the desired output trajectory through the inverse of the system dynamics model and/or hysteresis model. The feedback control design (G. Schitter. et al. (2004)) based on robust control theory has also been proposed. Recently, efforts to combine these two approaches, the feedforward with the feedback control, have also been pursued for AFM applications (G. Schitter. et al. (2003); Ying Wu. et al. (2007)). The efficacy of these control developments in improving the lateral scanning (Ying Wu. et al. (2006); S. Salapaka. et al. (2002)-H. Perez. et al. (2004)) as well as the vertical AFM-tip positioning (G. Schitter. et al. (2003)) for AFM imaging have been successfully demonstrated. To the best of our knowledge, however, no advanced control techniques have been developed for high-speed force-curve measurement.

We present a novel enhanced inversion-based iterative control (EIIC) technique for high-speed force-curve measurements. This EIIC technique seeks an appropriate feedforward control input through iterations to eliminate, during high-speed force-curve measurements, the adverse effects of the AFM system. The adverse effects include the vibrational dynamics, the hysteresis, and the creep effects (S.

A. Syed Asif. et al. (1999); D. Croft. et al. (2001)) of the AFM system (from the piezo-tube actuator to the cantilever along with the mechanical linkage in between). For force-curve measurements, the desired output (i.e., the applied force profile) is pre-defined, and the push-in/retraction operation is *repetitive*, making it possible to account for the above adverse effects on the output tracking through iterative update of the control input with the measured output errors. Therefore, the iterative control strategy is intuitively appealing for force-curve measurements. It has been demonstrated that the IIC-type of control algorithms can adequately "cancel" the dynamics-induced vibrations (S. Tien. et al. (2005)) and the hysteresis-caused nonlinear measurement errors (Ying Wu. et al. (2006)) during high-speed repetitive motion. However, in the IIC algorithm, the iteration of the input magnitude is coupled in the frequency-domain with the iteration of the input phase. Such coupling is removed in the proposed EIIC technique. Therefore, the EIIC algorithm extends the IIC algorithm, and can achieve the convergence in a larger frequency range with a faster convergence rate . We illustrate the use of the proposed EIIC technique in material characterization by applying it to quantitatively study the time-dependent elastic modulus of poly(dimethylsiloxane) (PDMS). The measured values of the elastic modulus are compared with the results obtained from the dynamic mechanical analysis (DMA) test of the PDMS.

3.2 Methods

3.2.1 Force curve measurement using AFM

AFM Force-Curve Measurement Various materials properties can be interrogated at submicro to nano-scale by using AFM through the force-curve measurement (M. Vanlandingham. et al. (1997)). To do so, the AFM-tip is driven by a piezoelectric actuator to push against the sample till the bending of the tip (i.e., the force applied onto the sample surface) reaches a pre-determined value, then the AFM-tip will retrace to a pre-determined distance—the tip can be either in continuous or intermittent contact with the sample surface during the process (H.-J. Butt. et al. (2005)) (see Fig. 3.1(a)). The force-distance curve, as schematically depicted in Fig. 3.1 (b), is obtained by measuring the tip-sample interaction force along with the vertical displacement of the AFM-tip during the push-in/retraction pro-

cess. The tip-sample force is measured from the tip deflection via an optics sensing scheme (Veeco Manual. et al. (2004), and the AFM-tip displacement is measured from the vertical displacement of the piezoelectric actuator if the indentation of the tip into the sample is negligible, i.e., when the sample is hard enough. Indentation, however, occurs and must be accounted-for when the sample is soft (H.-J. Butt. et al. (2005); S. A. Chizhik. et al. (2001); A. Weisenhorn. et al. (1993)), for example, the PDMS. The indentation is obtained as the difference between the AFM-tip displacement on a reference hard sample and on the soft sample (M. Vanlandingham. et al. (1997)). Then, the measured tip-sample interaction force vs. the indentation can be used to study various material mechanical properties (H.-J. Butt. et al. (2005)), for example, the elastic modulus.

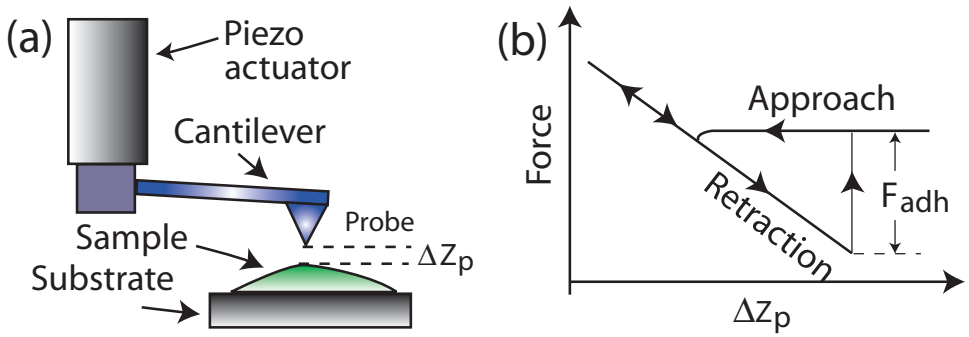

Figure 3.1 The scheme of AFM force curve measurement

3.2.2 Enhanced inversion-based Iterative-Control (EIIC) Approach to High-Speed Force-Curve Measurement

EIIC technique The EIIC control law can be described in frequency-domain as follows: At the first iteration, k=0, choose the initial input (e.g., the voltage applied to the piezo-tube actuator), as the scaled desired output trajectory $z_d(j\omega)$, where the scale factor is chosen as the inverse of the system dynamics model, $G_m^{-1}(j\omega)$,

$$u_0(j\omega) = G_m^{-1}(j\omega) z_d(j\omega), \qquad k = 0, \tag{3.1}$$

where '$f(j\omega)$' is the Fourier transform of a time-signal '$f(t)$', and the frequency response model of the system dynamics, $G_m(j\omega)$, can be measured experimentally (J.-N. Juang. et al. (2001)). Then for

all other iterations, $k \geq 1$, compute the control input by updating it with the positioning errors from the previous iteration, $z_d(j\omega) - z_{k-1}(j\omega)$,

$$\begin{aligned} |u_k(j\omega)| &= |u_{k-1}(j\omega)| + \rho(\omega)\left|G_m^{-1}(j\omega)\right|\left[|z_d(j\omega)| - |z_{k-1}(j\omega)|\right], \\ \angle u_k(j\omega) &= \angle u_{k-1}(j\omega) + (\angle z_d(j\omega) - \angle z_{k-1}(j\omega)), \qquad\qquad k \geq 1, \end{aligned} \tag{3.2}$$

where $z_k(j\omega)$ denotes the output obtained by applying the iterative input $u_k(j\omega)$ to the system during the k^{th} iteration, $\rho(\omega) > 0$ is the iteration coefficient. It has been shown that the choice of the iteration coefficient to guarantee the convergence of the iteration depends on the size of the uncertainty of the system dynamics. More specifically, let the dynamics uncertainty $\Delta G(j\omega)$ be the ratio of the actual AFM dynamics $G(j\omega)$ over the measured dynamics model $G_m(j\omega)$,

$$\Delta G(j\omega) = \frac{G(j\omega)}{G_m(j\omega)} = \frac{|G(j\omega)|e^{j\angle G(\omega)}}{|G_m(\omega)|e^{j\angle G(\omega)}} \triangleq |\Delta G(\omega)|\, e^{j\Delta\angle G(j\omega)}, \tag{3.3}$$

then it can be shown that if the iterative coefficient $\rho(\omega)$ is chosen within the following range,

$$0 < \rho(\omega) < \frac{2}{|\Delta G(j\omega)|}, \tag{3.4}$$

the above EIIC algorithm (3.2) will converge to the desired input $u_d(j\omega)$ at frequency ω, i.e.,

$$\lim_{k\to\infty} |u_k(j\omega)| = |u_d(j\omega)|, \text{ and } \lim_{k\to\infty} \angle u_k(j\omega) = \angle u_d(j\omega).$$

where $u_d(j\omega)$ denotes the desired input for achieving exact tracking of the desired trajectory at the frequency ω. Therefore, the converged control input will remove the system dynamics effect on the output (e.g., the AFM-tip deflection).

Note that in the above convergence analysis, the effect of noise is ignored. However, it can be shown that the noise effect is small provided that the noise level is low. Specifically, let the the sensor noise $z_n(t)$ is added to the system output $z(t)$, and the measured system output becomes,

$$\tilde{z}(t) = z_n(t) + z(t).$$

Then it can be shown that the error between the converged iterative control input and the desired input is bounded above by a constant proportional to the noise level as follows,

$$\lim_{k\to\infty}\big||u_k(j\omega)|-|u_d(j\omega)|\big| \leq |G_m^{-1}(j\omega)||z_n(j\omega)| \tag{3.5}$$

$$|\angle u_k(j\omega)-\angle u_d(j\omega)| \leq \tan^{-1}\frac{|z_n(j\omega)|}{|z_k(j\omega)|}, \quad \text{for } \forall k\geq 1. \tag{3.6}$$

Implementation of the EIIC Algorithm Equation (3.4) implies that to determine the iteration coefficient $\rho(\omega)$ in the EIIC algorithm (3.2), the dynamics uncertainty $\Delta G(j\omega)$ must be quantified. Although in many applications, the exact dynamics uncertainty may not be quantified due to the actual dynamics $G(\omega)$ being unknown, an estimation of the dynamics uncertainty can be obtained through experiments so that the exact dynamics uncertainty $\Delta G(j\omega)$ is bounded above by the estimated dynamics uncertainty $\hat{\Delta}G(j\omega)$, $|\Delta G(j\omega)|\leq|\hat{\Delta}G(j\omega)|$. Therefore, the iterative coefficient $\rho(\omega)$, computed by using the estimated dynamics uncertainty in Eq. (3.4), will guarantee the convergence of the EIIC algorithm. The dynamics uncertainty can be estimated through experiments by measuring a series of the frequency responses of the system (for example, with different input amplitudes), and then finding the maximum difference among the measured frequency responses at each frequency .

We further note that as the iterative control methodology is intended for *repetitive* applications where the desired trajectory $z_d(t)$ is usually known *a priori*, the comparison between the desired output trajectory and the measured output, and thereby the computation of the EIIC algorithm can be conducted *offline*, instead of online. Then the obtained iterative control input is applied as a *feedforward* control input to the system. This implies that the proposed EIIC algorithm can be implemented in frequency-domain directly using the fast Fourier transform (FFT) algorithm (and inverse Fourier transform), i.e., the time-domain iterative control input is obtained as

$$u_k(t)=\mathscr{F}^{-1}[u_k(j\omega)] \tag{3.7}$$

where $\mathscr{F}^{-1}$ denotes the inverse Fourier transform. Such a frequency-domain realization also implies that the experimentally measured frequency response data can be used directly in the EIIC algorithm. Therefore, the explicit transfer function model obtained via, for example, curve-fitting method, is not needed. Not only is the implementation simplified, but the modeling errors generated during the curve-fitting to obtain the transfer function model is removed—as usually a lower-order transfer function

model is preferred over high-order ones for computation efficiency in time-domain realization.

Finally, the EIIC algorithm (3.2) is applied at those frequency components of the desired output trajectory $z_d(j\omega)$ where the gain of the system dynamics is large enough—relative to the noise level of the system, and the control input is set to zero at all other frequencies (readers are referred to Ref. for details). The iteration process should be stopped if the tracking error, $z_d(t) - z_k(t)$, measured by using some chosen signal norm (e.g., 2-norm and/or infinity norm), can not be further reduced. These implementation issues are illustrated in Sec. 3.3.1.

Desired trajectory design To use the above EIIC algorithm to interrogate the time-dependent elastic modulus of PDMS, the desired trajectory ($z_d(j\omega)$ in Eq. (3.2)), e.g., the desired AFM-tip vertical displacement vs. time during the push-in/retraction process, needs to be pre-specified. The desired trajectory used in the experiments is schematically depicted in Fig. 3.2, where the push-in and the retraction sections are separated by two flat sections. Since the push-in section of the force-curve is chosen to measure and calculate the time-dependent elastic modules of the PDMS sample, the desired trajectory is designed by varying the time period of the push-in section, $[t_0,\ t_1]$ in Fig. 3.2 while maintaining the same push-in distance. The retraction time period, $[t_2,\ t_3]$, is chosen to be twice longer than the push-in period $[t_0,\ t_1]$ in the experiments to reduce the zero load plastic deformation. The constant flat period of a fixed duration at 5 ms, is added to help the tracking during the push-in section (at high speed), which can also be used to investigate material relaxation at different push-in rates.

It is noted that other shapes of user-defined trajectories can be used in the EIIC algorithm, provided that the trajectory is continuous with its main frequency components within the bandwidth of the piezo actuator. For example, to measure the time-dependent viscoelasticity of materials, the desired cantilever displacement trajectory can be designed by reversing the design of the above asymmetric trajectory to have a fixed push-in rate but different retraction rates. Therefore, the proposed EIIC algorithm allows the use of trajectory design (F. Schwesinger. et al. (2000)) in high-speed force-curve measurements.

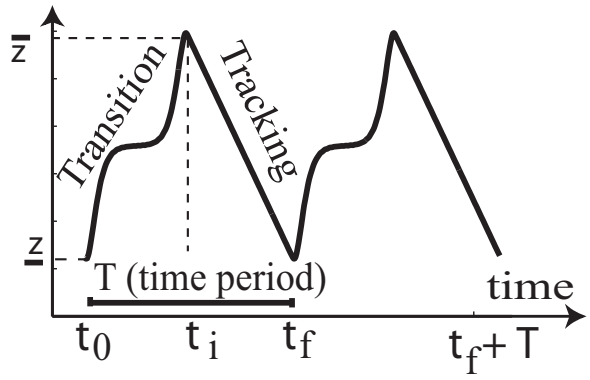

Figure 3.2 The tracking trajectory consisting of a push-in section (an indentation process) during the time interval $[t_0,\ t_1]$ and a retraction section (a recovery process) during the time interval $[t_2,\ t_3]$, with a flat period in between, where the different push-in rate is obtained by varying the push-in period $[t_0, t_1]$ while keeping the same push-in distance $d_1 - d_0$.

Use of EIIC Algorithm in Force-Curve Measurement The EIIC algorithm was used to measure the force-curve of the PDMS sample at different push-in rates. First, to obtain the control input that compensates for the dynamics effects of the AFM system (from the piezo-tube actuator to the cantilever along with the mechanical linkage in between) during high-speed force-curve operations, the EIIC algorithm was applied to measure the force-curve on a hard sample (a silicon calibration sample). Therefore, when such a control input is applied to measure the force-curve on the PDMS sample, the obtained force-curve should not contain distortions from the AFM system dynamics effect. As a result, the difference between the force-curve obtained on the hard sample and that obtained on PDMS should yield the mechanical property (e.g., elastic modulus) of PDMS. Moreover, our experimental results (see Sec. 3.3) show that by using such a control input, constant push-in (load) rate can be obtained on the PDMS sample.

Force and Indentation Computation The force applied to the sample F_S is computed according to $F_S = k \times C \times \theta_S$, where k is the stiffness constant of the tip, C is the sensitivity constant of the deflection signal vs. the vertical displacement of the tip, and θ_S denote the deflection signal measured on the sample. Then the indentation depth z_I is computed by

$$z_I = C \times (\theta_H - \theta_S) \tag{3.8}$$

where θ_H denotes the deflection signal measured on the hard surface. Note both the stiffness constant k and the sensitivity constant C can be experimentally calibrated (J. L. Hutter. et al. (1993)).

3.2.3 Theory: Hertzian contact model

Hertzian model (H.-J. Butt. et al. (2005); M. Vanlandingham. et al. (1997)) was employed to estimate the elastic modulus of the sample PDMS by using the experimentally measured force-curve data. The time-dependence of the elastic modulus is examined by using the force-curves obtained at different push-in rates in the calculation. According to the Hertzian model (H.-J. Butt. et al. (2005); Heinrich. Hertz. et al. (1896)), for two elastic materials (the sample and the tip) brought into contact, the contact area at zero load is zero ($a_0 = 0$) and the surface forces or adhesion force is negligible during the contact ($F_{adh} = 0$). Then the stiffness modulus of the sample (E_s) can be calculated by using the indentation depth δ, and the reduced Elastic modulus E_{tot} of the sample:

$$\delta = \left(\frac{F^2}{R \times E_{tot}^2}\right)^{1/3}, \tag{3.9}$$

$$\frac{1}{E_{tot}} = \frac{3}{4}\left(\frac{1-\nu_s^2}{E_s} + \frac{1-\nu_t^2}{E_t}\right), \tag{3.10}$$

where F, R, and E_t are the applied force, the tip radius, and the tip elastic modulus, respectively, and ν_s and ν_t are the Poisson's ratio of the sample and the tip, respectively. For soft samples like PDMS, its elastic modulus E_s (in several MPa range) is over 7 order smaller than that of the probe (silicon nitride) E_t at 160-290 GPa (H.-J. Butt. et al. (2005)), therefore the above Eq. (3.10) can be simplified as

$$\frac{1}{E_{tot}} \approx \frac{3}{4}\left(\frac{1-\nu_s^2}{E_s}\right) \tag{3.11}$$

3.3 Experimental Results and Discussion

3.3.1 Experimental Instrumentation

A commercial AFM system (Dimension 3100, Veeco Inc.) was used in all experiments along with a standard V-shaped Silicon Nitride cantilever as provided by the manufacturer. The nominal spring constant and the nominal curvature radius of the cantilever were 0.12 N/m and 20 nm, respectively. The effective spring constant of the cantilever, 0.07 N/m, was measured by using the thermal noise method

(J. L. Hutter. et al. (1993)) at room temperature. To minimize the effect of the tip shape variation during the experiment, the tip had been used to image a silicon calibration sample for over 5000 scan lines at the scan size of over 50 μm before the tip was used to measure the force-curve in the following experiments, thus containing a "steady-state" radius. Kanaga Karuppiah and co-workers found negligible wear on the probe as a result of sliding friction and force curve experiments on ultra-high molecular weight polyethylene (J. L. Hutter. et al. (2006)). Indentation on a soft material like PDMS is therefore not expected to result in wear of probe tip during the force displacement experiments. Hence a constant tip radius is used for calculation of modulus in Hertzian analysis. In our previous work (A. Mitchell. et al. (2006); J. L. Hutter. et al. (2006)), we consistently obtained a tip radius between 42-50 nm after imaging a hard sample for similar number of scan lines. The tip radius was measured through inverse imaging the probe over a calibration grating that has silicon spikes with radii of curvature less than 10nm. Hence, in the following, a tip radius of 50 nm was assumed for modulus computation during Hertzian analysis.

The experimental system to implement the EIIC control law to achieve high-speed force-curve measurement is depicted in Fig. 3.3. All the control inputs to the piezoelectric actuator were generated by using MATLAB xPC-target (Mathworks Inc.), and sent out through a data acquisition card (DAQ, PCI-DAS1602/16, Measurement Computing Inc.) to the high-voltage amplifier of the AFM-controller—The AFM-controller was modified so that the PID (proportional-integral-derivative) control circuit is bypassed when the external control input is applied. The corresponding cantilever deflection signal was sampled at 50 KHz by using the DAQ system. The environment humidity was controlled under 20% by feeding Nitrogen gas into a home-made sealed plastic box that covered the AFM head for over 40 minutes before the experiments were conducted (We note that PDMS is a hydrophobic material, and residual humidity is not expected to significantly influence the experimental measurements). All the experiments, including the iterations of the control inputs using the EIIC law on the hard surface, and the application of the obtained control inputs to measure the force-curves on the PDMS sample, were conducted with the box sealed (A flash light and a webcam were placed inside the box to aid the operation). The force-curve at different push-in rates were measured in sequence with a separation time of

$\sim$15s in between. The iteration was stopped when neither the relative RMS-tracking error $E_2(\%)$ nor the relative maximum-tracking error $E_\infty(\%)$ decreased further, where $E_2(\%)$ and $E_\infty(\%)$ are defined as

$$E_2(\%) \triangleq \frac{\|z_d(\cdot) - z(\cdot)\|_2}{\|z_d(\cdot)\|_2} \times 100\%, \quad E_\infty(\%) \triangleq \frac{\|z_d(\cdot) - z(\cdot)\|_\infty}{\|z_d(\cdot)\|_\infty} \times 100\%. \tag{3.12}$$

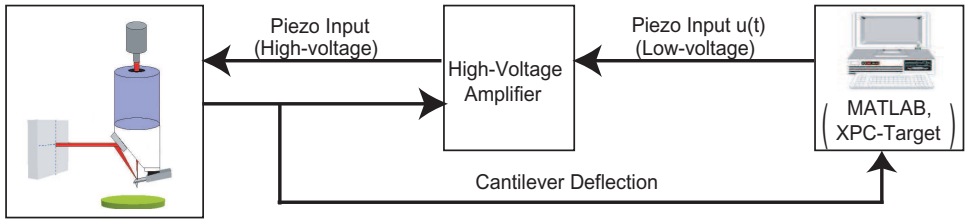

Figure 3.3 The block diagram showing the experiment setup to implement the EIIC algorithm to measure the time-dependent elastic modulus of PDMS using AFM.

Experimental Implementation of the EIIC algorithm The frequency response of the AFM dynamics was measured by, first, positioning the AFM probe on the hard (silicon) sample with a small deflection force (tuned by using the AFM controller software), then driving the piezoelectric actuator with a sinusoidal input with frequency sweeping from 1 Hz to 6 KHz (i.e., the *sweep sine method*), and measuring the cantilever deflection signal. The frequency responses acquired with three different input levels (20, 40, and 50 mV) at three different locations of the sample, respectively, were shown in Fig. 3.4. The maximum magnitude variations among the three frequency responses $|\Delta G(j\omega)|$ and the upper bounded of the iteration coefficient $\rho_{\sup}(j\omega)$ computed by (3.4) are shown in Fig. 3.5, from which the iterative coefficient $\rho(j\omega)$ used in the experiments were determined, as shown in Fig. 3.5. Finally, the nominal frequency response used in the EIIC algorithm was obtained as the average of the four measured frequency responses (see Fig. 3.4). Note Fig. 3.4, in the high frequency range (around 4$\sim$6 KHz), the gain of AFM system drops dramatically and large dynamics uncertainty occurs, therefore the EIIC algorithm was implemented for frequency $\omega \leq$6 KHz, i.e., the iterative control input $u_k(j\omega)$ was set to zero for all frequency $\omega >$ 6 KHz.

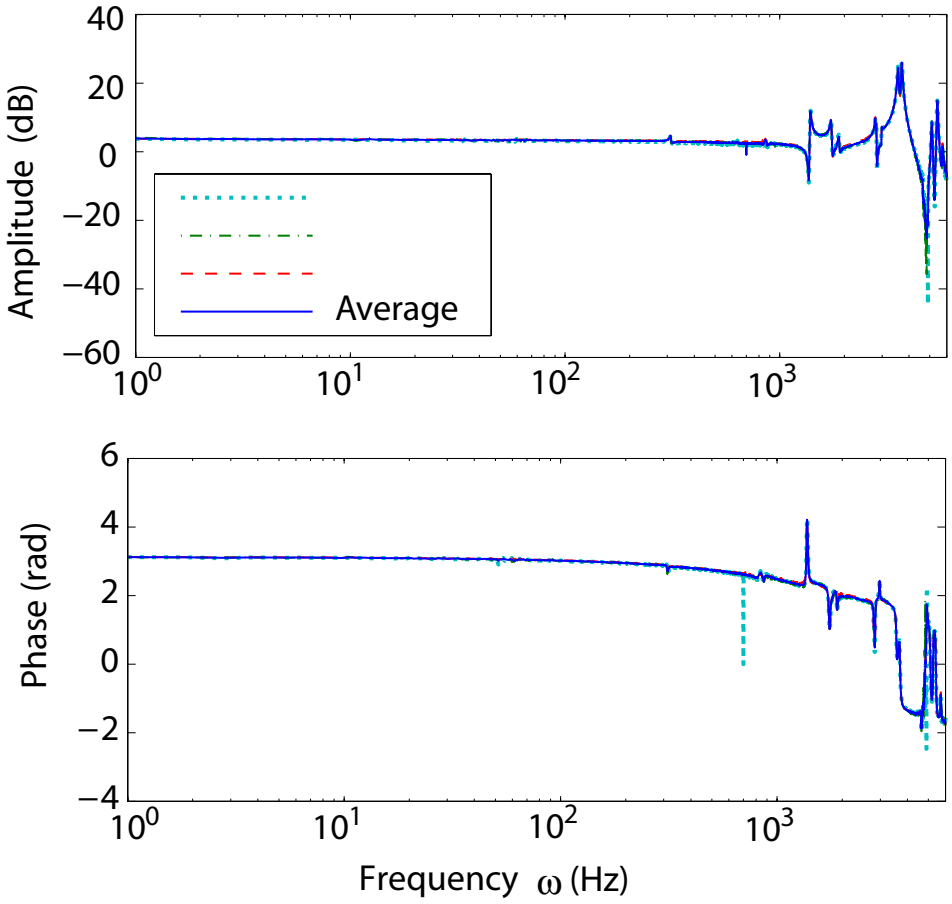

Figure 3.4 The frequency responses of the AFM dynamics measured in experiments with three different input levels (20, 40, and 50 mV), and the nominal frequency response (the average of the above four) used in the EIIC algorithm.

3.3.2 Tracking Results on the Silicon Sample

The force-curves at 12 different push-in rates, spanning 400 times difference from 2.16 μm/s to 864 μm/s, were measured on the Silicon sample—every push-in rate is a multiple integer times of the base speed at 1.08 μm/s (or equivalently, 12 mV/ms—with the system sensitivity at 90 nm/V). The displacement range was fixed at 270 nm—thus the slowest push-in rate of 2.16 μm/s corresponds to a scan rate of 2.53 Hz (the scan rate is defined as the rate of one push-in/retraction operation). The RMS positioning error $E_2(\%)$ and the relative maximum error $E_\infty(\%)$ for the 12 different push-in rates are listed in Table. 3.1, where the iteration numbers to achieve the convergence are also listed for each

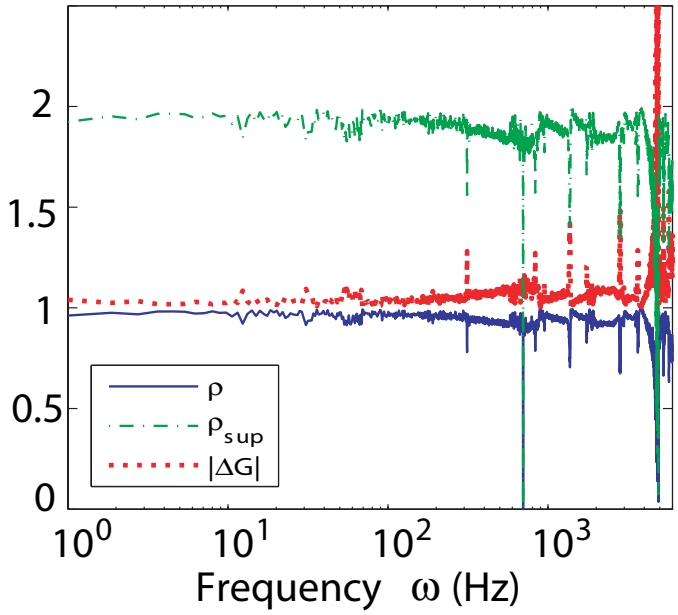

Figure 3.5 The experimentally estimated magnitude variation of the AFM dynamics $|\Delta G(j\omega)|$, the computed upper bound of the iterative coefficient, ρ_{sup}, and the iterative coefficient used in the experiments, ρ.

push-in rate. In addition, the tip vertical displacements vs. time at the push-in rate of 2.16 μm/s and 648 μm/s are plotted in Fig. 3.6. As can be seen from Table. 3.1 and Fig. 3.6, precision positioning is maintained for all push-in rates—The positioning errors, measured by the RMS error $E_2 \leq 1.5\%$ and the maximum tracking error $E_\infty(\%) \leq 2.5\%$, are close to the noise-level of the system. Particularly, we note that even at the high rate of 864 μ m/s, the positioning error is still close to the error at the low rate of 2.16 μm/s. Therefore, our experiment results show that high-speed force curve measurement with no loss of spatial resolution can be obtained by using the proposed EIIC technique.

To ensure that force-curves of PDMS were measured within the elastic deformation range of PDMS, a relatively small cantilever displacement (indentation) range ($\sim$270 nm) was chosen in the experiments (see Fig. 3.6). As shown later in Fig. 3.11, such a displacement range resulted in a force load size at $\sim$14 nN, which is well-below the elastic deformation range of PDMS as quantified in (K. Wahl. et al. (2006)). However, not shown here, even if we doubled to quadrupled the displacement range but kept the same time duration of the push-in portion, the tracking precision similar to Table 3.1 can still be

Table 3.1 Tracking performance results obtained by using the EIIC technique to measure the force-curves on a silicon sample at different push-in rates, where the RMS-error $E_2(\%)$ and the maximum error $E_{max}(\%)$ are defined in Eq. (3.12), and the iteration numbers (Iter. No.) to achieve the convergence at each push-in rate are also listed.

Push-in Rate ($\mu m/s$)	2.16	5.4	10.8	21.6	43.2	64.8
$E_2(\%)$	0.96	0.97	0.82	0.91	1.37	0.73
$E_\infty(\%)$	2.07	2.41	1.5	1.74	2.39	2.11
Iter. No.	5	3	5	3	3	3
Push-in Rate ($\mu m/s$)	86.4	108	216	432	648	864
$E_2(\%)$	0.86	0.88	0.72	0.85	0.70	0.99
$E_\infty(\%)$	1.68	2.08	2.16	1.86	1.86	2.2206
Iter. No.	2	2	1	6	4	3

maintained. This implies that even much higher push-in rate (doubled to quadrupled) can be achieved with the proposed EIIC technique (864 μm/s $\times 4 = 3.456$ mm/s).

3.3.3 Materials: PDMS

The PDMS sample with an appropriate thickness for DMA measurement was prepared as follows. The prepolymer (Sylgard 184 Silicon Elastomer base, Dow Corning) and curing agent were vigorously mixed at 1:10 ratio by weight. The prepolymer/curing agent mixture was then degassed in vacuum oven for 1 hr to remove any trapped air inside the mixture. Subsequently, the mixture was deposited in a plastic *Petri* dish, and cured at room temperature for 2 days in vacuum oven. Finally, the resulting PDMS film was truncated into a desirable dimension for DMA and AFM measurements.

3.3.4 Force-Curve Measurements on PDMS

The converged control inputs for the 12 different push-in rates, obtained in Sec. 3.3.2, were applied to measure the force-curves on the PDMS sample. We note that due to the difference of the tip-sample interaction on PDMS and on silicon, the obtained push-in rate and the cantilever vertical displacement range on the PDMS sample are different from those on the silicon sample, respectively. Particularly,

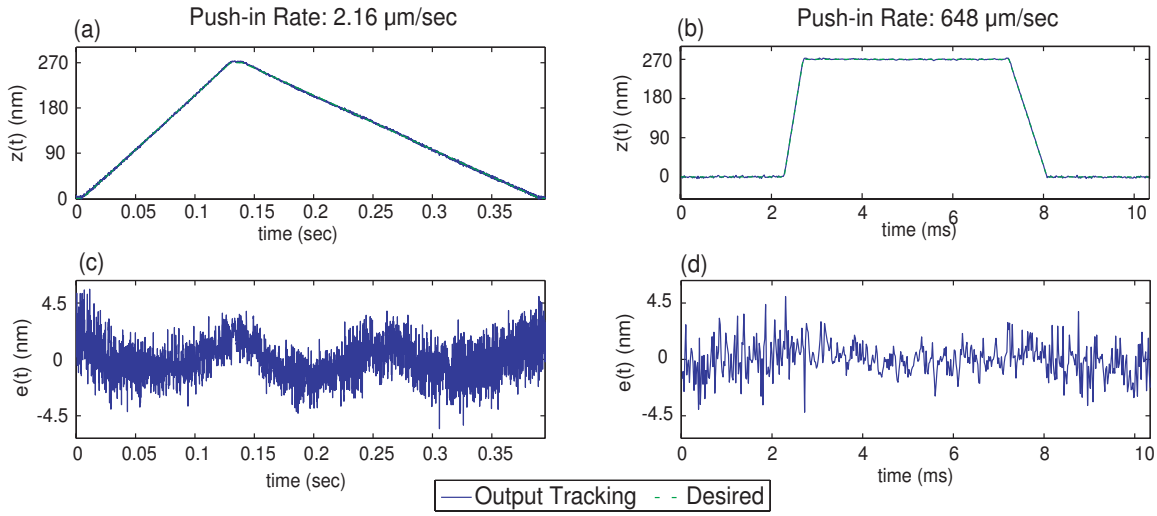

Figure 3.6 The plot of the cantilever vertical displacement during the push-in/retraction (load/unload) operation on the silicon calibration sample, obtained by using the EIIC technique, at the push-in rates of (a) 2.16 μm/sec and (b) 648 μm/sec, respectively. (c) and (d) show the corresponding positioning error with the desired trajectory.

non-constant push-in rate can be induced due to the soft contact between the cantilever and the AFM tip. However, our experiment results show that the deviation of the push-in rate from the constant push-in rate was very small and thus negligible. We calculated the push-in rates obtained on the PDMS sample for the 12 different control inputs, and further quantified the deviations of the cantilever deflection from the nominal trajectory (specified by the computed push-in rates). The deviations were quantified by using both the relative RMS error $E_2(\%)$ and the relative maximum error $E_{\max}(\%)$, and are shown in Table 3.2. By using the proposed EIIC technique, the variation of the push-in rates is still very small even when the push-in rate is as high as 777.4 μm/s (corresponding to the push-in rate of 848 μm/s obtained on silicon sample). This can also be seen from Fig. 3.7, where the cantilever vertical displacements for push-in rate of 1.7 μm/s and 565.2 μm/s are compared to the corresponding cantilever displacements obtained on the Silicon sample for push-in rates of 2.16 μm/s and 648 μm/s, respectively. Table 3.1 and Fig. 3.7 also show that the differences of the push-in rate and the (cantilever vertical) displacement, between the silicon sample and the PDMS sample, decrease as the push-in rate increased. This is because at the low push-in rate, PDMS exhibits a rubbery characteristic. As the push-in rate increases, however, the movements of PDMS molecules are significantly retarded since

they cannot follow the external deformation fast enough, thereby behaving like a stiff material (H-W. Hu. et al. (1992); S. Granick. et al. (1992)). As a result, the tip-sample interaction on PDMS becomes similar to the interaction on silicon, which in turn, leads to a similar push-in rates on these two different materials (Fig. 3.7 (b)) when the push-in rate is high. The experimental results, however, demonstrate that a desired constant push-in rate can be maintained by using the proposed EIIC technique on soft materials like PDMS during high-speed force-curve measurement.

Table 3.2 Tracking performance results ($E_2(\%)$ and $E_{max}(\%)$) during the push-in section of the force-curve, obtained by applying the converged EIIC control input to the PDMS sample.

Push-in Rate on Si (μm/s)	2.16	5.4	10.8	21.6	43.2	64.8
Push-in Rate on PDMS (μm/s)	1.7	4.4	9.0	18.5	36.9	56.4
$E_2(\%)$	0.39	0.47	0.71	0.67	1.11	0.66
$E_\infty(\%)$	0.84	1.11	1.45	0.96	3.24	1.17
Push-in Rate on Si (μm/s)	86.4	108	216	432	648	864
Push-in Rate on PDMS (μm/s)	75.3	95.2	193.5	384.9	565.2	777.6
$E_2(\%)$	0.70	0.84	0.97	1.59	2.50	2.86
$E_\infty(\%)$	1.60	1.52	2.22	3.09	4.71	4.98

The measured force-curves were analyzed using the Hertzian model to calculate the elastic modulus of PDMS at different push-in rates. First, the tip indentation was obtained as the difference of the cantilever vertical displacement of the PDMS and the silicon, as shown in Fig. 3.7 for the push-in rates of 1.7 μm/s and 565.2 μm/s, respectively. We note that the Si is not infinitely hard and might experiences slight deformation during the force-curve measurements. However, compared to the amount of tip indentation on the PDMS, such deformation was much smaller and thus negligible. Consequently, the force curves—the indentation vs. the force—were obtained for the 12 different push-in rates, and fitted by using the Hertzian model (see Eqs. (3.9, 3.11), Sec. 3.2.3) to find the elastic module of PDMS. The cantilever stiffness of 0.07 N/m has been experimentally calibrated (Sec. 3.3.1) and a nominal tip radius of 50 nm was used in the calculation. As an example, the force curves of PDMS for push-in rates of 1.7 μm/s and 565.4 μm/s are shown in Fig. 3.8, respectively.

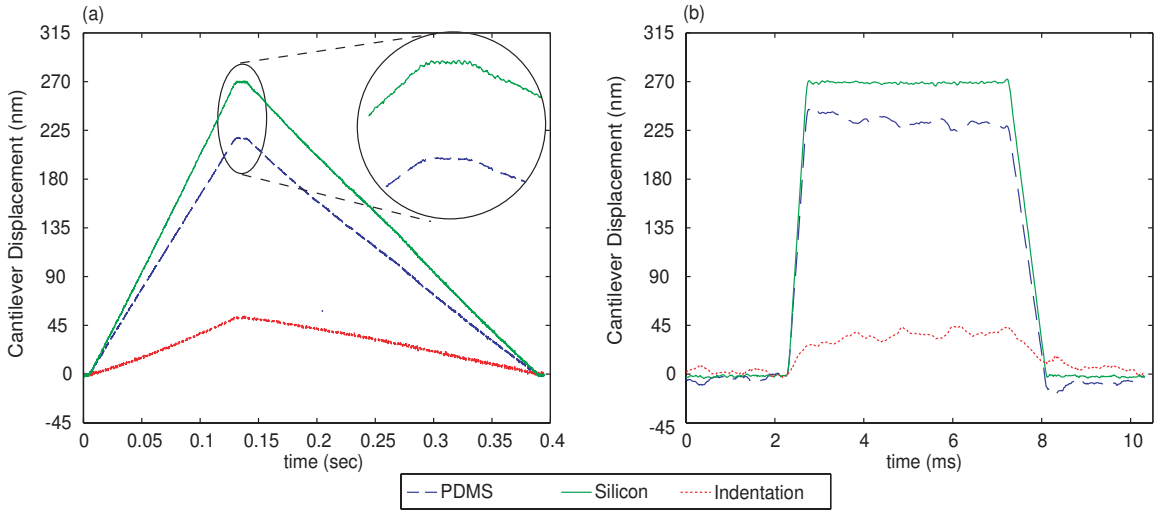

Figure 3.7 The comparison of the cantilever vertical displacement obtained by using the same control input for the push-in rate of (a) 2.16 μm/s on the silicon sample and 1.7 μm/s on the PDMS sample, and (b) 648 μm/s on the silicon sample and 565.4 μm/s on the PDMS sample. The corresponding displacement difference between the silicon and the PDMS measurements are also shown, which equals to the indentation of the tip into the PDMS sample during the measurement. The inset in (a) is the zoomed-in view of the flat portion of the trajectories.

Note that the Hertzian model was used to obtain the optimal fit (in the least-square sense) of the later part of the experimental force curve, and the difference between the experimental and the fitting curves at the beginning part of the curve represents the so called *zero-load plastic deformation* (i.e., the residual plastic deformation, see Fig. 3.8) (H.-J. Butt. et al. (2005)). Such a zero-load plastic deformation, as schematically denoted in Fig. 3.9, is generated because the force was applied repetitively on the PDMS sample—At each push-in rate, the push-in/retraction operation was repeated by 10 times, and the period is much shorter than the relaxation time of PDMS. Note that the zero-load plastic deformation depends on the kinetic energy applied to the PDMS sample during the operation (H.-J. Butt. et al. (2005)). Since the same force profile is applied during a longer time interval at low push-in rate than at high push-in rate, as a result, a larger amount of kinetic energy (applied to the PDMS), thereby a larger zero-load plastic deformation are generated at low push-in rate than at high push-in rate. This is veri-

fied by our experimental results. As shown in Fig. 3.10, the zero-load plastic deformation decreased as the push-in rate increased. Therefore, by using the proposed EIIC technique, force-curves of both hard and soft materials can be measured in a broad spectrum of push-in (and/or retraction) rates, spanning two-order difference.

Finally, the elastic modulus of the PDMS sample for the 12 different push-in rates were obtained, as plotted in Fig. 3.11. The variation of initial tip radius from 30nm to 70nm will cause a change of $+29.1\%$ to -15.5% in the computed modulus values.

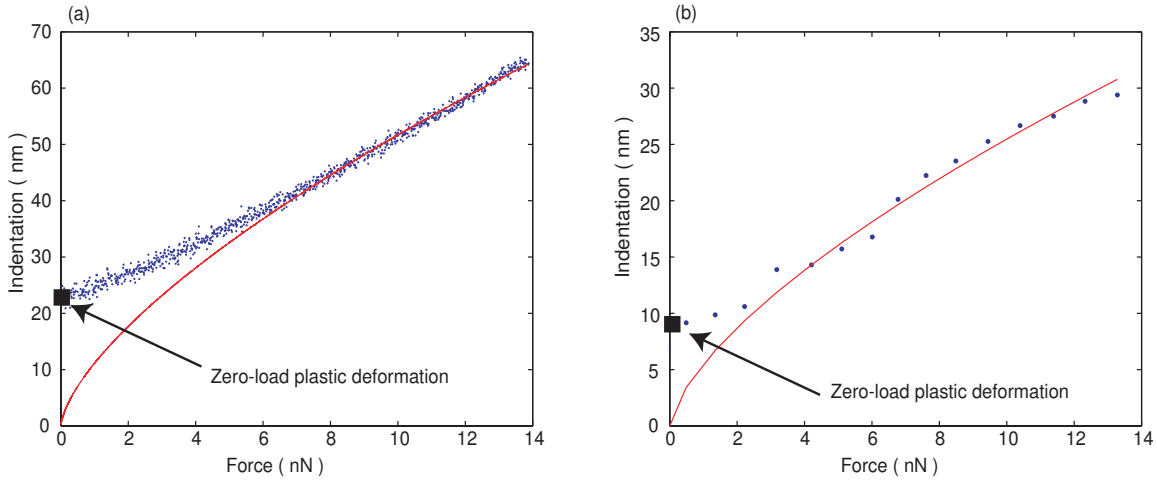

Figure 3.8 The force curve (blue-dotted) plotted as the tip indentation vs. the force applied for the push-in rate of (a) 1.7 μm/s and (b) 565.4 μm/s, along with comparison to the curve-fitting (red-line) obtained by using the Hertzian model, where the difference between the experimental and the fitted curves at the beginning portion represents the zero-load plastic deformation (H.-J. Butt. et al. (2005)).

3.3.5 DMA result

The viscoelastic properties of PDMS in bulk were characterized by DMA measurement (TA instrument, Q800). The storage modulus (E'), loss modulus (E''), and tan δ as a function of temperature ($-133 \sim 60\,^{\circ}$C) were obtained from a $20 \times 2 \times 7 mm^3$ sample under the tension mode at a frequency of 1 Hz and a heating rate of $5\,^{\circ}\mathrm{C}/min$.

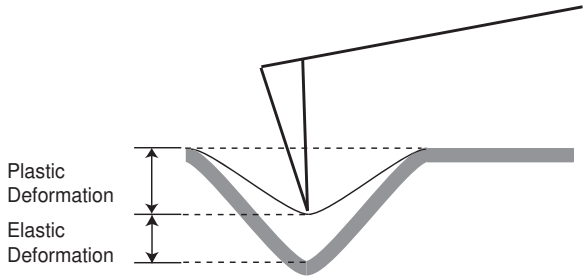

Figure 3.9 The schematic drawing to show the zero-load plastic deformation during the force-curve measurement.

3.3.6 Discussion

In case of Si, which is an elastic solid, the stress is always in phase with strain (i.e., the phase angle between stress and strain, $\delta = 0^\circ$). In contrast, the stress of the viscoelastic material, PDMS to the applied strain (i.e., the push-in force applied by the AFM tip in the present study) is out of phase with the strain, in which $0^\circ < \delta < 90^\circ$. When the push-in rate was low (e.g., 1.7 μm/s), the PDMS molecules were able to move (i.e., deform, and subsequently recover to their equilibrium conformation) in response to the applied deformation. So the modulus (E') compares well to that obtained in the DMA measurement. As shown in Fig. 3.11, the value of the PDMS elastic modulus at low push-in rate of 1.7 μm/s (equivalent to a push-in/retraction frequency of 2.53 Hz), estimated by using the AFM experimental data, is at $\sim$2 MPa, while the elastic modulus value obtained from the DMA measurement at the frequency of 1 Hz and the same room temperature (25.5 $^\circ C$) is at 1.56 MPa, as pointed out in Fig. 3.12. However, as the rate of external deformation increased by more than 2 orders of magnitude (e.g., 565.4 μ m/s), the PDMS molecules cannot move fast enough to follow the imposed external deformation, thereby behaving like a stiff material. This led to a dramatic increase in the elastic modulus E', as evidenced in Fig. 3.11.

Time Temperature Superposition (TTS) principle is widely applied to characterize material response of viscoelastic polymeric materials (J. D. Ferry. et al. (1980)). According to TTS, material response at low (high) temperature is similar to response at high (low) frequency loadings. At low temperatures or under high frequency loadings, polymers behave as a stiff or glassy solid. While at high tempera-

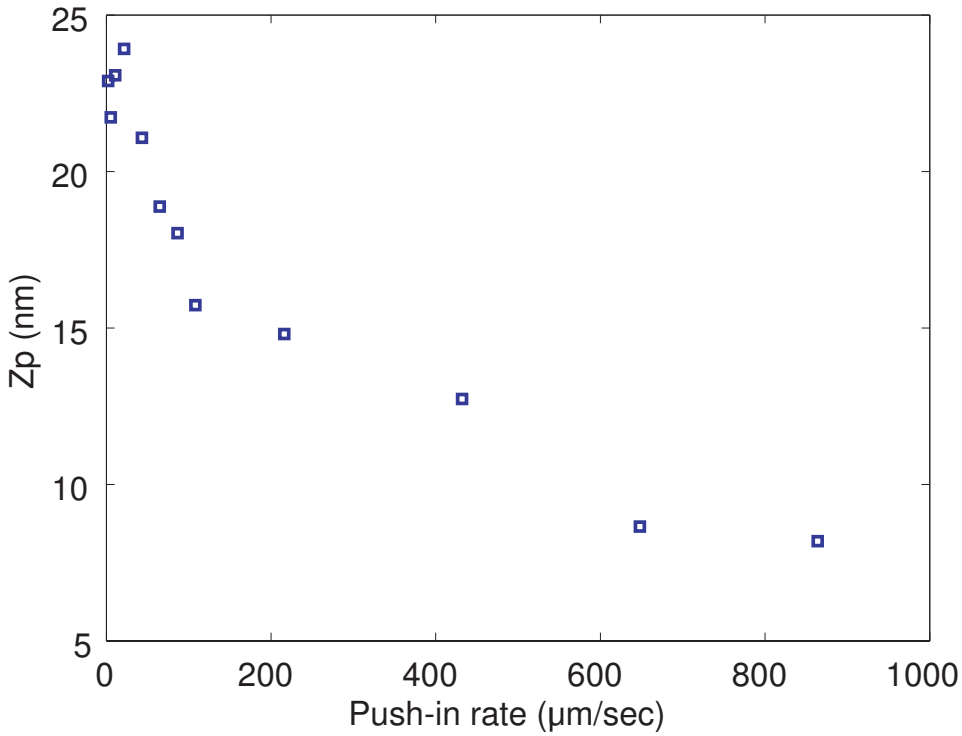

Figure 3.10 The zero load plastic deformation depth z_p obtained at different push-in rates.

tures or low frequency loading, polymer molecules are mobile and as a result lower modulus values are measured. Following TTS principle, PDMS response determined using fits of high-speed force displacement curves (Fig. 3.11) can be qualitatively compared to storage modulus measured using DMA (Fig. 3.12). As the loading rate is increased, PDMS modulus increases from about 2 MPa to about 6 MPa and similar magnitude of change in storage modulus is observed as the temperature is decreased from room temperature. Note that results of the DMA test are used to demonstrate the viscoelastic nature of PDMS sample investigated in the study. Comparison of the force displacement and DMA test results indicates that the current control technique may be utilized to measure the time dependent modulus. Magnitude of the modulus determined from force displacement relationship is higher than that measured using DMA because of the limitations in analytical model of contact between tip and sample. In previous work VanLandingham and co-workers (C. White. et al. (2005)) have noted that mechanics of contact between indenting tip and sample surface is not correctly captured by analytical Hertzian models. This limitation of contact mechanics models leads to consistent overestimation of

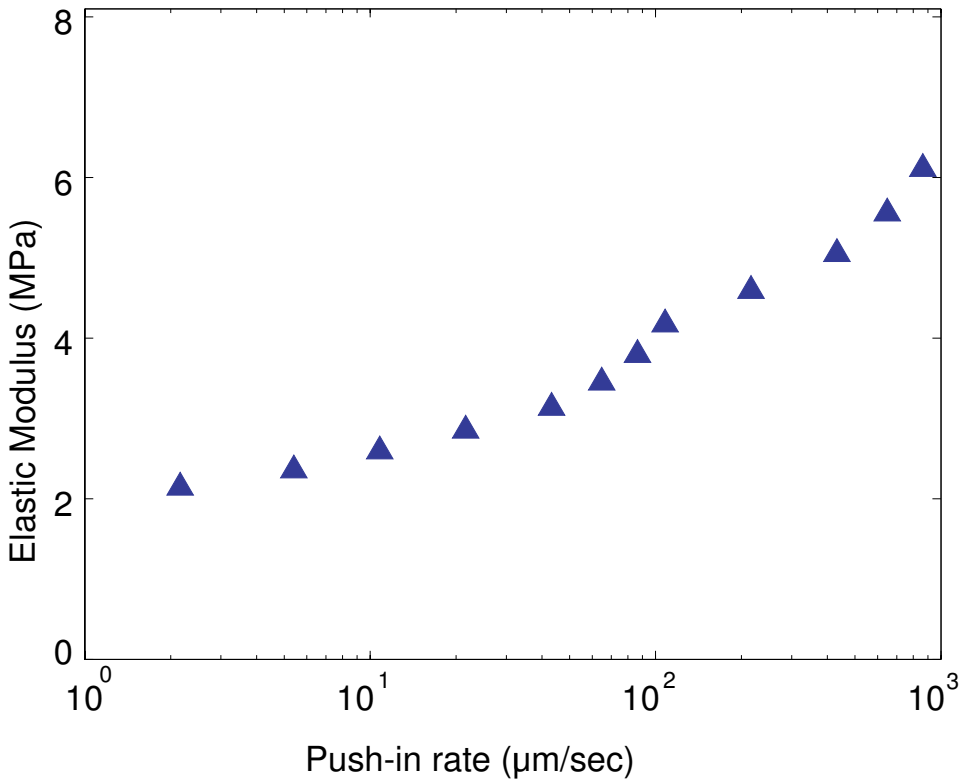

Figure 3.11 The elastic modulus of PDMS at different push-in rates, estimated by using the Hertzian model with the AFM experimental data, where the triangles denote the values obtained by using the nominal AFM tip radius of 50 nm. The variation of the tip radius from 30nm to 70nm will cause a change of $+29.1\%$ to -15.5% in the computed modulus values.

modulus measured from indentation experiments in comparison to bulk measurements (C. White. et al. (2005)). Since the focus of this paper is on development and demonstrate the iterative control algorithm for high-speed force measurement, a simple analytical (Hertzian) model was utilized to extract the modulus. Therefore, the correlation between modulus determined from high speed force-displacement and DMA clearly indicates that our technique may be used for characterization of material time dependent response.

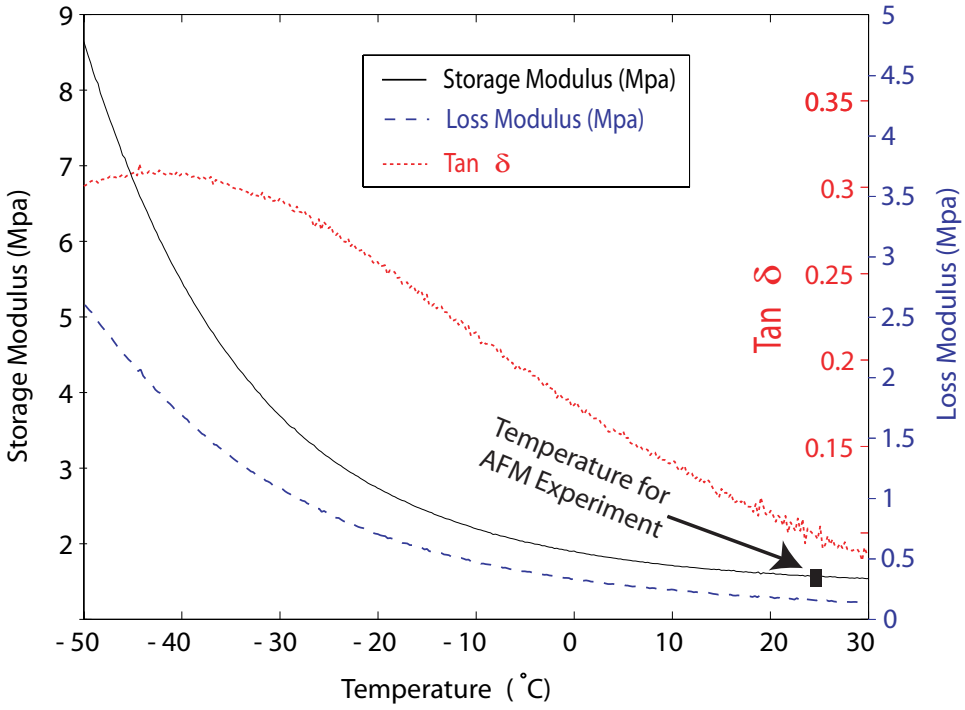

Figure 3.12 The storage modulus (E'), loss modulus (E''), and $\tan\delta$ of PDMS as a function of temperature measured by DMA.

3.4 Conclusions

In this chapter, we presented a novel enhanced inversion-based iterative control (EIIC) technique to achieve high-speed force-distance measurement using AFM, and implemented it to measure the time-dependent elastic modulus of poly(dimethylsiloxane) (PDMS). The experimental results showed that the proposed EIIC technique can effectively remove the effect of the AFM dynamics (from the piezotube actuator to the cantilever along with the mechanical connection in between) during high-speed force-curve measurements. A push-in or retraction rate as high as 864 μm/sec (over 80 times faster) were achieved with no loss of spatial resolution. The time-dependent elastic-modulus of PDMS was obtained by measuring the force-curve measurements with different push-in rates, and utilizing the measurements on a hard (silicon) sample and on the PDMS in the Hertzian contact model. The obtained values of the elastic modulus were compared with the results from the DMA test of the PDMS. As we expected, the elastic (storage) modulus value obtained from the DMA test compared well with our experimental result at low push-in rate ($\sim$1.7 μm/s), and the measured elastic modulus

increased as the push-in rate increased, signifying that a faster external deformation rate transitions the viscoelastic response of PDMS from that of a rubbery material toward a glassy one. Compared with other approaches, the proposed EIIC technique has advantages including being readily applied to current AFM system with minor hardware modification/updates, robust to system/operation variations (because such variations can be compensated for via iterations), and possibly achieving measurement precision beyond the signal noise limit (the signal noise effect can be significantly reduced using averaging methods, as the control input is computed off-line iteratively,). Therefore, we expect that the proposed high-speed force-curve measurement techniques can be readily implemented in various material characterization/synthesis applications.

CHAPTER 4. Model-less Inversion-based Iterative Control for Output Tracking: Piezoelectric Actuator Example

A paper A paper submitted to the ASME Journal of Dynamic Systems, Measurement and Control

Abstract

In this chapter, we propose a model-less inversion-based iterative control (MIIC) approach for high-speed output tracking in repetitive applications such as the lateral scanning during atomic force microscope (AFM) imaging. The MIIC algorithm extends the inversion-based iterative control (IIC) technique and the enhanced inversion-based iterative control (EIIC) technique. It has been demonstrated that these two recently-developed techniques can effectively compensate for the linear dynamics as well as the nonlinear hysteresis effects of systems such as the piezotube actuator used for positioning on AFM. The IIC algorithm, however, can be sensitive to the dynamics uncertainty of the system dynamics. The development of the EIIC algorithm removes such dynamics-uncertainty-caused constraints, by decoupling the iteration of the input amplitude from the iteration of the input phase (in frequency domain). However, the implementation of these two techniques requires modeling the system dynamics, which can be time consuming and prone to errors. Thus, the main contribution of this chapter is the development of the MIIC algorithm to eliminate the modeling process while further enhancing the output tracking performance. The disturbance and/or measurement noise effect is explicitly considered in the convergence analysis of the MIIC algorithm. It is shown that convergence can be reached in one iteration step if the noise/disturbance effect is negligible. Otherwise, the input error is quantified by the disturbance/noise to signal ratio (NSR, relative to the desired trajectory); and the upper bound of the NSR for guaranteeing the MIIC algorithm to improve tracking is also quantified.

The MIIC is applied to a piezotube scanner on an Atomic Force Microscope, and experimental results are presented to demonstrate the efficacy of the MIIC technique.

4.1 Introduction

In this chapter, we propose a new model-less inversion-based iterative control (MIIC) technique for high-speed precise output tracking. It is noted that precise tracking of periodic trajectories at high-speed is needed in applications such as the nano-scale imaging/measurement using atomic force microscope (AFM) (R. Wiesendanger. (1994); Kees O. van Werf. et al. (1994)), the scanning mechanism on MEMS-based micro-mirrors (F. Filhol. et al. (2005); F. Zimmer. et al. (2005)), the quick-return mechanisms and cams in manufacturing (R.-F. Fung. et al. (2000)), and the manufacturing process in rapid prototyping (S. Huang. et al. (2005)). For example, in atomic force microscope (AFM) imaging, repetitive precise scanning at high-speed is needed to achieve high-speed imaging, which not only improves the throughput, but more importantly, enables the interrogation of nanoscale dynamic processes (R. Wiesendanger. (1994); F. Zimmer. et al. (2005)). It has been shown that iterative learning control (ILC) is quite efficient in tracking repetitive trajectories (R. Horowitz. et al. (1991); K. Krishnamoorthy. et al. (2004); M. R. Graham. et al. (2006); L. Moore. et al. (2000)). Limits, however, exist in conventional ILC designs (M. Verwoerda. et al. (2006)) because causal controllers were used in these designs. As a result, the noncausality (i.e., the "preview" of the future desired trajectory as well as the predicted output of the system) was not exploited to improve the tracking, particularly for nonminimum-phase systems (M. Verwoerda. et al. (2006)). Such a limit is alleviated in the IIC and the EIIC techniques. Although the IIC and the EIIC techniques utilize the noncausality to improve the tracking precision, as illustrated in (S. Tien. et al. (2005); Y. Wu. et al. (2007)), their performance depends on the quality of the system dynamics model, whereas modeling process is time-consuming and prone to errors. Thus, the main contribution of this paper is the development of the MIIC technique which eliminates the need for the dynamics model while further enhances the output tracking performance.

Iterative learning control approach (L. Moore. et al. (2000); Moore, Kelvin. et al. (1993); Jian-Xin

Xu. et al. (2003)) has been effective in output tracking in repetitive operations. Compared to feedback control methods, the ILC approach avoids the potential stability issues caused by the high feedback gain (needed to achieve precise tracking). Instead, a learning mechanism is introduced in the ILC approach to utilize the repetitive nature of the applications to improve the tracking performance (Q. Zou. et al. (2004); S. Salapaka. et al. (2002)). Moreover, ILC approach also has the advantages such as being ease to design and implement—as precise model usually is not required in ILC algorithms. ILC techniques have been successfully implemented in various applications (C. Cloet. et al. (2001)). The majority of the ILC algorithms aims at obtaining a stable controller based on, for example, H_∞ robust control theory (Gaspar, P.. et al. (1998)). Such a stable controller, however, limits the ILC method in exploring the noncausality provided by the knowledge of the entire output tracking through iterations. Particularly, we note that it has been shown recently (M. Verwoerda. et al. (2006)) that a causal IIC controller is essentially equivalent to a feedback controller. Therefore, constraints exist in the conventional ILC approaches.

Such causality-related constraints in the ILC approaches are removed in the development of the inversion-based iterative control approaches (J. Ghosh. et al. (2002); S. Tien. et al. (2005); Y. Wu. et al. (2007); K. Kim. et al. (2007)). Particularly, the IIC approach utilizes the inverse of the system dynamics a frequency-domain implementation scheme (S. Tien. et al. (2005); Y. Wu. et al. (2007)). The convergence of the IIC algorithm, however, can be sensitive to the dynamic uncertainties of the system, i.e., the phase uncertainty of the system dynamics must be less $\pi/2$ to guarantee the convergence (S. Tien. et al. (2005)). To improve the robustness of the IIC technique against the phase uncertainty, the enhanced inversion-based iterative control technique (EIIC) was proposed. In the EIIC method, the updating of the input magnitude is decoupled from the updating of the input phase (in frequency-domain). Thereby, the EIIC approach can achieve convergence in a larger frequency range at a faster convergence rate. The efficacy of the IIC and the EIIC algorithms has been demonstrated through experiments to achieve high-speed precise scanning (Y. Wu. et al. (2007)), and to compensate-for the cross-axis coupling-caused vibrations of piezotube actuators (S. Tien. et al. (2005)). However, both the IIC and the EIIC algorithms require a reasonably-good model of the system dynamics, and the the

convergence rate (i.e., the choice of the iterative coefficient) is determined by the model accuracy. We note that system dynamics modeling is time consuming and prone to errors, and in many applications, the measured dynamics response depends on the operation condition, which can also vary significantly from time to time (for example, the positioning dynamics on AFM system). Therefore, there exists need to overcome the modeling-related constraints in the ILC approaches.

The main contribution of the chapter is the development of the MIIC technique. The MIIC algorithm does not require the modeling of the system dynamics, therefore, the constraints related to the modeling process, and the requirement for a good dynamics model are removed. Instead, in the MIIC algorithm, the input-output relation of the system is iteratively updated by using the measured input-output signals. We note that a similar idea was utilized before in the adaptive ILC approaches (Francois Padieu. et al. (1990); K. L. Moor. et al. (1992)). Fundamental differences, however, exist between the proposed MIIC technique and the adaptive ILC approaches in that how such online updating is utilized: In the adaptive ILC approaches (Francois Padieu. et al. (1990); K. L. Moor. et al. (1992)), a dynamics model is used and the measured input-output signals are used to update the model; Whereas in the proposed method, no dynamics model is needed, and the measured input-output signals are used to update the iterative control input directly. Moreover, we explicitly address the disturbance/noise effects—which was not considered in (Francois Padieu. et al. (1990); K. L. Moor. et al. (1992))—in the convergence analysis of the proposed MIIC algorithm. We show that the convergence of the MIIC algorithm can be achieved in one iteration when the noise/disturbance effect is negligible; Or, the input error is quantified by the disturbance/noise to signal ratio (NSR, relative to the desired trajectory) when the disturbance and/or noise effects are considered. The size of NSR for the MIIC algorithm to be effective (i.e., the tracking error is smaller when using the MIIC algorithm than that when not using it) is further quantified. We illustrate the proposed MIIC technique by implementing it in experiments to the output tracking of a piezotube actuator on an AFM system. Two types of trajectories are used to evaluate the tracking performance with comparison to the IIC algorithm: triangular trajectories and band-limited white-noise type of trajectories. Experimental results show that precise output tracking is achieved in both cases, whereas the IIC algorithm failed to track the complicated band-limited white-noise trajecto-

ries. Moreover, the MIIC algorithm is also implemented to compensate-for the hysteresis effect when tracking large-range triangle trajectory at high-speed. Experimental results show that precise output tracking can also be achieved.

The rest of the paper is organized as follows. The MIIC algorithm and its convergence analysis are presented in Section II, followed by the experimental implementation of the proposed technique and discussion in Section III. Our conclusions are given in section IV.

4.2 Model-less Inversion-based Iterative Control

We start with briefly reviewing the inversion-based iterative control (S. Tien. et al. (2005); Q. Zou. et al. (2005)) and the enhanced inversion-based iterative control algorithm. These two control algorithms form the base for the proposed MIIC algorithm.

4.2.1 Inversion-based Iterative Control (IIC) and Enhanced Inversion-based Iterative control (EIIC)

IIC Algorithm (S. Tien. et al. (2005)) Recently, an inversion-based iterative control technique (S. Tien. et al. (2005); Y. Wu. et al. (2007)) was developed to achieve high-speed output tracking of periodic trajectories. For a stable, single input single output (SISO) linear time invariant (LTI) system, the IIC control law can be described in the frequency-domain as

$$\begin{aligned} u_0(j\omega) &= G_m(j\omega)^{-1} y_d(j\omega), & k=0 \\ u_k(j\omega) &= u_{k-1}(j\omega) + \rho(\omega) G_m(j\omega)^{-1} [y_d(j\omega) - y_{k-1}(j\omega)] & k \geq 1 \end{aligned} \tag{4.1}$$

where '$f(j\omega)$' denotes the Fourier transform of the signal '$f(t)$', '$y_d(\cdot)$' denotes the desired output trajectory, '$y_k(\cdot)$' denotes the output obtained by applying the input '$u_k(\cdot)$' to the system during the k^{th} iteration, $\rho(\omega) > 0$ is the iterative coefficient, and $G_m(j\omega)$ denotes the frequency response model of the system. It has been shown that the above IIC algorithm can lead to exact tracking of the desired trajectory at frequency ω, provided that the modeling error is not too large and the iterative coefficient

is appropriately chosen (S. Tien. et al. (2005)). More specifically, the convergence of the IIC algorithm is given in the following lemma 2.

Lemma 2 *(S. Tien. et al. (2005)) At any given frequency ω, let both the actual dynamics of a SISO LTI system $G(j\omega)$ and its model $G_m(j\omega)$ be stable and hyperbolic (i.e., both have no zeros on the $j\omega$ axis), and the dynamics uncertainty $\Delta G(j\omega)$ be described as*

$$\begin{aligned} \Delta G(j\omega) &= \frac{G(j\omega)}{G_m(j\omega)} = \frac{|G(j\omega)|e^{j\angle G(j\omega)}}{|G_m(j\omega)|e^{j\angle G_m(j\omega)}} \\ &\triangleq |\Delta G(\omega)|\, e^{j\Delta\angle G(j\omega)}, \end{aligned} \tag{4.2}$$

then the IIC control law converges at frequency ω to the desired input $u_d(j\omega) \triangleq G(j\omega)^{-1} y_d(j\omega)$, i.e., $\lim_{k\to\infty} u_k(j\omega) = u_d(j\omega)$*, if and only if,*

1) the iterative coefficient $\rho(\omega) \in \mathbb{R}$ is chosen as

$$0 < \rho(\omega) < \rho_{sup}(\omega) \triangleq \frac{2\cos(\angle\Delta G(j\omega))}{|\Delta G(j\omega)|} \tag{4.3}$$

2) the magnitude of the phase variation is less than $\pi/2$, i.e.,

$$|\angle\Delta G(j\omega)| < \frac{\pi}{2} \tag{4.4}$$

The IIC algorithm has been successfully implemented in applications such as the compensation for the cross-axis coupling effects of piezoelectric tube actuator (S. Tien. et al. (2005)), and the high-speed precise tracking of driving wave forms for inertial reaction devices (Q. Zou. et al. (2005)). Moreover, it has also been shown recently that the IIC method can compensate for both the hysteresis and the vibrational dynamics effects of piezotube actuators (Y. Wu. et al. (2007)). The convergence of the IIC algorithm (Eq. (4.1)), however, can be sensitive to phase uncertainties of the system dynamics, particularly at frequencies where the phase uncertainty is close to $\pi/2$, for example, near the resonant peaks of the system dynamics. On the contrary, we note that regardless the phase relation between the desired output and the current output, if the output amplitude in current iteration is larger than the

desired output amplitude at frequency ω, then the input amplitude at that frequency should become smaller in the next iteration than that in current iteration, and vise versa. However, such an updating mechanism is not realized in the IIC algorithm. To that end, the following EIIC algorithm has been proposed.

EIIC Algorithm The EIIC control law is also given in the frequency-domain as follows,

$$\begin{cases} u_0(j\omega)) = G_m(j\omega)^{-1} y_d(j\omega) & k=0 \\ |u_k(j\omega)| = |u_{k-1}(j\omega)| + \rho(\omega)\left|G_m^{-1}(j\omega)\right|[|y_d(j\omega)| - |y_{k-1}(j\omega)|] & k \geq 1 \\ \angle u_k(j\omega) = \angle u_{k-1}(j\omega) + (\angle(y_d(j\omega)) - \angle y_{k-1}(j\omega)) & \end{cases} \tag{4.5}$$

As shown in Eq. (4.5), the updating of the input magnitude is decoupled from the updating of the phase angle in the EIIC algorithm. As a result, the EIIC algorithm can converge in a larger frequency range and at a faster convergence rate than IIC algorithm.

Lemma 3 *For any given frequency value ω, let $G(j\omega)$, $G_m(j\omega)$ and $\Delta G(j\omega)$ be defined as in Lemma 2, respectively. Then the input of the EIIC law converges to the desired input $u_d(j\omega)$, i.e.,*

$$\lim_{k\to\infty} |u_k(j\omega)| = |u_d(j\omega)|, \ \textit{and} \ \lim_{k\to\infty} \angle u_k(j\omega) = \angle u_d(j\omega),$$

if and only if the iterative coefficient $\rho(\omega)$ is chosen as

$$0 < \rho(\omega) < \rho_{sup}(\omega) \triangleq \frac{2}{|\Delta G(j\omega)|} \tag{4.6}$$

The efficacy of the EIIC algorithm has been illustrated through experiments including the measurement of adhesion force measurement at high-speed using AFM , and the measurement of the time-dependent elastic modulus of a polymer material (Polydimethylsiloxane, PDMS) (K.-S. Kim. et al. (2007)).

Remark 4 *The EIIC law extends the IIC control law (4.1) in two aspects (S. Tien. et al. (2005)): 1). The phase condition needed for the convergence of the IIC law (Eq. (4.4)) is removed in the EIIC*

law, thereby the convergence frequency range of the EIIC law is larger; and 2). The range of the iterative coefficient $\rho(\omega)$ to guarantee the convergence also becomes larger — for any nonzero phase uncertainty, the upper bound of $\rho(\omega)$ for the convergence of the EIIC law (Eq. (4.6)) is larger than that for the IIC law (Eq. (4.1)), i.e., $2/|\Delta G(j\omega)| \geq 2\cos(\Delta G(j\omega))/|\Delta G(j\omega)|$.

Remark 5 *The frequency-domain implementation of the IIC and the EIIC algorithms provides a natural and straightforward avenue to explore the noncausality in the iterative control, particularly for non-minimum-phase systems. This is in contrast to the time-domain, causal ILC algorithms (Peter B. Goldsmith. et al. (2002)). Recently it is shown (Kelvin L. Moor. et al. (1999); M. Verwoerda. et al. (2006)) that the advantages of the iterative control approach mainly lie in the utilization of the noncausality gained from the repetitive nature in applications, and a causal ILC algorithm is equivalent to a feedback controller. Therefore, the IIC algorithm and the EIIC algorithm are very efficient in achieving precise positioning control at high-speed (S. Tien. et al. (2005); Y. Wu. et al. (2007); K. Kim. et al. (2007)).*

The implementation of the IIC and the EIIC algorithms, however, requires a reasonably-good model of the system dynamics, while the modeling process can be time consuming and prone to errors. Thus, the success of the IIC and EIIC algorithms and the challenges involved in the dynamics modeling motivate the development of the following model-less inversion-based iterative control.

4.2.2 Model-less Inversion-based Iterative Control (MIIC)

The proposed MIIC algorithm is given below,

$$\begin{aligned} u_0(j\omega) &= \alpha y_d(j\omega), && k=0, \\ u_k(j\omega) &= \begin{cases} \frac{u_{k-1}(j\omega)}{y_{k-1}(j\omega)} y_d(j\omega), & \text{when } y_k(j\omega)\neq 0 \quad \text{and } y_d(j\omega)\neq 0 \\ 0 & \text{otherwise} \end{cases} && k\geq 1, \end{aligned} \tag{4.7}$$

where $\alpha \neq 0$ is a pre-chosen constant (e.g., α can be chosen as the estimated DC-Gain of the system).

Remark 6 *Comparing Eq. (4.5) with Eq. (4.7), we see that the EIIC law is transformed to the MIIC law by replacing the inverse dynamics model $G_m^{-1}(j\omega)$ with $u_{k-1}(j\omega)/y_{k-1}(j\omega)$ and setting $\rho(\omega)=1$ in Eq. (4.5). Thus, essentially the proposed MIIC technique introduces an iterative adaptation mechanism into the inversion-based iterative control approach.*

Next, we discuss the convergence of the MIIC algorithm upon the additional disturbance and/or measurement noise.

Theorem 2 *Let $G(j\omega)$ be a stable SISO LTI system, then at frequency ω,*

1. *if the disturbance (and/or noise) effects are negligible, then the MIIC algorithm converges after one iteration, i.e.,*

$$u_1(j\omega) = u_d(j\omega), \tag{4.8}$$

2. *if the system output $y(j\omega)$ is effected by the disturbance and/or the measurement noise as*

$$y(j\omega) = y_l(j\omega) + y_n(j\omega), \tag{4.9}$$

where $y_l(j\omega)$ denotes the linear part of the system response to the input $u(j\omega)$, i.e. $y_l(j\omega) = G(j\omega)u(j\omega)$, and $y_n(j\omega)$ denotes the output component caused by the disturbances and/or measurement noise. Then at the k^{th} iteration, the ratio of the iterative control input to the desired input is given by:

$$\frac{u_k(j\omega)}{u_d(j\omega)} = \frac{G(j\omega)}{G(j\omega)\,(1+S_k(j\omega)) + P_k(j\omega)/\alpha} \quad , \quad \forall \;\; k \geq 1 \tag{4.10}$$

where $P_k(j\omega)$ denotes the product of the noise/disturbance-to-signal (NSR) ratios (relative to the desired output $y_d(j\omega)$) at frequency ω from all the past iterations, and $S_k(j\omega)$ denotes the

summation of the product $P_k(j\omega)$,

$$\begin{aligned} P_k(j\omega) &= \prod_{i=0}^{k-1} \frac{y_{i,n}(j\omega)}{y_d(j\omega)}, \\ S_k(j\omega) &= \begin{cases} 0, & \text{for} \quad k=1 \\ \Sigma_{j=1}^{k-1} \Pi_{i=1}^{j} \frac{y_{k-i,n}(j\omega)}{y_d(j\omega)}, & \text{for} \quad k \geq 2 \end{cases} \end{aligned}$$

Proof We start with showing Result 1). Equation (4.8) follows directly by substituting the output of the system after the initial input (k=0), $y_0(j\omega) = G(j\omega)u_0(j\omega)$, back into the MIIC law

$$\begin{aligned} u_1(j\omega) &= \frac{u_0(j\omega)}{y_0(j\omega)} y_d(j\omega) \\ &= \frac{u_0(j\omega)}{G(j\omega)u_0(j\omega)} y_d(j\omega) \\ &= u_d(j\omega). \end{aligned} \tag{4.11}$$

To show Result 2), rewrite the iterative control input at the k^{th} iteration by combining Eq. (4.7) with Eq. (4.9)

$$\begin{aligned} u_k(j\omega) &= \frac{u_{k-1}(j\omega)y_d(j\omega)}{G(j\omega)u_{k-1}(j\omega) + y_{k-1,n}(j\omega)} \\ &= \frac{G(j\omega)u_d(j\omega)}{G(j\omega) + \ y_{k-1,n}(j\omega)/u_{k-1}(j\omega)}, \end{aligned} \tag{4.12}$$

which yields

$$\frac{u_k(j\omega)}{u_d(j\omega)} = \frac{G(j\omega)}{G(j\omega) + \ y_{k-1,n}(j\omega)/u_{k-1}(j\omega)} \tag{4.13}$$

Next, we proceed by using the induction method. First, Formula (4.10) holds at the first iteration,

$$\begin{aligned} \frac{u_1(j\omega)}{u_d(j\omega)} &= \frac{G(j\omega)}{G(j\omega) + \ y_{0,n}(j\omega)/u_0(j\omega)} && \text{(by Eq. (4.13))} \\ &= \frac{G(j\omega)}{G(j\omega) + \ y_{0,n}(j\omega)/\alpha y_d(j\omega)} && \text{(by the choice of} \quad u_0(j\omega) = \alpha y_d(j\omega)) \end{aligned}$$

Secondly, we assume that Eq. (4.10) holds at the k^{th} iteration, then at the $k+1^{th}$ iteration,

$$\begin{aligned}
\frac{u_{k+1}(j\omega)}{u_d(j\omega)} &= \frac{G(j\omega)}{G(j\omega)+\frac{y_{k,n}(j\omega)}{u_k(j\omega)}} \\
&= \frac{G(j\omega)}{G(j\omega)+\frac{y_{k,n}(j\omega)}{G(j\omega)u_d(j\omega)}\left[G(j\omega)\left(1+S_k(j\omega)\right)+P_k(j\omega)/\alpha\right]} \\
&\qquad \text{(by the assumption that Eq. (4.10) holds at the } k^{th} \text{ iteration)} \\
&= \frac{G(j\omega)}{G(j\omega)+G(j\omega)\frac{y_{k,n}(j\omega)}{y_d(j\omega)}(1+S_k(j\omega))+\frac{y_{k,n}(j\omega)}{y_d(j\omega)}P_k(j\omega)/\alpha} \qquad (4.14) \\
&\qquad \text{(by } y_d(j\omega)=G(j\omega)u_d(j\omega)\text{)}
\end{aligned}$$

Notice that

$$\begin{aligned}
\frac{y_{k,n}(j\omega)}{y_d(j\omega)}(1+S_k(j\omega)) &= \frac{y_{k,n}(j\omega)}{y_d(j\omega)}+\frac{y_{k,n}(j\omega)}{y_d(j\omega)}\sum_{j=1}^{k-1}\prod_{i=1}^{j}\frac{y_{k-i,n}(j\omega)}{y_d(j\omega)} \\
&= \frac{y_{k,n}(j\omega)}{y_d(j\omega)}+\frac{y_{k,n}(j\omega)}{y_d(j\omega)}\sum_{j=2}^{k}\prod_{i=2}^{j}\frac{y_{k+1-i,n}(j\omega)}{y_d(j\omega)} \\
&= \frac{y_{k,n}(j\omega)}{y_d(j\omega)}+\sum_{j=2}^{k}\prod_{i=1}^{j}\frac{y_{k+1-i,n}(j\omega)}{y_d(j\omega)} \\
&= \sum_{j=1}^{k}\prod_{i=1}^{j}\frac{y_{k+1-i,n}(j\omega)}{y_d(j\omega)}, \qquad (\text{for } \; k\geq 2) \\
&= S_{k+1}(j\omega) \qquad (4.15)
\end{aligned}$$

and

$$\begin{aligned}
\frac{y_{k,n}(j\omega)}{y_d(j\omega)}P_k(j\omega) &= \frac{y_{k,n}(j\omega)}{y_d(j\omega)}\prod_{i=0}^{k-1}\frac{y_{i,n}(j\omega)}{y_d(j\omega)}, \\
&= \prod_{i=0}^{k}\frac{y_{i,n}(j\omega)}{y_d(j\omega)}, \\
&= P_{k+1}(j\omega) \qquad (4.16)
\end{aligned}$$

Substituting the above Eqs. (4.15, 4.16) back into Eq. (4.14) shows the Eq. (4.10) holds at the $(k+1)^{th}$ iteration, thereby, holds for all $k\geq 1$—by induction. This completes the proof. ■

The next theorem finds the bound of the MIIC input relative to the desired input, and quantifies the upper-bound of the NSR at a given frequency for guaranteeing the improvement of the output tracking by using the MIIC algorithm, i.e., below which the output tracking at that frequency will be better by using the MIIC algorithm than not tracking that frequency component.

Theorem 3 *Let assumptions in Theorem 2 be satisfied,*

1. *assume that during each iteration, the NSR is bounded above by a positive, less-than-half constant $\varepsilon(\omega)$, i.e.,*

$$\left|\frac{y_{k,n}(j\omega)}{y_d(j\omega)}\right| \leq \varepsilon(\omega) < 1/2, \quad \forall\ k \tag{4.17}$$

then the ratio of the iterative input to the desired input is bounded in magnitude and phase, respectively, as

$$R_{\min}(\omega) \triangleq 1-\varepsilon(\omega) \leq \lim_{k\to\infty}\left|\frac{u_k(j\omega)}{u_d(j\omega)}\right| \leq \frac{1-\varepsilon(\omega)}{1-2\varepsilon(\omega)} \triangleq R_{\max}(\omega) \tag{4.18}$$

$$\lim_{k\to\infty}\left|\angle\left(\frac{u_k(j\omega)}{u_d(j\omega)}\right)\right| \leq \sin^{-1}\left(\frac{\varepsilon(\omega)}{1-\varepsilon(\omega)}\right) \triangleq \theta_{\max}(\omega), \tag{4.19}$$

and the relative tracking error is bounded as

$$\lim_{k\to\infty}\left|\frac{y_k(j\omega)-y_d(j\omega)}{y_d(j\omega)}\right| \leq \frac{2\varepsilon(\omega)(1-\varepsilon(\omega))}{1-2\varepsilon(\omega)}; \tag{4.20}$$

2. *The use of the MIIC algorithm will improve the tracking at frequency ω, i.e.,*

$$\lim_{k\to\infty}\left|\frac{y_k(j\omega)-y_d(j\omega)}{y_d(j\omega)}\right| < 1, \tag{4.21}$$

if the NSR is bounded above by $1-\frac{\sqrt{2}}{2} \approx 0.3$, i.e.,

$$\left|\frac{y_{k,n}(j\omega)}{y_d(j\omega)}\right| \leq \varepsilon(\omega) < 1-\frac{\sqrt{2}}{2}, \quad \forall\ k \tag{4.22}$$

Proof To show Result 1), note that if the NSR is less than 1, then the term $P_k(j\omega)/\alpha$ in Eq. (4.13) converges to zero,

$$\begin{aligned}\lim_{k\to\infty}|P_k(j\omega)/\alpha| &= \lim_{k\to\infty}\left|\frac{1}{\alpha}\prod_{i=0}^{k-1}\frac{y_{i,n}(j\omega)}{y_d(j\omega)}\right| \\ &= 0\end{aligned} \tag{4.23}$$

Therefore, the limit of the ratio of the iterative input to the desired input in Eq. (4.14) is simplified as:

$$\begin{aligned}\frac{u_\infty(j\omega)}{u_d(j\omega)} \triangleq \lim_{k\to\infty}\frac{u_k(j\omega)}{u_d(j\omega)} &= \lim_{k\to\infty}\frac{G(j\omega)}{G(j\omega)\,(1+S_k(j\omega))+P_k(j\omega)/\alpha} \\ &= \lim_{k\to\infty}\frac{1}{1+S_k(j\omega)} \triangleq \frac{1}{1+S_\infty(j\omega)} \end{aligned} \tag{4.24}$$

Since the term $|S_\infty(j\omega)|$ is bounded as

$$\begin{aligned}|S_\infty(j\omega)| &= \lim_{k\to\infty}\left|\sum_{j=1}^{k-1}\prod_{i=1}^{j}\frac{y_{k-i,n}(j\omega)}{y_d(j\omega)}\right| \\ &\le \lim_{k\to\infty}\sum_{j=1}^{k-1}\left|\prod_{i=1}^{j}\frac{y_{k-i,n}(j\omega)}{y_d(j\omega)}\right| \\ &\le \sum_{k=1}^{\infty}\varepsilon^k(\omega) \\ &= \frac{\varepsilon(\omega)}{1-\varepsilon(\omega)} < 1 \quad (\text{ for } \quad 0<\varepsilon(\omega)<1/2), \end{aligned} \tag{4.25}$$

Equation (4.18) follows directly by substituting Eq. (4.25) back into Eq. (4.24) and applying the triangle inequality:

$$\begin{aligned}\left|\frac{u_\infty(j\omega)}{u_d(j\omega)}\right| &\ge \frac{1}{1+|S_\infty(j\omega)|} \\ &\ge \frac{1}{1+\frac{\varepsilon(\omega)}{1-\varepsilon(\omega)}} \\ &= 1-\varepsilon(\omega), \end{aligned}$$

and

$$\begin{aligned}\left|\frac{u_\infty(j\omega)}{u_d(j\omega)}\right| &\le \frac{1}{1-|S_\infty(j\omega)|} \quad (\text{as} \quad |S_\infty(jw)|<1) \\ &\le \frac{1}{1-\frac{\varepsilon(\omega)}{1-\varepsilon(\omega)}} \\ &= \frac{1-\varepsilon(\omega)}{1-2\varepsilon(\omega)} < \infty \qquad (\text{as} \quad \varepsilon(\omega)<1/2) \end{aligned} \tag{4.26}$$

To quantify the phase variation of the iterative control input relative to the desired control input (Eq. (4.19)), we note that by using Eq. (4.24) and writing $S_\infty(j\omega)$ as $S_\infty(j\omega)=|S_\infty(j\omega)|e^{j\angle S_\infty(j\omega)}$

$$\frac{u_\infty(j\omega)}{u_d(j\omega)} = \frac{1}{1+|S_\infty(j\omega)|e^{j\theta(\hat{j}\omega)}} = \frac{1+|S_\infty(j\omega)|\cos\angle S_\infty(j\omega)-|S_\infty(j\omega)|\sin\angle S_\infty(j\omega)j}{\sqrt{(1+|S_\infty(j\omega)|\cos\angle S_\infty(j\omega))^2+(|S_\infty(j\omega)|\sin\angle S_\infty(j\omega))^2}} \tag{4.27}$$

Thus, the bound of the phase error $\angle\frac{u_\infty(j\omega)}{u_d(j\omega)}$ can be obtained by examining the sine of the phase variation and its derivative (with respect to $\angle S_\infty$) as below

$$\sin\left(\angle\frac{u_\infty(j\omega)}{u_d(j\omega)}\right) = \frac{-|S_\infty|\sin\angle S_\infty}{\sqrt{(1+|S_\infty|\cos\angle S_\infty)^2+(|S_\infty|\sin\angle S_\infty)^2}} \tag{4.28}$$

$$\frac{d\left[\sin\left(\angle\frac{u_\infty(j\omega)}{u_d(j\omega)}\right)\right]}{d\angle S_\infty} = \frac{-|S_\infty|\left(\cos\angle S_\infty+|S_\infty|\right)\left(1+|S_\infty|\cos\angle S_\infty\right)}{\left(1+2|S_\infty|\cos\angle S_\infty+|S_\infty|^2\right)} \tag{4.29}$$

Since $|S_\infty(j\omega)|<1$ (Eq. (4.25)), the above Eqs. (4.28, 4.29) imply that the bound of the phase error $\angle\frac{u_\infty(j\omega)}{u_d(j\omega)}$ is obtained when

$$\cos\angle S_\infty = -|S_\infty| \tag{4.30}$$

Thus Eq. (4.19) follows directly by combining the above Eqs. (4.28, 4.30) with Eq. (4.25). Moreover, we note that the limit of the relative tracking error yields

$$\begin{aligned}
\lim_{k\to\infty}\left|\frac{y_k(j\omega)-y_d(j\omega)}{y_d(j\omega)}\right| &= \lim_{k\to\infty}\left|\frac{y_{k,l}(j\omega)+y_{k,n}(j\omega)-y_d(j\omega)}{y_d(j\omega)}\right| \\
&\le \lim_{k\to\infty}\left|\frac{G(j\omega)}{G(j\omega)}\right|\left|\frac{u_k(j\omega)-u_d(j\omega)}{u_d(j\omega)}\right|+\left|\frac{y_{k,n}(j\omega)}{y_d(j\omega)}\right| \\
&\le \lim_{k\to\infty}\left|\frac{u_k(j\omega)}{u_d(j\omega)}-1\right|+\varepsilon(\omega) \\
&= \left|\frac{S_\infty(j\omega)}{1+S_\infty(j\omega)}\right|+\varepsilon(\omega). \quad \text{(by Eq. (4.24))}
\end{aligned} \tag{4.31}$$

Thus Eq. (4.20) follows directly by substituting Eq. (4.25) into the above question,

$$\begin{aligned}
\left|\frac{S_\infty(j\omega)}{1+S_\infty(j\omega)}\right|+\varepsilon(\omega) &\le \frac{|S_\infty(j\omega)|}{1-|S_\infty(j\omega)|}+\varepsilon(\omega) \quad (\text{as} \quad |S_\infty(j\omega)|<1) \\
&\le \frac{\frac{\varepsilon(\omega)}{1-\varepsilon(\omega)}}{1-\frac{\varepsilon(\omega)}{1-\varepsilon(\omega)}}+\varepsilon(\omega) \\
&= \frac{2\varepsilon(\omega)(1-\varepsilon(\omega))}{1-2\varepsilon(\omega)}<\infty \qquad (\text{as} \quad \varepsilon(\omega)<1/2)
\end{aligned} \tag{4.32}$$

This completes the proof of Result 1). To show Result 2, we note that Eqs. (4.21, 4.31) imply that the bound

$$\frac{2\varepsilon(\omega)(1-\varepsilon(\omega))}{1-2\varepsilon(\omega)}<1$$

will guarantee that the use of the MIIC law at frequency ω will improve the output tracking. Note the above Eq. is equivalent to

$$2\varepsilon^2(\omega) - 4\varepsilon(\omega) + 1 > 0 \tag{4.33}$$

Thus the bound of the NSR (4.22) follows by solving the above (4.33) for ε along with Eq. (4.17). This completes the proof. ■

Remark 7 Geometry interpretation of Theorem 3 *First note that geometrically, Equation (4.24) implies that the vector of the input ratio, $u_\infty(j\omega)/u_d(j\omega)$, falls into the neighborhood of point $(1,\ 0)$ with a radius of $S_\infty(j\omega)$, as shown by the grey area in Fig. 4.1 (a). Thus, it is evident from Fig. 4.1 (a) that the (lower and upper) magnitude bounds of the input ratio ($R_{\min}$ and $R_{\max}$ in Eq. (4.18)) are attained when the two vectors, $\vec{1}$ and $\vec{S_\infty}(j\omega)$, are aligned with each other while the size of $\vec{S_\infty}(j\omega)$ reaches its upper bound (Eq. (4.25)), as marked as points A and B in Fig. 4.1 (a), respectively. Moreover, the phase bound of the input ratio ($\theta_{\max}$ in Eq. (4.19)), as marked as θ in Fig. 4.1 (a), is attained when these two vectors are perpendicular to each other and the vector $\vec{S_\infty}(j\omega)$ is at its upper bound, which results in Eq. (4.19) directly. Secondly, a simple algebraic derivation combining Eqs. (4.24, 4.21) leads to the following condition to guarantee the tracking error is less than 1 under the MIIC law,*

$$\left|\vec{1} + \vec{S_\infty}(j\omega)\right| \geq \frac{1}{2-\varepsilon(\omega)},$$

This implies that the vector, $\vec{1} + \vec{S_\infty}(j\omega)$, must fall outside the circle centered at the origin with a radius of $1/(2-\varepsilon)$, which is equivalent to requiring that the size of the vector $\vec{S_\infty}(j\omega)$ must be below $1 - 1/(2-\varepsilon)$. Combining with Eq. (4.25), this amounts to (see Fig. 4.1 (b))

$$1 - \frac{1}{2-\varepsilon(\omega)} > \frac{\varepsilon(\omega)}{1-\varepsilon(\omega)},$$

which is equivalent to Eq. (4.33).

Remark 8 *Theorem 3 implies that precise tracking at frequency ω can be achieved provided that the NSR at that frequency is small, which agrees with our intuition. Additionally, Theorem 3 gives a guideline to determine the frequency range over which the MIIC law can be applied in practices*

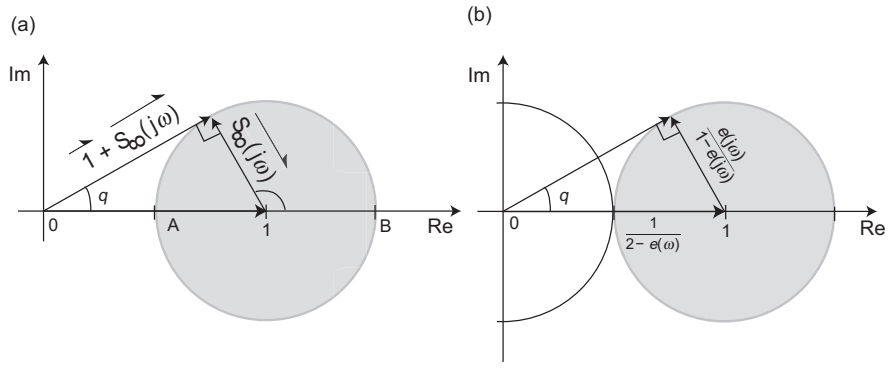

Figure 4.1 Geometric interpretation of Theorem 2.

(Eq. (4.22)). Note that the NSR at frequency ω can be experimentally estimated, for example, by comparing the power spectrum of the measurement noise or disturbance signal with that of the desired output trajectory.

4.3 Experimental Example: Piezotube Actuator Output Tracking

In this section, we illustrate the MIIC technique by implementing it to the output tracking of a piezotube actuator on an AFM system. First, a triangular trajectory was used as the desired trajectory, then secondly, band-limited white noise type of trajectories were used as the desired trajectories to further evaluate the performance of the MIIC algorithm. Finally, we also applied the MIIC algorithm for tracking of large-range trajectories when the hysteresis effect became pronounced. We start with describing the experimental system.

4.3.1 Experimental setup

The experimental system is schematically shown in Fig. 4.2 for the control of the x-axis piezotube actuator of an AFM system (Dimension 3100, Veeco Inc.). All the control inputs to the piezotube actuator were generated by using MATLAB-xPC-target package, and sent through a data acquisition card (DAQ) to drive the piezotube actuator via an amplifier—The AFM-controller had been customized so that the PID control circuit of the AFM-controller was bypassed when the external control input was

applied. The sampling rate was chosen at 50 KHz when tracking triangular trajectories, and reduced to 20 KHz when tracking the band-limited white noise type of trajectories due to the memory limit.

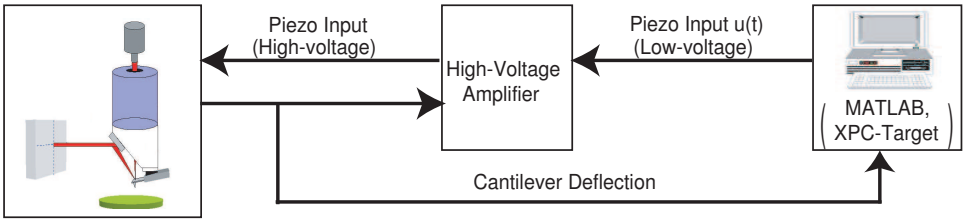

Figure 4.2 Schematic diagram of the experiment setup to implement the proposed MIIC algorithm.

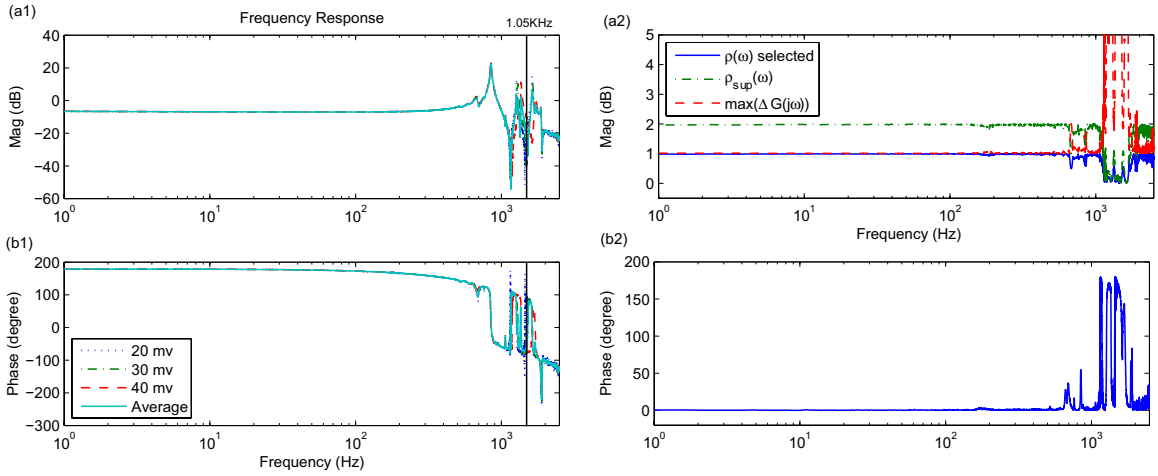

Figure 4.3 The experimentally frequency responses of the x-axis piezoelectric actuator on the AFM, measured with three different input amplitude levels (20 mv,30 mv, and 40 mv), with comparison to the averaged response.

4.3.2 Implementation and Tracking Results

Output Tracking of Triangle Trajectory To illustrate and evaluate the tracking performance of the proposed MIIC technique in compensating for the dynamics effects of LTI systems, the MIIC algorithm was implemented first to track a triangle trajectory. We note that triangle trajectories are commonly used in many scanning operations such as the AFM imaging. The displacement range was

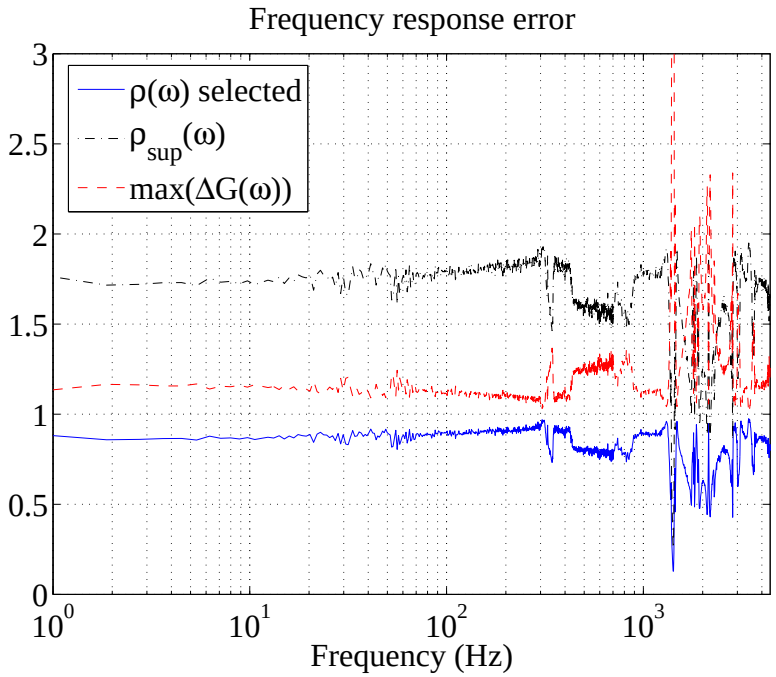

Figure 4.4 (top) The measured magnitude variation of the piezo actuator (see Eq. (4.6)), the upper bound of the iterative coefficient $\rho_{sup}(\omega)$, and the iterative coefficient $\rho(\omega)$ used in the experiments; and (bottom) the measured phase variation.

chosen small ($5\mu m, \sim 5\%$ of the total displacement range of the piezotube actuator), thereby the effect of the nonlinear hysteresis became small and negligible (as the hysteresis effect is range-dependent) (S. Tien. et al. (2005)). Three different rates (2 Hz, 100 Hz and 300 Hz) of the triangle trajectory were chosen—which correspond to the tracking in the low, medium and high speed ranges (relative to the bandwidth of the piezotube actuator), respectively. The tracking results are shown in Fig. 4.5, with comparison to those obtained by using the IIC technique. To implement the IIC control law, we first estimated the dynamics uncertainty of the piezotube actuator by measuring the frequency responses with three different input levels (20 mv, 30 mv, and 40 mv) with a dynamic signal analyzer (DSA, Hewlett Packard 356653A), as shown in Fig. 4.3. Then the iterative coefficient $\rho(\omega)$ was determined according to Eq. (4.3). Moreover, the experimental tracking results are also compared quantitatively in Table. 4.1 in terms of the relative maximum error $E_{max}(\%)$ and the relative root mean square (RMS) error $E_{rms}(\%)$, where

$$E_{max}(\%) \triangleq \frac{\|y_d(\cdot) - y(\cdot)\|_\infty}{\|y_d(\cdot)\|_\infty} \times 100, \qquad E_{rms}(\%) \triangleq \frac{\|y_d(\cdot) - y(\cdot)\|_2}{\|y_d(\cdot)\|_2} \times 100. \tag{4.34}$$

In the experiments, the iterations of the MIIC law (or the IIC law) were ceased when neither one of the above two errors, $E_{max}(\%)$ nor $E_{rms}(\%)$, can be further reduced. The iterative input for tracking multiple (over 10) periods of the triangle trajectory was sent to the system, and the averaged results are shown in Table. 4.1 and Fig. 4.5 (The un-averaged results are compared with the averaged ones later in Fig. 4.6). Also, the numbers of iterations used in the experiments are listed in Table 4.1.

Output Tracking of a Band-limited White-Noise Type of Trajectory We note that the triangle trajectory only consists of a few significant frequency components (i.e., multiple integer times of the fundamental frequency of the triangle signal), whereas a band-limited white-noise type of trajectory has much richer frequency components—up to the cut-off frequency. Therefore, it is more challenging to track band-limited white noise type of trajectories than to track the triangle trajectories. Specifically, the band-limited white-noise of one second duration were generated by using MATLAB, and then duplicated for multiple copies to form the desired trajectory. Three different cut-off frequencies, 400 Hz, 800 Hz, and 1050 Hz, where chosen in the experiments, and the displacement range of the desired trajectory was chosen around 1.5 μm. For comparison, the IIC algorithm was also implemented to track the three chosen white-noise type of trajectories. The obtained output tracking results are compared in Figs. 4.7, 4.8, and 4.9, and Table 4.2.

Output Tracking of Large-range Triangle Trajectory The proposed MIIC technique was also applied to track large-range triangle trajectories to evaluate its efficacy in compensating for the nonlinear hysteresis effect. To demonstrate the tracking error caused by the hysteresis and vibration dynamics effects, the DC gain method was applied in the experiments, where the input was obtained by simply scaling the desired output with the DC gain of the system, i.e., the DC-Gain method does not compensate for the hysteresis and the vibrational dynamics effects. It is noted that the hysteresis effect of piezotube actuators is significant as the displacement range becomes large (Y. Wu. et al. (2007)). The triangle trajectories with the displacement range of $50\mu m$ was chosen. Such a displacement range is

over 60% of the full displacement range of the piezotube actuator, and the hysteresis effect became pronounced in the output tracking. The tracking results are shown in Fig. 4.10 and Table. 4.3 for the same three triangle rates (2 Hz, 100 Hz and 300 Hz) as in small-range tracking.

4.3.3 Discussion of the Experiment Results

Triangle trajectory tracking The tracking results in Table. 4.1 show that by using the proposed MIIC algorithm, precise output tracking can be achieved. For the triangle trajectories at 2 Hz and 100 Hz, the tracking errors obtained by using the MIIC algorithm are similar to the error when using the IIC method (see Fig. 4.5). However, only two iterations were needed for the MIIC law to reach convergence, compared to 3 to 4 iterations needed for the IIC law. As the triangle rate increased to 300 Hz, the tracking error obtained by using the MIIC algorithm was 7 times smaller than the error by using the IIC algorithm (see Table 4.1). Note the frequency range to implement the MIIC algorithm (or the IIC algorithm) is a design parameter. The frequency range was chosen as 2.5 KHz and 1 KHz for the MIIC algorithm and the IIC algorithm, respectively, to optimize the tracking results. Particularly, we notice that divergence occurred for the IIC algorithm if the frequency range was chosen larger than 1.4 KHz. This can be explained by using the frequency response shown in Fig. 4.4: large phase variation exists for frequencies lager than 1 KHz, which becomes larger than $\pi/2$ around the second resonant peak at 1.3 KHz. Therefore, by Lemma 2, the output tracking will diverge at those frequencies. On the contrary, the proposed MIIC algorithm is not limited by such phase uncertainties, thereby the tracking performance can be further improved (see Fig. 4.5 (a3), (b3)). Moreover, we compared the power spectrum (estimated by using MATLAB) of the tracking error with that of the desired trajectory. It was found that the maximum power spectrum value of the tracking error was less than 0.4% of that of the desired trajectory. Thus, the experimental results show the superior tracking performance of the MIIC algorithm over the IIC algorithm.

We further evaluated the tracking precision of the proposed MIIC algorithm by comparing the averaged tracking result as well as the un-averaged one (picked from the middle of the multiple periods output) with the measurement noise. As shown in Fig. 4.6, the size of the un-averaged tracking errors

Table 4.1 Performance comparison of the MIIC algorithm and the IIC algorithm for tracking the triangle trajectory at three different triangle rates, where $E_{rms}(\%)$ and $E_{max}(\%)$ are defined in Eq. (4.34), and the iteration numbers used are also listed. The displacement range is 5 μm.

Iter. No.	E_{rms} (%)					
	2 Hz		100 Hz		300 Hz	
	MIIC	IIC	MIIC	IIC	MIIC	IIC
1	0.6026	1.3529	0.7160	4.5145	2.0689	12.7279
2	0.2291	0.3033	0.3477	3.0220	1.7508	12.1486
3	0.2279	0.2338	0.3243	2.5296	1.7529	12.1497
4	0.2292	0.23256	0.3267	2.0518	1.7517	12.1394
Iter. No.	E_{max} (%)					
	2 Hz		100 Hz		300 Hz	
	MIIC	IIC	MIIC	IIC	MIIC	IIC
1	1.1106	1.5927	1.7450	4.7731	5.8387	17.7013
2	0.7296	0.9274	1.5784	4.9721	5.4809	19.7839
3	0.7890	0.9197	1.6046	5.3670	5.4594	19.3573
4	0.7677	0.6804	1.6598	2.6577	5.5369	19.4687

was close to the noise level for all the three chosen triangle rates (10 Hz, 100 Hz, and 300 Hz, compare Fig. 4.6 (b, c, d) with (a)), and at low speed (2 Hz), the tracking error was dramatically reduced via averaging—the 2-norm of the averaged tracking error was over 3 times smaller than that of the noise. Such a dramatic reduction via averaging can be utilized in applications to achieve a measurement precision beyond the noise limit, for example, in the measurement of material properties at nanoscale (H.-J. Butt. et al. (2005)). Even at higher speed tracking of 100 Hz, significant reduction of the tracking error was still achieved via averaging (see Fig. 4.6 (b1)). We note that the error reduction via averaging became small in higher speed tracking of 300 Hz, due to the effect of the system dynamics beyond the frequency range over which the MIIC algorithm was applied (at 2.5 KHz). Therefore, our experimental results show that high-speed output-tracking can be achieved by using the proposed MIIC algorithm.

Tracking of band-limited white-noise trajectories The band-limited white noise trajectory has much richer frequency components than triangle trajectories, which is evident as shown by the power spectrum of the three band-limited white noise trajectories in Fig. 4.9. Our experimental results (Ta-

ble. 4.2 and Figs. 4.7 and 4.8) demonstrate that by using the MIIC technique, precise output tracking can still be achieved for such complex trajectories. For band-limited white-noise trajectory with cut-off frequency of 400 Hz, the tracking errors obtained by using the MIIC technique were very small (the relative RMS error is less than 2 %). Such a tracking precision was maintained even when the cut-off frequency became much higher (800 Hz and 1.05 KHz). We note that in order to achieve the same tracking precision (RMS error $E_{rms} \leq 2$ %) by using feedback control approaches, the closed-loop sensitivity must be kept below -34 dB (i.e., 0.02) for frequency $\omega \leq 1.05\ KHz$, which, in turn, requires the closed-loop bandwidth to be much higher than the cut-off frequency of 1.05 KHz. Such a high bandwidth is extremely difficult to achieve with feedback control—if not entirely impossible, as the cut-off frequency of 1.05 KHz is significantly higher than the bandwidth of the piezotube actuator, encompassing two resonant peaks as well as one ”dip” (i.e., highly under-damped zero) of the piezotube actuator dynamics, as marked out in Fig. 4.3. Note that such a comparison is to highlight the efficacy of the proposed MIIC algorithm in tracking broad-band trajectories in repetitive operations, in light of the Result of Ref. (M. Verwoerda. et al. (2006)) that an equivalent feedback controller exists for causal iterative learning algorithms.

The experimental results also show that the proposed MIIC technique is robust against system dynamics uncertainty, particularly the phase uncertainty. As we can see from Fig. 4.7, divergences occurred when the IIC method was used to track such complex broad-band trajectories. For the band-limited white-noise trajectory with cut-off frequency of 400 Hz, large tracking error occurred, which became much larger than the desired trajectory itself as the cut-off frequency increased to 800 Hz and 1.05 KHz. Such sensitivity of the iteration to the phase uncertainty is removed in the MIIC technique. Therefore, the experimental results show that the proposed MIIC algorithm is superior to the IIC method in tracking high-speed complex output trajectories.

Large-range triangle trajectory The tracking results in Table. 4.3 and Fig. 4.10 show that precise tracking at large displacement range can also be achieved by using the MIIC algorithm. As revealed by the output tracking obtained by using the DC-gain method, the hysteresis effect became pronounced at

Table 4.2 Tracking performance Comparison of the MIIC with the IIC algorithms to track a band-limited white noise trajectory with different cut-off frequencies are where "Iter. No." denotes the number of iterations used in experiments.

Iter. No.	E_{rms} (%)					
	400 Hz		800 Hz		1050 Hz	
	MIIC	IIC	MIIC	IIC	MIIC	IIC
1	2.6123	17.1439	4.5240	94.1437	4.93406	962.8028
2	1.5548	63.2610	1.3014	350.1737	1.2710	Diverge
3	1.5060	Diverge	1.3223	Diverge	1.1992	Diverge
4	1.7034	Diverge	1.3355	Diverge	1.1934	Diverge
Iter. No.	E_{max} (%)					
	400 Hz		800 Hz		1050 Hz	
	MIIC	IIC	MIIC	IIC	MIIC	IIC
1	3.3647	17.3808	5.7165	98.9275	6.7249	1003.9
2	1.9774	61.4206	4.5881	563.5381	3.1347	Diverge
3	2.0713	Diverge	4.9661	Diverge	3.3160	Diverge
4	2.3516	Diverge	4.9499	Diverge	3.1175	Diverge

large displacement range (50 μm, Fig. 4.10 (a)), which was augmented with the vibrational dynamics effect at high-speed (100 Hz and 300 Hz), resulting in larger tracking errors, see Fig. 4.10 (b), (c). The experimental results show that at slow-speed (2 Hz) tracking, the tracking error obtained by the MIIC algorithm was small (the relative RMS error and the relative maximum error are at 0.22 % and 0.37 %, respectively), and very close to that of tracking small-range triangle trajectory (Compare Table 4.1 with Table 4.2). Even at much higher speeds (100 Hz and 300 Hz), precise tracking was still maintained. For example, the relative RMS error was still only about 4.7 % for tracking the triangle trajectory of 300 Hz. We note that this error is slightly larger than the error in small-range tracking. This is mainly due to the reduction of the frequency range over which the MIIC algorithm was implemented (from 2.5 KHz to 2 KHz)—to prevent the input voltage from saturation. We also note that the dynamics variations caused by the hysteresis effect became pronounce in large-range tracking, thereby more iterations were needed in large-range tracking than in the small-range tracking (see Table 4.3). Therefore, the experimental results demonstrate that the MIIC algorithm can be used to compensate for both the hysteresis and the dynamics effects simultaneously.

Table 4.3 Tracking performance achieved by using the MIIC algorithm to track a large range triangular trajectory at different speeds. The number of iterations (Iter. No.) used is also listed.

Iter.	E_{rms} (%)			E_{max} (%)		
No.	2 Hz	100 Hz	300 Hz	2 Hz	100 Hz	300 Hz
1	16.2798	14.9187	16.7815	17.8695	14.48487	17.4982
2	5.8267	4.4482	6.4311	6.0470	4.8405	8.5115
3	2.0171	1.5763	4.8690	2.0396	4.0078	11.16333
4	0.6062	0.8372	4.7582	0.7377	1.5715	10.4311
5	0.2236	0.6078	4.7463	0.3760	2.4580	10.4798

4.4 Conclusions

This chapter introduced a model-less inversion-based iterative control for tracking of repetitive trajectories at high-speed. The convergence of the MIIC algorithm was analyzed for both the case when the noise/disturbance is negligible and the case when the effect of the disturbance/noise is considered. It was shown that the convergence can be achieved in one iteration when the noise effect is negligible. When the disturbance/noise effect is considered, the input error at a given frequency, as measured by the ratio of the iterative input to the desired input, was quantified in terms of the disturbance/noise to signal ratio (relative to the desired trajectory). It was shown that the convergence of the MIIC algorithm can be guaranteed when the NSR is smaller than one-half, and the MIIC algorithm can guarantee to improve the tracking if the NSR is less than $1-1/\sqrt{2}$. The proposed method was applied to the output tracking of a piezotube actuator on an AFM system. The experimental results demonstrated that the MIIC can achieve precise output tracking for both high-speed triangle trajectories and band-limited white-noise trajectories with cut-off frequency beyond the bandwidth of the piezotube actuator. Moreover, precise output tracking of large-range triangle trajectories at high-speed can also be achieved, indicating the ability of the proposed MIIC technique to compensate for both the hysteresis and the dynamic effects simultaneously.

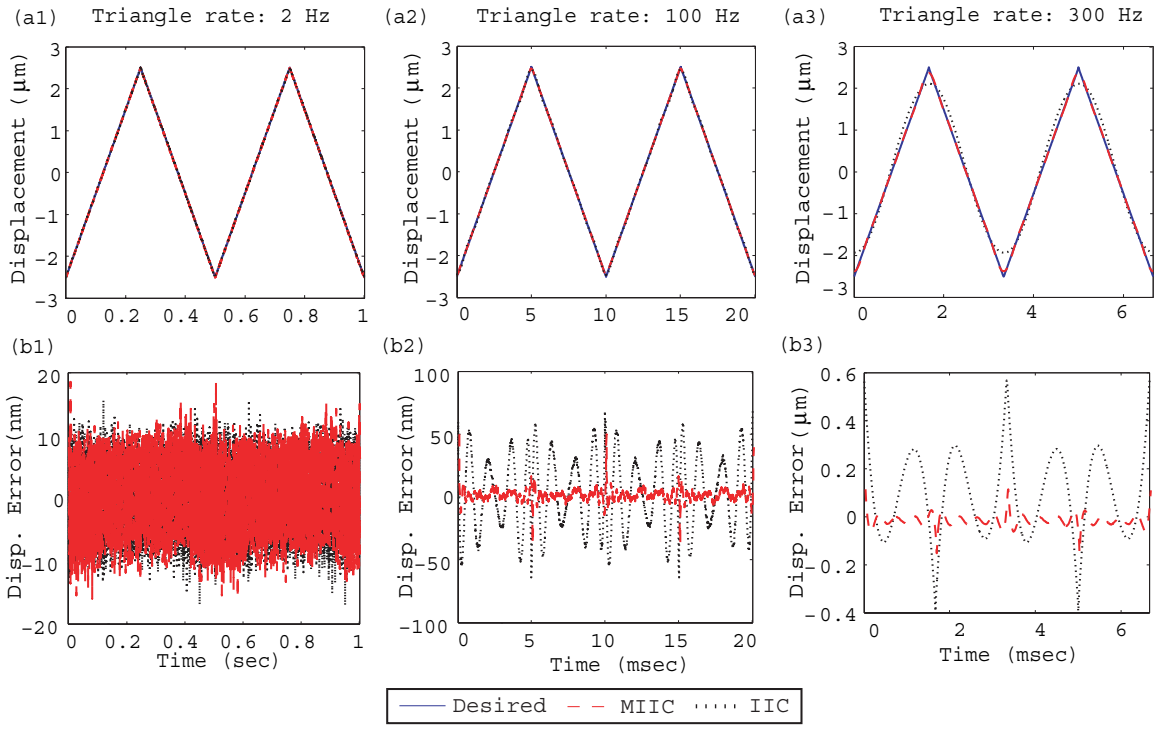

Figure 4.5 Experimental results: (top row) comparison of the output tracking obtained by using the MIIC algorithm with the tracking by the IIC algorithm for three different triangle rates; and (bottom row) comparison of the corresponding tracking errors.

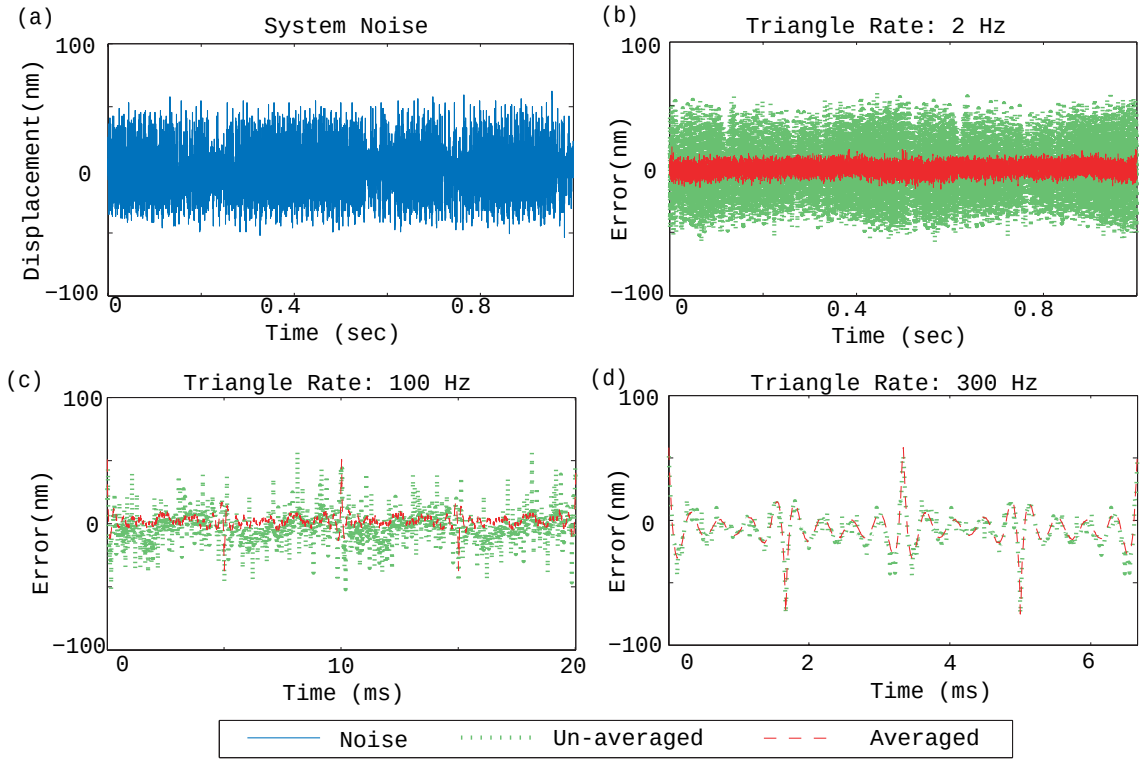

Figure 4.6 Comparison of (a) the measurement noise (a1) with the averaged tracking error and the un-averaged error of the triangle trajectory at rates of (b) 2 Hz, (c) 100 Hz, and (d) 300 Hz.

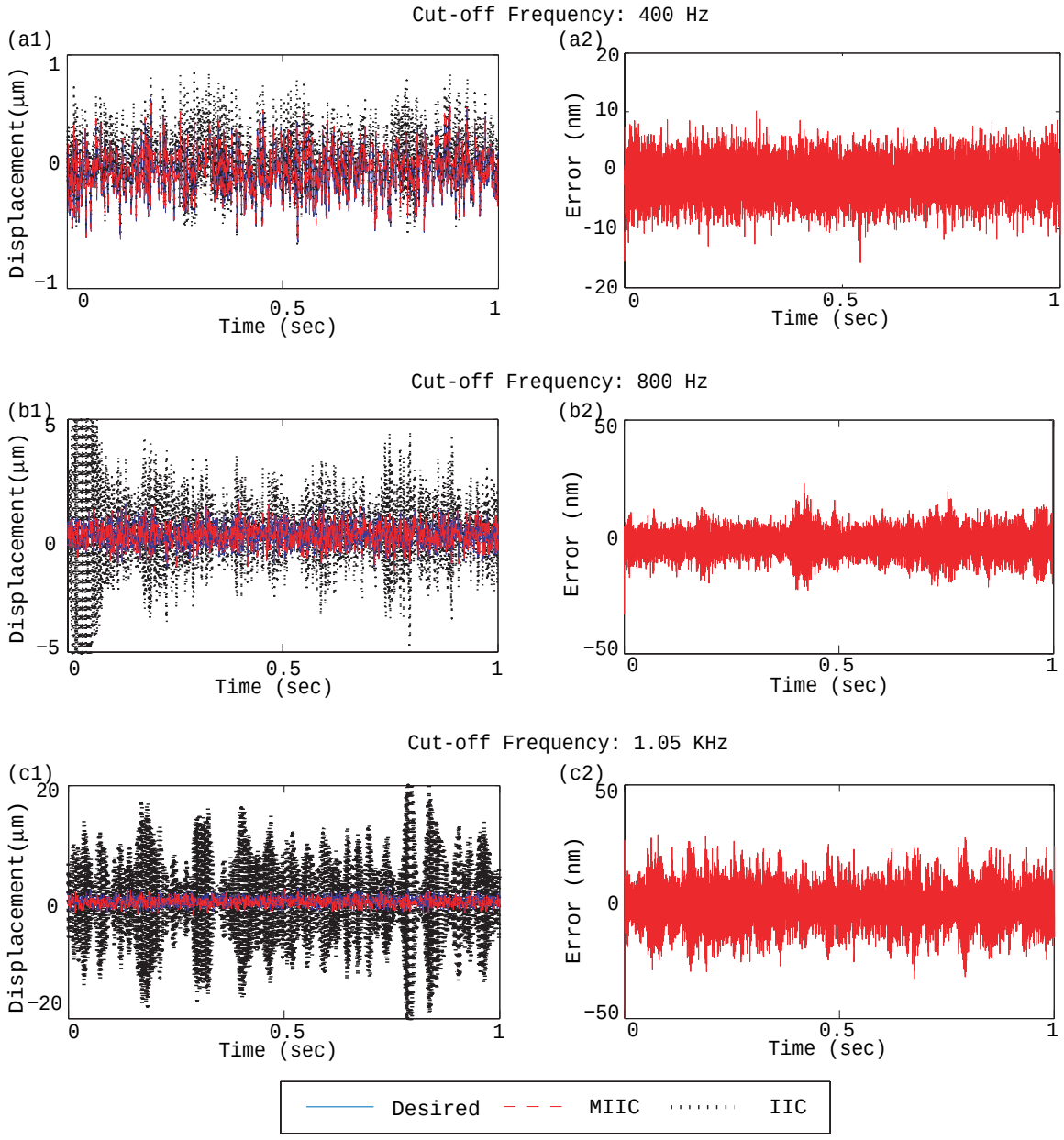

Figure 4.7 (left column) Comparison of the tracking results the band-limited white-noise trajectory at cut-off frequency of (a1) 400 Hz, (b1) 800 Hz, and (c1) 1.05 KHz by using the MIIC algorithm with those obtained by using the IIC algorithm, and (right column) the corresponding tracking errors by using the MIIC algorithm.

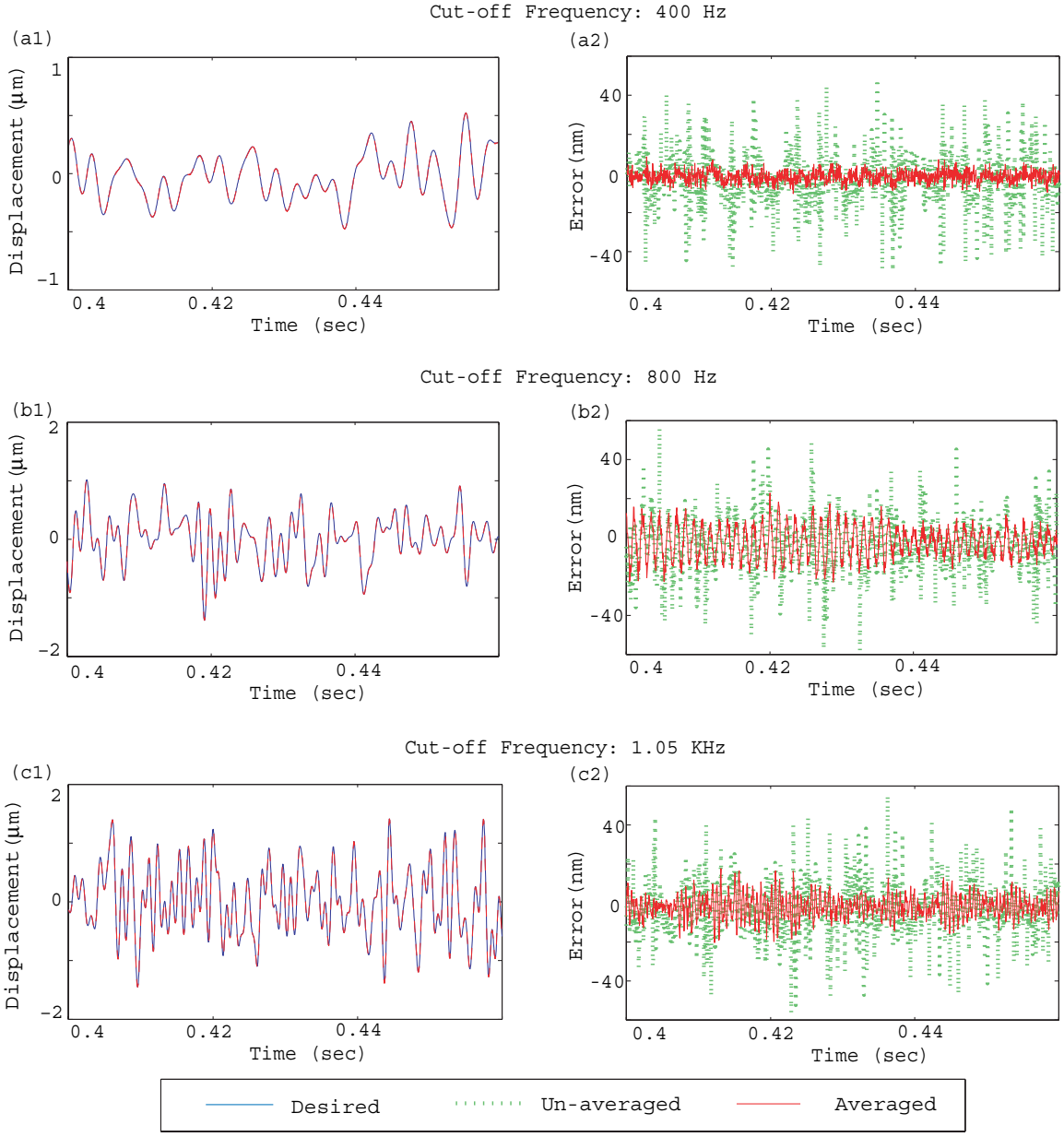

Figure 4.8 (left column) The zoomed-in view of the tracking of the band-limited white noise trajectory tracking results obtained by the MIIC algorithm for a time interval of 0.06 sec; and (right column) comparison of the corresponding the un-averaged with the averaged tracking errors.

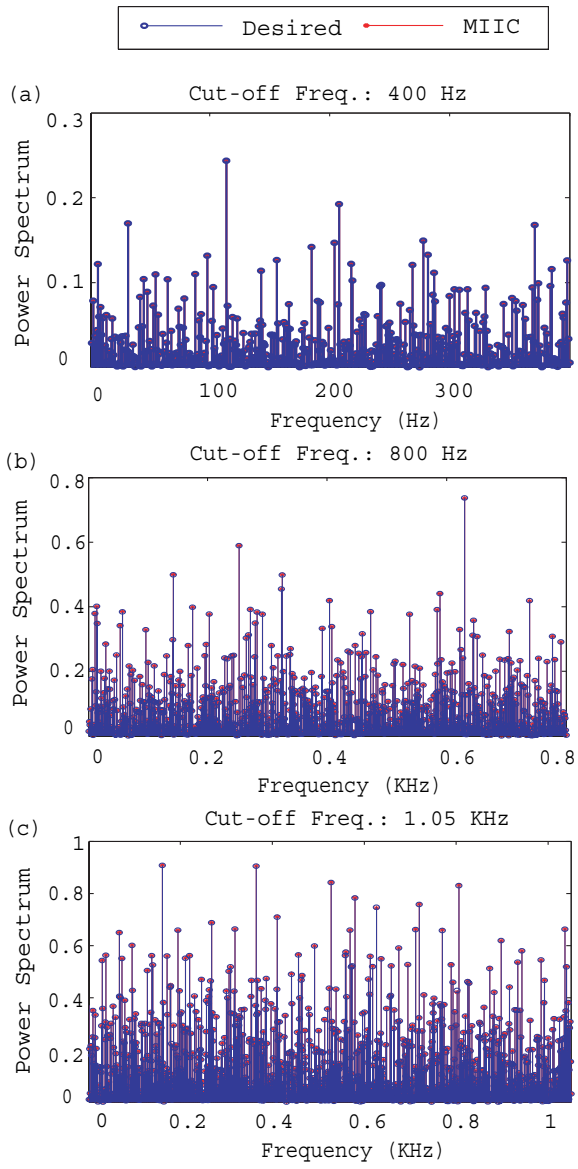

Figure 4.9 Comparison of the power spectrum of the band-limited white noise desired trajectory (blue circle) with the power spectrum of the output tracking obtained by using the MIIC algorithm (red cross).

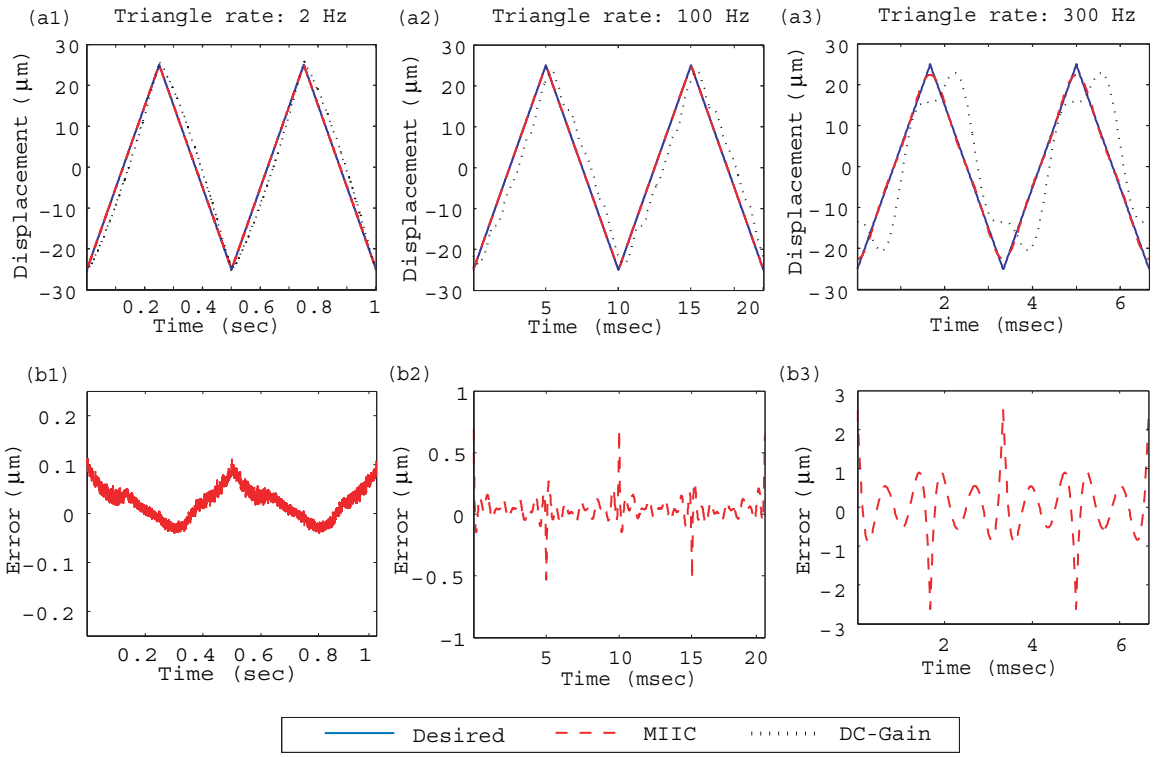

Figure 4.10 (top row) Comparison of the output tracking obtained by using the DC-Gain method with the tracking by the MIIC algorithm at the rates of (a1) 2 Hz, (a2) 100 Hz and (a3) 300 Hz, and (bottom row) the corresponding tracking errors obtained by using the MIIC algorithm.

CHAPTER 5. High speed force-volume mapping using atomic force microscope.

A paper A paper in proceedings of American Control Conference, 2009

Abstract

This chapter proposes a control approach based on the notion of superimposition and iterative learning control to achieve high-speed force-volume mapping on scanning probe microscope (SPM). Current force-volume mapping measurement is slow, resulting in large temporal errors in the force mapping when rapid dynamic evolution is involved in the sample. The force-volume mapping speed is limited by the challenge to overcome the hardware adverse effects excited during high-speed mapping, particularly over a relatively large sample area. The contribution of this article is the development of a novel control approach to high-speed force-volume mapping. The proposed approach utilizes the concept of signal decoupling-superimposition and the recently-developed model-less inversion-based iterative control (MIIC) technique. Experiment on force-curve mapping of a Polydimethylsiloxane (PDMS) sample is presented to illustrate the proposed approach. The experimental results show that the mapping speed can be increased by over 20 times.

5.1 Introduction

In this chapter, an approach based on iterative control to achieve high-speed force-volume mapping on atomic force microscopy (AFM) is proposed. Force-volume mapping, which is to acquire a mapping of local material properties at nanoscale over a sample area, has become an important tool in sciences and engineering fields including biology and materials science (Jeffrey L. Hutter. et al. (2004, 2000); H. Suzuki. et al. (1998)). Current force-volume mapping with measurement time generally

over 30 minutes, however, is slow (H. Suzuki. et al. (1998)) and induces large temporal errors into the mapping when the material property to be measured changes rapidly during the mapping. For example, in the elasticity of collagen sample changes rapidly during the dehydration process (Marshall GW . et al. (1998)). The force-volume mapping speed is limited by the challenge to overcome the hardware adverse effects that can be excited during high-speed mapping over a relatively large sample area. The contribution of this chapter is to propose a high-speed force-volume mapping approach based on signal decoupling-superimposition along with the model-less inversion-based iterative control (MIIC) technique. The proposed method is illustrated by implementing it to obtain the force-curve mapping of a Polydimethylsiloxane (PDMS) sample on one scan line. The experimental results are presented to show that the mapping speed can be increased by over 20 times.

Various force-volume mapping techniques have been developed (M. Radmacher. et al. (1994); David R. Baselta. et al. (1994); Koleske, D. D. et al. (1995); B Cappella. et al. (1997)). However, current force-volume mapping methods can not achieve the desired high-speed force-volume mapping. For example, the absolute mode (M. Radmacher. et al. (1994)), where the force-curve at each sample point was measured from the same initial position with the same (vertical) distance, undesirable excessively large load force can be generated at some points and/or not touching the sample at others. Such issues are avoided in the relative mode (David R. Baselta. et al. (1994)), where the same initial load force is applied to the probe before measuring the force-curve at each sample point, as well as when transiting the probe laterally between sample points. However, the sliding of the probe on the sample in this mode is not desirable for soft samples. To avoid such a sliding on the sample, the touch and lift mode (B Cappella. et al. (1997)) has been proposed, where feedback control has been used to determine the load force profile during the force-curve measurement and to lift the probe off the sample afterwards. However, the touch and lift mode is slow in order to compensate for the unknown sample topography variations. In all these above modes, the measurement speed is further limited because during the mapping, the cantilever only moves (relative to the sample) either horizontally (during the transition to the next sample point) or vertically (during the force-curve measurement), but not simultaneously. This horizontal-vertical alternation is avoided by measuring the force curves while

continuously scanning the sample in the lateral direction (H. Suzuki. et al. (1998)). Although in this method the probe is lift up after each force curve while the probe is transited to the next sample point, the lateral scanning speed has to be slow (0.1 Hz in (H. Suzuki. et al. (1998))) to avoid lateral sliding during the force curve. Clearly, there exist a need to develop new paradigm for achieving high-speed force-volume mapping.

Achieving high-speed force-volume mapping is challenging. The challenge is three-fold: (1) high-speed force-curve measurement at each sample point, (2) rapid transition of the probe from one sample point to the next while compensating for the sample topography difference between the two points, with no sliding of the probe on the sample, and (3) seamless integration of the above two motions. These challenges are caused by the adverse effects that can be excited during high-speed force-volume mapping, including the vibrational dynamics of the piezo actuators (used to position the probe relative to the sample) along with the cantilever (K. Kim. et al. (2008); D. Abramovitch. et al. (2007); S. Tien. et al. (2005)), the nonlinear hysteresis effect of the piezo actuators (Y. Wu. et al. (2007); K. K. Leang. et al. (2006)), and the system uncertainties (Srinivasa M. Salapaka. et al. (2005); Ying Wu. et al. (2007); Georg E. Fantner. et al. (2005)). The vibrational dynamics and the nonlinear hysteresis effects limit the speed of the force-curve measurement (at one sample point) , particularly when the vertical displacement of the force-curve is large (in order to lift up the sample and in case the required load force is large). Additionally, during the transition of the probe to compensate for the sample topography variation, post transition oscillations can occur (Mark A. Lau. et al. (2003)), particularly at high-speed. Moreover, the motion of the probe (in the vertical direction) needs to switch back and forth between force-curve measurement (at one sample point) and output transition (between current sample point and the next one). Such a switching at high-speed, can also result in large transient oscillatory response due to the mismatch of the state condition at the end of the force-curve measurement and the desired initial state for the point-to-point transition (A. Serrani. et al. (2001)). Therefore, there exist a need to develop new control approach to achieve high-speed force-volume mapping.

The main contribution of the chapter is the development of a novel switching-motion based force-

volume mapping mode. The proposed mode consists of stop-and-go switching motion in lateral scanning, synchronized with the vertical probe motion switching between force-curve measurement and point-to-point output transition. To achieve precision tracking in the lateral scanning as well as in the vertical switching motion, we propose to combine the utilization of the notion of superimposition with the recently-developed MIIC technique . First, the vertical motion of the probe is decoupled as the summation of elements of force-curve measurement at one sample point and elements of output transition at one sample point. Then secondly, the MIIC technique is implemented to obtain the control input to track the element force-curve, and to achieve the element output-transition (at one point) as well. Finally, the control is achieved by superimposing these element inputs together appropriately. The a priori sample topography knowledge is utilized in the proposed mode, which can be obtained by using high-speed AFM imaging technique (Paul K. Hansma. et al. (2006); Ying Wu. et al. (2008)). The proposed method is illustrated by implementing it in experiments to obtain force-volume mapping of a Polydimethylsiloxane (PDMS) sample. The experimental results show that the speed of force-volume mapping can be achieved over 20 times with large lateral scan range (40 μm) and high spatial resolution (128 number of force curves measured per scan line).

5.2 Iterative control approach to high speed force mapping

We start with describing force-volume mapping method and the related control requirements for high-speed mapping. Then we will introduce the proposed force-volume scheme based on switching-motion. The proposed force-volume scheme is achieved by utilizing the recently developed model-less inversion based iterative control technique .

5.2.1 Precision control requirements in force-volume mapping

Force volume mapping extends the force-curve measurement at one sample point to obtain a mapping of the force-curves across a sample area (Hans-Jurgen Butta. et al. (2008); M. Radmacher. et al. (1994)). To measure the force curve using AFM, the cantilever is driven by a piezoelectric actuator to approach and touch the sample surface until the cantilever deflection (i.e., the probe-sample interaction force) reaches the set-point value (see Fig. 5.1). Then the piezoelectric actuator retraces to withdraw

the cantilever from the sample surface until the probe surface contact is broken. To obtain a mapping of force-curves over a sample area (see Fig. 5.1)—the so called *force-volume mapping*, the force curve is measured at each sample point while the sample is scanned continuously at low-speed under a raster pattern (Note as discussed in the introduction, other methods have been proposed previously, but this method is currently employed by the industry). (Hans-Jurgen Butta. et al. (2008)). Feedback control is applied during the force-curve measurement to maintain the same force load and guide the point-to-point probe relocation. The feedback control is to compensate for the sample topography variation from one sample point to the next, thereby the difference of the measured force-curves at different sample points will only represent the difference of the material properties—not effected by the sample topography difference. Therefore, precision positioning is important in force-volume mapping, because the positioning error during the force-curve measurement at each sample point is directly translated to the errors in the force and/or indentation measurements, and the positioning error in the lateral scanning and in the transition will lead to the coupling of the sample topography into the force measurements, which leads to the positioning errors in the force-curve measurement at each sample point as well.

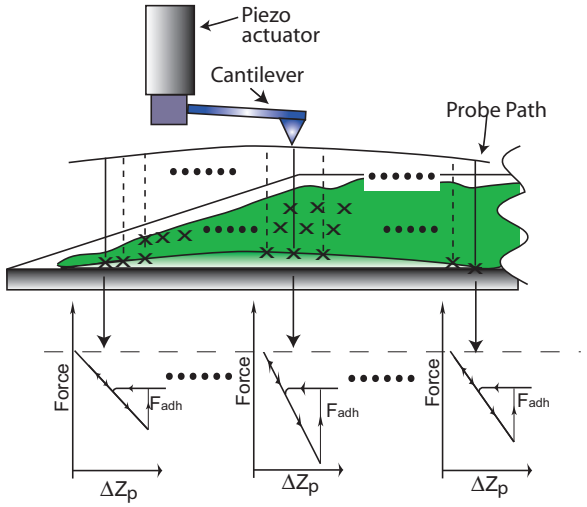

Figure 5.1 Concept of force mapping

5.2.2 Switching-motion based force-volume mapping

In this chapter, we propose a switching-motion based force-volume mapping scheme: First, we assume that the sample topography profile has been obtained a priori before the force-volume map-

ping (for example, through imaging the sample (Georg E. Fantner. et al. (2005); Ying Wu. et al. (2008)). Then the obtained sample profile will be used to achieve high-speed force-volume mapping. In the proposed force-volume mapping, the lateral *x*-axis scanning trajectory consists of stop-sections and go-sections alternative with each other (see Fig. 5.2 (a)). Such a stop-and-go switching in lateral scanning will be synchronized with the vertical probe motion as follows: During the stop section (t_m in Fig. 5.2 (a)), the force-curve will be measured at each sample point, and the probe will be positioned above the sample at the end of the force-curve measurement; then during the subsequent go (transition) section (t_t in Fig. 5.2 (a)), the AFM-probe will be transited from one sample point to the next, and the sample topography difference between these two sample points will be compensated for. In this method, since the force-curves are acquired with no lateral motion of the probe (relative to the sample), the lateral spatial resolution is improved, particularly at high-speed, over existing force-volume mapping methods (M. Radmacher. et al. (1994); Koleske, D. D. et al. (1995)) with lateral scanning during the force-curve measurement. Moreover, since the sample topography variation is compensated for (through the probe relocation), feedback control is not needed to maintain the same load force profile during the force-curve measurement. Rather, the same input for force-curve measurement can be applied at each sample point. The use of the same input for force-curve at all sample points implies that iterative learning control techniques can be applied to achieve high-speed in force-curve measurements, as demonstrated in our recent work .

Next, we describe the design of the output trajectory in both the *x*-axis and the *z*-axis.

5.2.2.1 Switching-motion based trajectory in lateral *x*-axis scanning

In the proposed approach, the desired stair-like trajectory in the lateral *x*-axis can be specified as follows: For given lateral scan rate f (in Hz), lateral spatial resolution R (i.e., number of force curves per one scan line), duty ratio $D(\%)$ (i.e., the ratio of the stop-section duration (t_m) relative to the total go and stop duration ($t_m + t_t$), $D = 100 * t_m/(t_m + t_t)$, see Fig. 5.2 (a)), and the total lateral scan length L, the duration time of the go (transition)-section t_t and that of the stop (measurement)-section t_m, and the

lateral spatial distance between two adjacent sample points ℓ_s are determined as below, respectively,

$$t_t = \frac{100 - D}{200 \cdot R \cdot f}, \qquad t_m = \frac{D}{200 \cdot R \cdot f}, \qquad l_s = \frac{L}{\cdot R}. \tag{5.1}$$

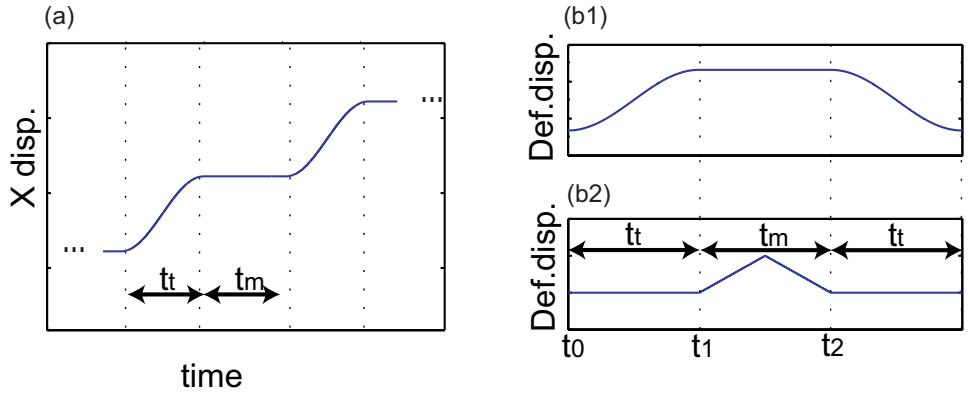

Figure 5.2 Basic element of the desired trajectories. (a) X-directional displacement desired trajectory composed of stop (force-curve measurement section) and go (transition section). (b1) Desired deflection the transition trajectory, $z_t(t)$, for point-to-point sample topography variation compensation. (b2) Desired deflection trajectory, $z_m(t)$, for force curve measurement.

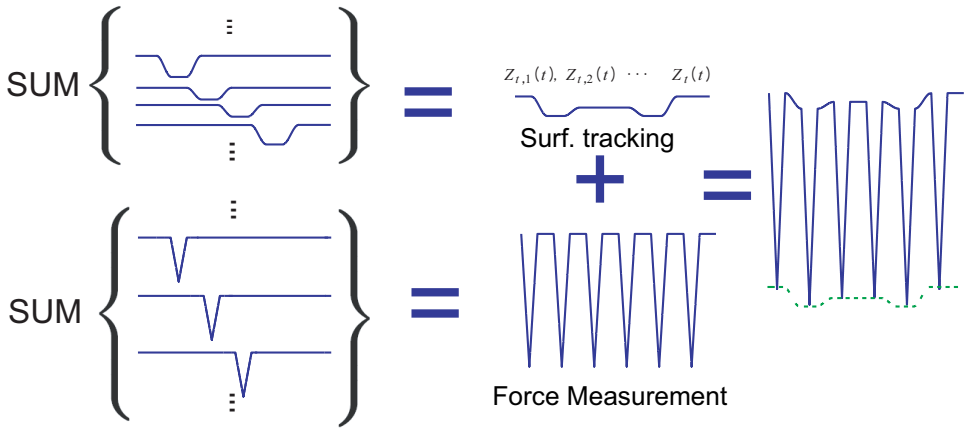

Figure 5.3 Desired deflection signal trajectory generation using linear superimposition.

5.2.2.2 Vertical *z*-axis trajectory for force-curve measurements and sample topography compensation

In this chapter, we propose a feedforward control approach that combines offline iterative learning with online implementation via superimposition for the switch-motion based *z*-axis tracking. First, we

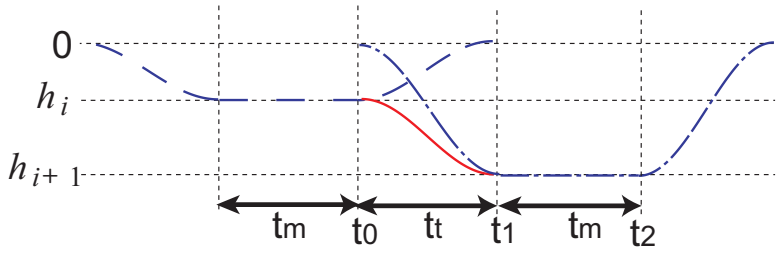

Figure 5.4 Surface tracking trajectory superimposition. One element of the surface topography tracking signal (dashed line) superimposed on the other element of the surface topography tracking signal (dashed dotted line) generates point to point transition trajectory (solid line).

decouple the desired z-axis trajectory $z_d(t)$ across the entire scan line, into the trajectory for measuring the probe transition that compensates for the point-to-point sample topography variation, $z_t(t)$, and the trajectory for the force-curves at each sample point, $z_m(t)$, i.e.,

$$z_d(t) = z_t(t) + z_m(t) \tag{5.2}$$

Then we will find the feedforward input to track the transition trajectory $z_t(t)$, $u_t(t)$, and the feedforward input to track the force-curves trajectory $z_m(t)$, $u_m(t)$, respectively, through an offline iterative learning method (see Sec. 5.2.3). Provided that the SPM dynamics can be adequately approximated by a linear system around each sample point location, the total input to track the z-axis trajectory $z_d(t)$, $u_z(t)$, can be obtained as

$$u_z(t) = u_t(t) + u_m(t). \tag{5.3}$$

The linearization condition holds in the proposed force-volume mapping approach provided that enough points are sampled along the scan line—as needed to achieve high resolution in the force-volume mapping. This is because that with enough sampled points, the displacement range of the point-to-point probe relocation at each sample point is small. As a result, the nonlinear hysteresis effect becomes small and negligible. We note that although the vertical displacement range in each force-curve might be large and the hysteresis effect can be substantial, the hysteresis effect will be effectively addressed through offline iterations in the proposed approach. Based on the above trajectory decoupling (Eq. (5.2)), we further decouple the desired transition trajectory $z_t(t)$ as a summation of one-point transition $z_{t,i}(t)$ with

different transition range (see Fig. 5.3 and 5.4) :

$$z_t(t) = \sum_{i=1}^{R} h_i z_{t,i}(t - i * T_s), \quad (T_s \triangleq t_t + t_m) \tag{5.4}$$

where R is the lateral spatial resolution defined before, h_i denotes the scale factor for the one-point transition, and $z_{t,i}(t)$ denotes the transition trajectory element selected from a library for the transition at the i^{th} sample point, i.e., the library consists of trajectory elements for one-point transition with different transition ranges, which will be constructed offline a priori. Thus, in implementations, the entire sample topography trajectory across each scan line will be obtained a priori and then partitioned by the total number of sample points to determine the selection of the one-point transition element $z_{t,i}(\cdot)$. Additionally, the one-point transition element $z_{t,i}(\cdot)$ comprises an up-transition section and a down-transition, connected by a stop (flat) section in between (see Fig. 5.4)—during the flat section, force curve will be measured. The inclusion of both up- and down- transition sections renders the same initial and post state condition, which facilitates the use of iterative control to track such a trajectory. To enable the point-to-point transitions along the scan line, the down-section of the current one-point transition will be superimposed with the up-section of the next one-point transition, as schematically shown in Fig. 5.4. Particularly, the up- and down- transition sections are designed by using cosine functions, such that the superimposed trajectory becomes a cosine function plus an offset, i.e.,.

$$\begin{aligned} & \frac{h_i}{2}\left[cos\left(\omega\left(t-t_0\right)\right)+1\right]+\frac{h_{i+1}}{2}\left[cos\left(\omega\left(t-t_0\right)+\pi\right)+1\right] \\ = \quad & \frac{h_i-h_{i+1}}{2}cos\left(\omega\left(t-t_0\right)\right)+\frac{h_i+h_{i+1}}{2} \end{aligned} \tag{5.5}$$

where h_i and h_{i+1} denotes the partitioned transition height at the i^{th} and the $i+1^{th}$ sample point, respectively. Thus, such a construction will ensure that the superimposition can be proceeded across the sample points such that the smoothness at the transition points is maintained.

Similarly, the force-curve measurement trajectory $z_m(t)$ is also decoupled as a summation of individual force-curves at each sample point as follows (see Fig. 5.2):

$$z_m(t) = \sum_{i=1}^{R} z_{m,i}(t - i * T_s), \quad (T_s \triangleq t_t + t_m) \tag{5.6}$$

where $z_{m,i}(t)$ denotes force curve measurement at the i^{th} sample point. Note that in the proposed approach, the control input to track the one-point transition trajectory element $z_{t,i}(t)$, $u_{t,i}(t)$, and the input to track the individual force-curve $z_{m,i}(t)$, $u_{m,i}(t)$ will be obtained a priori through offline iterations (see Sec. 5.2.3). Therefore, the input for the point-to-point transition, $u_t(t)$, is obtained by superimposing the inputs for one-point transitions together—according to Eq. (5.4) and the input for the force-curve measurements, $u_m(t)$ is obtained similarly via superimposition by Eq. (5.3).

Lemma 4 *Let $u_{t,i}(\cdot)$ be the feedforward control input to track the one-point transition element $z_{t,i}(\cdot)$, and $u_{m,i}(\cdot)$ be the feedforward control input to track the one-point force curve element $z_{m,i}(\cdot)$, then the linearly superimposed input $u_z(t)$ as specified by Eqs. (5.3,5.4,5.6) will track the superimposed trajectory $z_d(t)$.*

Proof *We proceed by examining the superimposition of one one-point transition element $z_{t,i}(\cdot)$ with one one-point force-curve $z_{m,i}(\cdot)$ at any given sample point i on the scan line. By linearity, the superimposed input, $u_{t,i}(\cdot)+u_{m,i}(\cdot)$, will track the combined trajectory $z_{t,i}(\cdot)+z_{m,i}(\cdot)$. Additionally, from the above construction, the one-point transition element $z_{t,i}(\cdot)$ and the one-point force-curve are superimposed in such a way that the output change of the force-curve occurs during the flat stop section of the transition element $z_{t,i}(\cdot)$, i.e.,*

$$z_{t,i}(t)+z_{m,i}(t)=\begin{cases} z_{t,i}(t), & for \quad t\in[t_0,t_1] \\ z_{m,i}(t) & for \quad t\in[t_1,t_2] \end{cases}$$

where $t_t=t_1-t_0$ and $t_m=t_2-t_1$. The above equation implies that such a superimposition of the two trajectories, the one-point transition element $z_{t,i}(\cdot)$ and the one-point force-curve element $z_{m,i}(\cdot)$, avoids the interference of the point-to-point transition with the force-curve measurement at each sample point. This analysis implies that the superimposed input for tracking the entire z-axis trajectory (i.e., the superimposed transition and the force-curve trajectory as in Eq. 5.2) will lead to the desired switching-based motion as described in Sec. 5.2.2.2. ■

Remark 9 *As shown through the development of the stable-inversion theory (Devasia, S. et al. (1996, 1998); Zou, Q. et al. (2007)), the feedforward input to track the one-point transition element, $u_{t,i}(\cdot)$, and that to track the one-point force-curve element, exist, even for nonminimum-phase systems like*

many piezoactuators. Such a feedforward input for nonminimum-phase systems requires the input to be applied before the output change occurs—pre-actuation (or equivalent, preview- actuation). Although achieving exact tracking of the output trajectory (when disturbances including modeling error and noise effects are ignored), required the pre-actuation time (i.e., preview time) to approach infinity, finite pre-actuation (preview) time is usually used in implementations, and the truncation error can be rendered arbitrarily small by having a large enough preview time (Zou, Q. et al. (1999, 2007)). The needed preview-time depends on the minimum distance of the nonminimum-phase zeros relative to the $j\omega$ axis. In force-volume mapping applications, the needed preview time can be determined by using the force-curve element at the first sample point.

Remark 10 *As the element trajectories, $z_{t,i}(\cdot)$ and $z_{m,i}(\cdot)$, are known a priori, it has been established that iterative control approach is highly effective in achieving precision tracking of such pre-known trajectories in practices. Particularly, it has been demonstrated through experiments that the recently-developed MIIC technique can be applied to obtain the feedforward control input for the element trajectories, $z_{t,i}(\cdot)$ and $z_{m,i}(\cdot)$. Similarly, the control input to track the stair-like trajectory for lateral x-axis scanning can also be obtained by using the MIIC technique.*

5.2.3 Model-less Inversion-based Iterative Control (MIIC)

The MIIC algorithm is used to is given below,

$$
\begin{aligned}
u_0(j\omega) &= \alpha y_d(j\omega), \qquad k=0, \\
u_k(j\omega) &= \begin{cases} \frac{u_{k-1}(j\omega)}{y_{k-1}(j\omega)} y_d(j\omega), & \text{when } y_k(j\omega)\neq 0 \\ & \text{and } y_d(j\omega)\neq 0 \quad k\geq 1, \\ 0 & \text{otherwise} \end{cases}
\end{aligned} \tag{5.7}
$$

where $\alpha \neq 0$ is a pre-chosen constant (e.g., α can be chosen as the estimated DC-Gain of the system).

The next theorem finds the convergence of the MIIC algorithm upon the additional disturbance and/or measurement noise, the bound of the MIIC input relative to the desired input, and quantifies the upper-bound of the noise/disturbance-to-signal (NSR) at a given frequency for guaranteeing the improvement

of the output tracking by using the MIIC algorithm, i.e., below which the output tracking at that frequency will be better by using the MIIC algorithm than not tracking that frequency component.

Theorem 4 *Let the system output $y(j\omega)$ is effected by the disturbance and/or the measurement noise as*

$$y(j\omega) = y_l(j\omega) + y_n(j\omega), \tag{5.8}$$

where $y_l(j\omega)$ denotes the linear part of the system response to the input $u(j\omega)$, i.e. $y_l(j\omega) = G(j\omega)u(j\omega)$, and $y_n(j\omega)$ denotes the output component caused by the disturbances and/or measurement noise, at frequency ω,

1. *assume that during each iteration, the NSR is bounded above by a positive, less-than-half constant $\varepsilon(\omega)$, i.e.,*

$$\left|\frac{y_{k,n}(j\omega)}{y_d(j\omega)}\right| \leq \varepsilon(\omega) < 1/2, \quad \forall\ k \tag{5.9}$$

then the ratio of the iterative input to the desired input is bounded in magnitude and phase, respectively, as

$$R_{\min}(\omega) \leq \lim_{k\to\infty}\left|\frac{u_k(j\omega)}{u_d(j\omega)}\right| \leq R_{\max}(\omega), \tag{5.10}$$

where $R_{\min}(\omega) \triangleq 1-\varepsilon(\omega)$ and $\frac{1-\varepsilon(\omega)}{1-2\varepsilon(\omega)} \triangleq R_{\max}(\omega)$,

$$\lim_{k\to\infty}\left|\angle\left(\frac{u_k(j\omega)}{u_d(j\omega)}\right)\right| \leq \sin^{-1}\left(\frac{\varepsilon(\omega)}{1-\varepsilon(\omega)}\right) \triangleq \theta_{\max}(\omega) \tag{5.11}$$

and the relative tracking error is bounded as

$$\lim_{k\to\infty}\left|\frac{y_k(j\omega)-y_d(j\omega)}{y_d(j\omega)}\right| \leq \frac{2\varepsilon(\omega)(1-\varepsilon(\omega))}{1-2\varepsilon(\omega)}; \tag{5.12}$$

2. *The use of the MIIC algorithm will improve the tracking at frequency ω, i.e.,*

$$\lim_{k\to\infty}\left|\frac{y_k(j\omega)-y_d(j\omega)}{y_d(j\omega)}\right| < 1, \tag{5.13}$$

if the NSR is bounded above by $1-\frac{\sqrt{2}}{2} \approx 0.3$, i.e.,

$$\left|\frac{y_{k,n}(j\omega)}{y_d(j\omega)}\right| \leq \varepsilon(\omega) < 1-\frac{\sqrt{2}}{2}, \quad \forall\ k \tag{5.14}$$

Proof Proof is given in .

5.3 Superimposition-based rapid switching-motion control

In this section, we present the superimposition-based control technique and quantify the boundness of the tracking error caused by finite pre-actuation time and its superimposition for the non-minimum phase system. We formulate boundness of the output tracking error problem. The solution begins with the decomposition of the desired trajectory into simple element trajectories. The feedforward control inputs for the element trajectories are computed and superimposed to track desired trajectory. The resulting tracking errors caused by finite pre-actuation time and its superimposition is quantified.

5.3.1 Problem formulation

Consider a time-invariant linear system described by

$$\begin{aligned} \dot{x}(t) &= Ax(t) + Bu(t) \\ y(t) &= Cx(t) \end{aligned} \tag{5.15}$$

where $x(t) \in \mathbb{R}^n$ is the state, $u(t) \in \mathbb{R}^p$ is the input, and $y(t) \in \mathbb{R}^p$ is the output. We assume that the system has a well defined relative degree $r \equiv [r_1, r_2, \cdots, r_p]$ and the system is controllable, non-minimum phase, and hyperbolic.

Definition 1 Boundness of the output tracking error problem. *Given a desired output trajectory $y_d(t)$ to be tracked, quantify a bound of the tracking error using bounded input trajectory with the finite pre-actuation time T_p such that the following requirements are met.*

1. *The given desired output trajectory $y_d(t)$ is defined for $t > 0$, otherwise $y_d(t) = 0$.*

2. *The system equations are satisfied during tracking*

$$\dot{x}(t) = Ax(t) + Bu(t) \tag{5.16}$$

3. *Exact output tracking is achieved if stable inversion control input $u(t) = u_{ff}(t)$ is utilized.*

$$y_d(t) = Cx(t) \tag{5.17}$$

5.3.2 Superimposition-based rapid switching-motion control

5.3.2.1 Decomposition of the desired trajectory into elements of the desired trajectory

In this article, we propose a feedforward control approach that combines offline iterative learning with online implementation via superimposition. First, we decouple the desired trajectory y_d into the desired trajectory elements $y_{d1}, y_{d2}, \cdots, y_{dn}$. We assume that non-zero value of desired trajectory and its element trajectories start from time zero. Since the desired trajectory has its own time delay t_i (see Fig. 5.5), the desired trajectory is decomposed to satisfy the following superimposition, i.e,

$$y_d(t) = \sum_{i=1}^{n} y_{di}(t - t_i)$$

.

Definition 2 Separation time. *Let the desired trajectory elements $y_{d,1}, y_{d,2}, \cdots, y_{d,n}$ are arranged by ascending order of the non-zero desired trajectory element starting time, $t_1 < t_2 < t_3 < \cdots < t_n$ (see Fig. 5.5). Then the separation time $t_{s,i}$ is*

$$t_{s,i} = t_{i+1} - t_i \tag{5.18}$$

Remark 11 *Each desired trajectory elements can be used as the trajectory library for the other different complex desired trajectory tracking problem.*

5.3.2.2 Control input generation by Stable inversion theory and its superimposition

For the each element trajectory, feedforward control input can be generated by stable inversion theory for the MIMO system. For the demonstration purpose, we chose recently developed Model-less Inversion based Iterative Control algorithm and introduced in Section. 5.2.3. Provided that there exist a input $u_{y_{d,i}}$ that tracks the desired trajectory elements exactly and the SPM dynamics can be adequately approximated by a linear system, the exact solution of the input to track the desired trajectory $y_d(t)$, $u_{ff}(t)$, can be obtained by the superimposition of the each individual feedforward input as follows

$$u_{ff}(t) = \sum_{i=1}^{n} u_{y_{d,i}}(t - t_i) \tag{5.19}$$

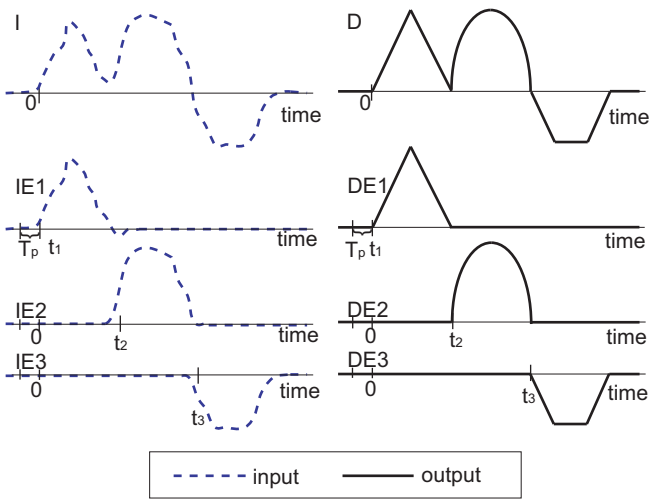

Figure 5.5 Decomposition of the desired trajectory (D) into desired trajectory elements (DE1 $\sim$ DE3) and composition of the input trajectory (I) from the input elements (IE1 $\sim$ IE3).

Since the pre-actuation time to track the desired trajectory must be finite, the finite additional pre-actuation time t_p is introduced (see Fig. 5.5) and the resulting pre-actuation time for each desired trajectory element $T_{p,i}$ is

$$T_{p,i} = t_p + \sum_{n=1}^{i} t_{s,n}$$

where $t_{s,1} = 0$.

Then the finite pre-actuation time transforms the inputs to be truncated from the exact solution of the input as follows

$$u(t) = u_{ff}(t) \qquad \text{for} \quad t > t_p$$

$$\text{otherwise} \qquad u(t) = 0 \tag{5.20}$$

5.3.3 Boundness of superimposed tracking error

The key to the above proposed superimposition based rapid switching-motion control method is to determine the amount of pre-actuation time T_p needed to guarantee the required tracking precision. In this section, we quantify output tracking error caused by finite pre-actuation time. At first, the boundness of the tracking error is analyzed for a desired trajectory element. And the resulting boundness of tracking error from superimposition of finite or infinite number of element desired trajectories are to

be analyzed. The proper choice of pre-actuation time and separation time is proposed for the complex desired trajectory tracking.

Output Tracking Form (H. Perez. et al. (2004)). Consider a system described in Eq. (5.15). With the proper state transformation, the states can be defined by

$$x(t) = \left[\xi(t)^T, \eta_s(t)^T, \eta_u(t)^T\right]^T \tag{5.21}$$

, where $\xi(t)$ denotes $[y_1, y_2, \cdots, y_p, \dot{y_1}, \dot{y_2}, \cdots, \dot{y_p}, \cdots, y_p^{(r-1)}]^T$ and r denotes a well defined relative degree. $\eta_s(t)$ and $\eta_u(t)$ denotes stable internal dynamic states and unstable internal dynamic states respectively. Then $C = [I_{p\times p}, 0, \ldots, 0]_{p\times n}$.

By using model-based inversion approaches there exists feedforward control input $u_{ff}(t)$ that tracks the desired output trajectory $y_d(t)$ and state trajectory $x_d(t)$ as follows:

$$u_{ff}(t) = \hat{B}_s\eta_s(t) + \hat{B}_u\eta_u(t) + \hat{B}_\xi \mathbb{Y}_d(t)$$

where $\mathbb{Y}_d = \left[\xi^T, y^{(r)}\right]^T$ that transforms the system (5.15) into the output-tracking form:

$$\begin{aligned} \dot{\xi}(t) &= \dot{\xi}_d(t) \\ \begin{bmatrix} \dot{\eta}_s \\ \dot{\eta}_u \end{bmatrix} &= \begin{bmatrix} A_s & 0 \\ 0 & A_u \end{bmatrix} \begin{bmatrix} \eta_s \\ \eta_u \end{bmatrix} + \begin{bmatrix} B_s \\ B_u \end{bmatrix} \mathbb{Y}_d \end{aligned}$$

where A_u, A_s have all the eigenvalues on the open right hand side and the open left hand side respectively Zou, Q. et al. (1999). Then the bounded solution to the internal dynamics in the transformed coordinates can be found as

$$\begin{aligned} \eta_s(t) &= \int_{-\infty}^{t} e^{A_s(t-\tau)} B_s \mathbb{Y}_d(\tau) d\tau \\ \eta_u(t) &= -\int_{t}^{\infty} e^{-A_u(\tau-t)} B_u \mathbb{Y}_d(\tau) d\tau \end{aligned}$$

The state trajectory and output trajectory satisfy the following equation.

$$\begin{aligned} x_d(t) &= e^{A(t+T_p)} x_d(-T_p) + \int_{-T_p}^{t} e^{A(t-\tau)} B u_{ff}(\tau) d\tau \\ &= \int_{-\infty}^{-T_p} e^{A(t-\tau)} B u_{ff}(\tau) d\tau + \int_{-T_p}^{t} e^{A(t-\tau)} B u_{ff}(\tau) d\tau \\ y_d(t) &= C x_d(t) \end{aligned}$$

where $-T_p$ is any arbitrary time instant before $t = 0$.

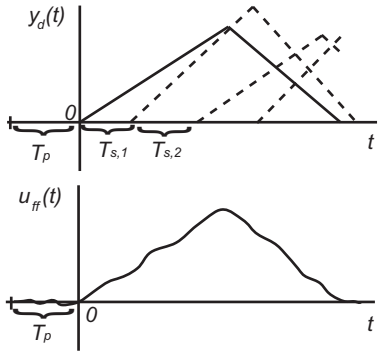

Figure 5.6 Desired trajectory $y_d(t)$ and its tracking input $u_{ff}(t)$.

Lemma 5 *Let the desired trajectory y_d and its time derivatives upto the relative degree r be bounded, i.e. there exists a positive scalar $M \in \mathbb{R}$, such that the standard Euclidean norm $\left\| [y_d, \dot{y}_d, \ddot{y}_d, \cdots, y_d^{(r)}] \right\|_2 \leq M$ for all time t. Then, the output tracking error $\|e_y(t)\|_2$ with a finite pre-actuation time T_p is bounded by*

$$\|e_y(t)\|_2 \leq \frac{M_A M_{A_u} \|B_u\|_2 e^{-(\alpha+\beta)T_p}}{\beta} \sup_{\tau} \|\mathbb{Y}_d(\tau)\|_\infty$$

where the constant M_A, M_{A_u}, α andβ satisfies the following Hurwitz matrix inequality.

$$\left\| e^{At} \right\|_2 \leq M_A e^{-\alpha t}$$
$$\left\| e^{-A_u t} \right\|_2 \leq M_{A_u} e^{-\beta t}$$

Proof: Suppose that the input signal $u(t)$ is

$$\begin{aligned} u(t) &= u_{ff}(t) \quad \text{for } t \geq -T_p \\ u(t) &= 0 \quad \text{for } t < -T_p. \end{aligned}$$

Then the state trajectory $x(t)$ and the state trajectory tracking error $e_x(t)$ for $t > 0$ is to be:

$$\begin{aligned} x(t) &= \int_{-T_p}^{t} e^{A(t-\tau)} B u_{ff}(\tau) d\tau \\ e_x(t) &= x_d(t) - x(t) \\ &= e^{A(t+T_p)} x_d(-T_p) \end{aligned} \tag{5.22}$$

Notice that

$$\begin{aligned} x_d(-T_p) &= \begin{bmatrix} \mathbb{Y}_d(-T_p) \\ \eta_s(-T_p) \\ \eta_u(-T_p) \end{bmatrix} \\ &= \begin{bmatrix} \mathbb{Y}_d(-T_p) \\ \int_{-\infty}^{-T_p} e^{A_s(-T_p-\tau)} B_s \mathbb{Y}_d(\tau) d\tau \\ -\int_{-T_p}^{\infty} e^{-A_u(T_p+\tau)} B_u \mathbb{Y}_d(\tau) d\tau \end{bmatrix} \end{aligned}$$

Notice that $y_d(t) = [0]$ and $Y_d(t) = [0]_{r\times 1}$ for $t \leq 0$, then

$$x_d(-T_p) = \begin{bmatrix} 0 \\ 0 \\ -\int_0^{\infty} e^{-A_u(T_p+\tau)} B_u \mathbb{Y}_d(\tau) d\tau \end{bmatrix}$$

Since A and $-A_u$ is Hurwitz matrix, the norm of the state tracking error and output tracking error is

$$\begin{aligned} \|e_x(t)\|_2 &\leq \left\| e^{A(t+T_p)} \right\|_2 \|x_d(-T_p)\|_2 \\ &\leq M_A e^{-\alpha t} e^{-\alpha T_p} \int_0^{\infty} \left\| e^{-A_u(T_p+\tau)} \right\|_2 \|B_u\|_2 \|\mathbb{Y}_d(\tau)\|_{\infty} d\tau \\ &\leq \frac{M_A M_{A_u} \|B_u\|_2 e^{-(\alpha+\beta)T_p}}{\beta} \sup_{\tau} \|\mathbb{Y}_d(\tau)\|_{\infty} \\ \|e_y(t)\|_2 &= \|y_d(t) - y(t)\|_2 \\ &\leq \|C\|_2 \|x_d(t) - x(t)\|_2 \quad (\text{with} \quad \|C\|_2 = 1) \\ &\leq \frac{M_A M_{A_u} \|B_u\|_2 e^{-(\alpha+\beta)T_p}}{\beta} \sup_{\tau} \|\mathbb{Y}_d(\tau)\|_{\infty} \end{aligned}$$

This completes the proof. ■

The next theorem shows that the superimposed output tracking error is to be bounded and can also be made small by choosing a sufficiently large pre-actuation time.

Theorem 5 *Let the desired trajectory elements $y_{d,1}, y_{d,2}, \cdots, y_{d,n}$ and its time derivatives upto the relative degree r be bounded, i.e. there exists a positive scalar $M \in \mathbb{R}$, such that, for $Y_{d,i} = \left[y_{d,i}, \dot{y_{d,i}}, \ddot{y_{d,i}}, \cdots, y_{d,i}^{(r)} \right]^T$,*

$$\left\| \left[Y_{d,1}^T, Y_{d,2}^T, \cdots, Y_{d,n}^T \right]^T \right\| \leq M \quad \textit{for all time} \quad t. \tag{5.23}$$

Then for the given constants $T_s^* = min\{T_{s,n}\}$, the resulting output tracking error $e_y(t)$ is bounded by

$$\|e_y(t)\|_2 \leq \frac{M_A M_{A_u} \|B_u\|_2 e^{-(\alpha+\beta)T_p}}{\beta} \frac{\max_i \{\sup_\tau \|\mathbb{Y}_{d,i}(\tau)\|_\infty\}}{1-e^{-(\alpha+\beta)T_s^*}}$$

Proof: From the Lemma. 5,the summation of each tracking error $e_y(t)$ caused by superimposition of the desired trajectory elements is

$$\begin{aligned}
\left\|e_y(t)\right\|_2 &= \sum_{i=1}^{n} \left\|e_{y,i}(t)\right\|_2 \\
&\leq \sum_{i=1}^{n} \frac{M_A M_{A_u} \|B_u\|_2}{\beta} \sup_\tau \left\|\mathbb{Y}_{d,i}(\tau)\right\|_\infty e^{-(\alpha+\beta)T_{p,i}} \\
&\leq \frac{M_A M_{A_u} \|B_u\|_2}{\beta} \max_i \left\{\sup_\tau \left\|\mathbb{Y}_{d,i}(\tau)\right\|_\infty\right\} \sum_{i=1}^{n} e^{-(\alpha+\beta)(T_p - T_s^* + iT_s^*)} \\
&\leq \frac{M_A M_{A_u} \|B_u\|_2 e^{-(\alpha+\beta)T_p}}{\beta} \max_i \left\{\sup_\tau \left\|\mathbb{Y}_{d,i}(\tau)\right\|_\infty\right\} \frac{1-e^{-(\alpha+\beta)T_s^* n}}{1-e^{-(\alpha+\beta)T_s^*}}
\end{aligned}$$

Then

$$\lim_{n\to\infty} \left\|e_y(t)\right\|_2 \leq \frac{M_A M_{A_u} \|B_u\|_2 e^{-(\alpha+\beta)T_p}}{\beta} \frac{\max_i \{\sup_\tau \left\|\mathbb{Y}_{d,i}(\tau)\right\|_\infty\}}{1-e^{-(\alpha+\beta)T_s^*}}$$

■

Remark 12 *Theorem 5 implies that the sum of the distances from stable pole and unstable zero to the imaginary axis in complex plane affects the boundness of the output tracking error. Since $1 - e^{-(\alpha+\beta)T_s^*} < 1$, the boundness of the output tracking error is governed by the pre-actuation time. As the distance of the sum increases, the smaller pre-actuation time can be chosen to achieve the desired output tracking accuracy. And sufficiently large pre-actuation time can be chosen to achieve the desired output tracking accuracy for a given system.*

5.4 Experimental Example: Elasticity and adhesion force volume mapping on a line

In this section, we illustrate the MIIC technique by implementing it into the output tracking of a piezotube actuator on an AFM system. We start with describing the experimental system first.

5.4.1 Experimental setup

The schematic diagram of the experimental AFM system (Dimension 3100, Veeco Inc.) is shown in Fig. 5.7 for the control of the *x*-axis piezotube actuator. All the control inputs to the piezo actuator

were generated by using MATLAB-xPC-target package, and sent out through a data acquisition card (DAQ) to drive the piezo actuator via an amplifier.The AFM-controller had been customized so that the PID control circuit was bypassed when the external control input was applied.

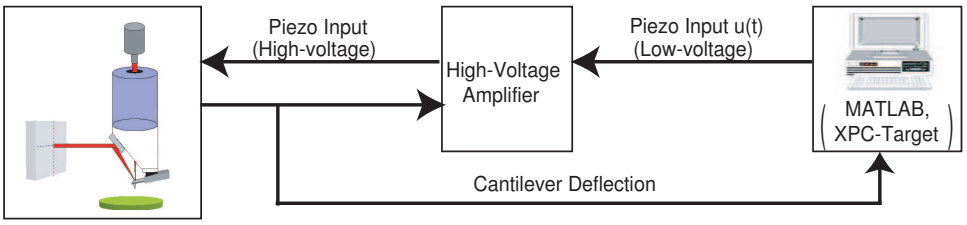

Figure 5.7 Schematic diagram of the experiment setup to implement the proposed MIIC algorithm

5.4.2 Implementation of the Switching-motion-based force-volume mapping

The proposed switching-motion based force-volume mapping is illustrated by using a PDMS sample as an example. The stair-like desired trajectory for the lateral *x*-axis scanning was specified first. The scan size was chosen at $40\mu m$, and a total of 128 force curves were measured per scan line (i.e., R = 128). Moreover, two different duty ratios (D = 20 and 50) for the stop-and-go section of each stair in the *x*-axis trajectory (see Sec. 5.2.2.1), along with three different *x*-axis lateral scan rates (f = 0.5, 1, 2 (Hz)), were chosen in the experiments. Therefor, the transition time t_t, the measurement time t_m, and the point-to-point spatial distance ℓ_s, are also specified accordingly (see Sec. 5.2.2.1). For example, for the the case of 2 Hz lateral line scan speed and duty ratio of D=20, the transition time ($t_t = 1.563$ ms), the measurement times ($t_m = 0.39$ ms), and the point-to-point spatial distance ($l_s = 313nm$) were determined. Once the *x*-axis desired trajectory was determined, the *z*-axis desired trajectory can be determined accordingly. Particularly, the total trajectory for the force-curve measurements ($z_m(t)$ in Eq. (5.6)) was designed by choosing the vertical displacement of each force-curve element ($z_{m,i}$ in Eq. (5.6)) as 800 nm. As shown in Fig. 5.2 (b2), each force-curve consisted of a triangle trajectory followed by a flat section, and to be synchronized with *x*-axis motion, the duration of the triangle part and the duration of the flat part were equivalent to the measurement time t_m and the transition time t_t, respectively. The triangle part was symmetric with the same push-in time and the pull-up time. Similarly, the total trajectory for the point-to-point transition ($z_{t,i}$ in Eq. (5.4)) was designed by specifying

the one-point transition element also. In this experiment, we simplified the design of the library of elements for one-point transitions (see Sec. 5.2.2.2 and Eq. (5.4)) by having only one element for one-point transition. Specifically, the element for one-point transition was chosen to have a displacement range of 98 nm, corresponding to one voltage displacement sensor output. Then the total transition trajectory was determined by scaling the one-point transition element according to the transition height at each sample point (see Eq. 5.4 and Sec. 5.2.2.2). Next, the MIIC control algorithm was used to find, ahead of time, the converged inputs for tracking the stair-like x-axis desired trajectory, and then the force-curve element along with the one-point transition element, respectively. The obtained control inputs were stored and applied appropriately during the force volume mapping on one scan line (such that the switching-motion in the lateral scanning was synchronized with the force-curve and transition switching in the vertical direction). We demonstrated the technique by measuring the force-volume mapping on one scan line, and the sample topography profile was obtained a priori by iteratively using the absolute mode force-curve measurement along the scan line (to avoid applying excessively large load force, we note that the sample topography profile can be obtained a priori via high-speed imaging (Ying Wu. et al. (2008)), in this chapter, however, we focus on the high-speed force-volume mapping).

5.4.3 Experimental Results & Discussion

We start with presenting the experimental tracking results in both the x-axis and the z-axis, followed by the force-volume mapping results.

5.4.3.1 Experimental output tracking results

The output tracking results achieved by using the MIIC control technique are compared with those obtained by using the DC-Gain method in Figs. 5.8 and 5.9 for the tracking of the stair-like x-axis trajectory and the tracking of the force-curve element and the one-point transition element. In the DC-Gain method, the control input was obtained by scaling the desired output with the DC-Gain of the system. Therefore, the DC-Gain method did not account for the dynamics of the system, and the obtained output tracking quantitatively demonstrate the effects of the SPM dynamics on the positioning

Table 5.1 Tracking errors by using the MIIC technique for the x-axis trajectory, the force-curve element, and the one-point transition element. The RMS error $E_2(\%)$ and the maximum error $E_{max}(\%)$ are defined in Eq. (5.24).

Scan Rate	Duty Rate	App. Rate(mm/s)	E_2 (%)			E_{max} (%)		
			X	Z_m	Z_t	X	Z_m	Z_t
0.5 Hz	20	1.02	0.77	3.76	1.17	0.63	1.51	2.94
0.5 Hz	50	0.41	1.16	0.65	3.38	0.45	2.34	1.18
1 Hz	20	2.05	1.16	1.69	0.98	0.5	3.95	3.06
1 Hz	50	0.82	1.74	0.7	0.92	0.44	2.51	2.93
2 Hz	20	4.1	1.92	3.55	0.67	0.39	6.33	1.72
2 Hz	50	1.64	2.95	1.03	0.68	0.35	2.95	1.79

precision. In Fig. 5.8 and 5.9, the tracking results are shown for the scan rates of 0.5 Hz and 2 Hz with duty ratio D = 50 and D = 20, respectively, where the load rate of the force-curve equaled to 0.41 mm/s and 4.1 mm/s, respectively. (Experimental results for the other 4 different scanning and duty combinations were omitted due to the page limits). When implementing the MIIC technique, the iteration was stopped when neither the relative RMS-tracking error nor the relative maximum-tracking-error decreased further. The resulting tracking results are shown in Table. 5.4.3.1 in terms of the relative RMS error $E_2(\%)$ and the relative maximum error $E_\infty(\%)$, as defined below,

$$E_2(\%) \triangleq \frac{\|y_d(\cdot)-y(\cdot)\|_2}{\|y_d(\cdot)\|_2}\times 100\%, E_\infty(\%) \triangleq \frac{\|y_d(\cdot)-y(\cdot)\|_\infty}{\|y_d(\cdot)\|_\infty}\times 100\%. \tag{5.24}$$

The experimental results show that precision tracking in the proposed switching-motion based force-volume mapping can be achieved by using the MIIC technique. As shown in Fig. 5.8 and Table 5.4.3.1, when the lateral scan rate and the load-rate of the force-curves were relatively low, the dynamics effect was small, thereby the tracking errors of the force-curve element and the one-point transition element by using the DC-gain method were relatively small (around 5%). Instead, due to the large lateral scanning range (40 μm), the hysteresis effect was pronounced (see Fig. 5.8 (a1), (b1)). However, by using the proposed MIIC technique, such a large hysteresis effect was substantially removed (as shown in Fig. 5.8 (b1), the tracking error was close to the noise level), and so were the error in the force-curve element and the one-point transition element tracking (see Fig. 5.8 (a2) to (b3)). When both the lateral scan rate and the load-rate of the force-curve were increase by 4 times to 2 Hz and 10 times to 4.1 mm/sec, respectively, the dynamics effect became significant and resulted in large

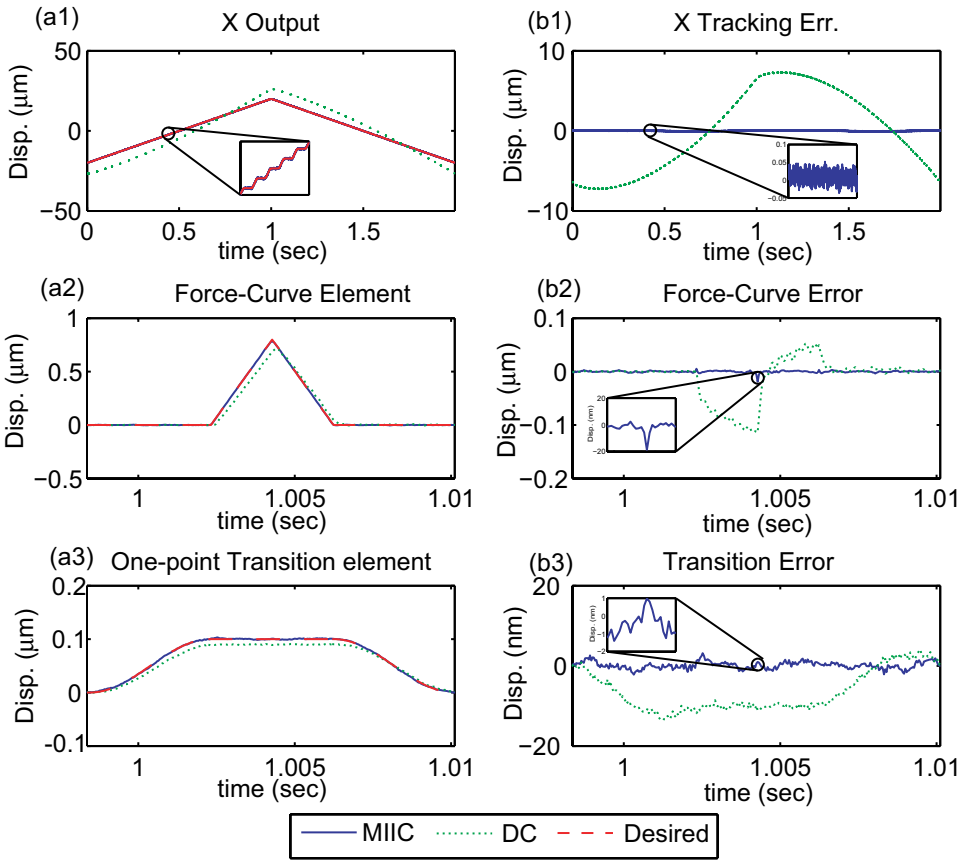

Figure 5.8 Experimental tracking results for the line scan rate of 0.5 Hz, and the duty ratio D = 50, where the load rate of the force-curve is 0.41 mm/sec.

oscillations in the force-curve element and the one-point transition tracking results when DC-Gain method was used (see Fig. 5.9 (a2), (b2), (a3), and (b3)). However, precision tracking was still maintained by using the MIIC algorithm, and the tracking error was still small and less than 3% (see Fig. 5.9 and Table 5.4.3.1). Therefore, the experimental results show that precision tracking in the proposed switching-motion based force-volume mapping can be achieved by using the MIIC technique.

5.4.3.2 Force-Volume Mapping of a PDMS Sample

The converged control inputs to the tracking of the *x*-axis and the *z*-axis trajectories, obtained above, were apply to measure the force-volume mapping on a PDMS sample. The PDMS sample was

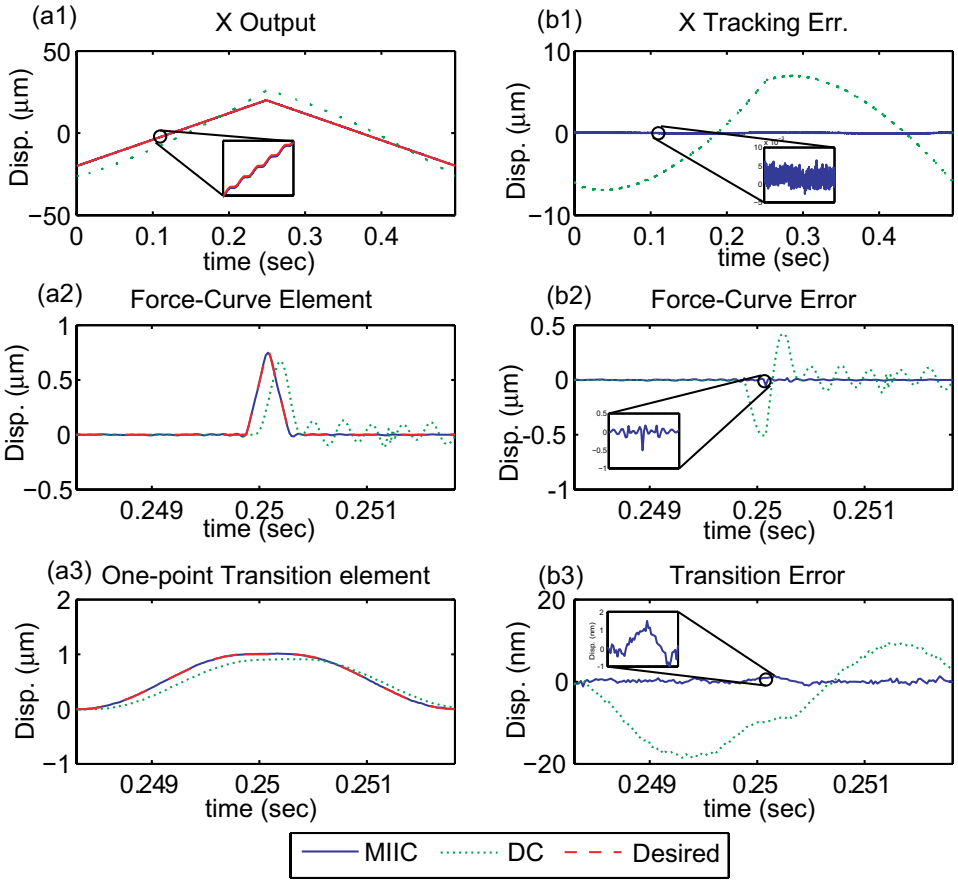

Figure 5.9 Experimental tracking results for the scan rate of 2 Hz, and the duty ratio D = 20, where the load rate of the force-curve equaled to 4.1 mm/sec.

prepared as describe in (K.-S. Kim. et al. (2007)). The preparation process ensured that the PDMS sample is homogeneous, i.e., the mechanical properties of the sample remained almost the same across the entire sample area. First, the sample topography was obtained as described earlier, then the obtained sample topography was partitioned by using the lateral spatial resolution (R = 128), which was then used to determine the scale factor h_i for the control input to the one-point transition element at each sample point. Then the *z*-axis control input was obtained via superimposition as described in Sec. 5.2.2.2, and was synchronized with the *x*-axis control input during the implementation. The obtained force-volume mapping results over one scan line are shown in Fig. 5.10 for the line scan rate of 0.5 Hz and the force load rate of 0.41 mm/sec, and in Fig. 5.11 for the line scan rate of 2 and the force rate of 4.1 mm/sec.

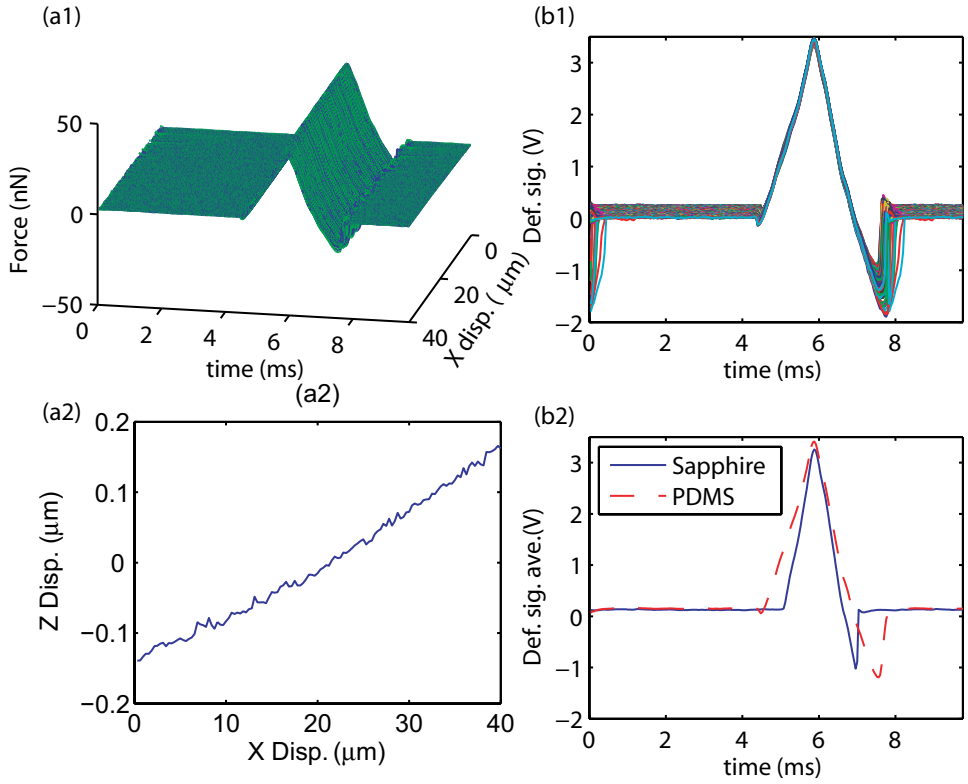

Figure 5.10 (a1) The 3-D plot and (b1) the side view of the force-volume mapping on the PDMS sample, (a2) the sample topography across the scan line, and (b2) the comparison of the force-time curve on the PDMS with that on a sapphire sample. The load rate is $0.41 mm/s$.

The experimental results show that force-volume mapping speed can be significantly improved by using the proposed approach. As shown in Fig. 5.11 (a1), the force-curves measured at all sampled points were very close to each other, which is even more clear in the side-view of the force-volume mapping result in Fig. 5.11 (b1). Such a uniformity across the sampled point implied that the mechanical properties at all sampled points were very close to each other, i.e., the PDMS sample was homogeneous. Thus, the measured force-volume mapping results agree with our expectation. We note that such measurement results were achieved when there existed significant sample topography variation across the 40 μm scan line—-as shown in Fig. 5.11 (a2). Thus, the experimental results showed that the proposed method can effectively remove the sample topography effect on the force-volume mapping when the scan rate and the force load rate were relatively low. Such an ability, to remove

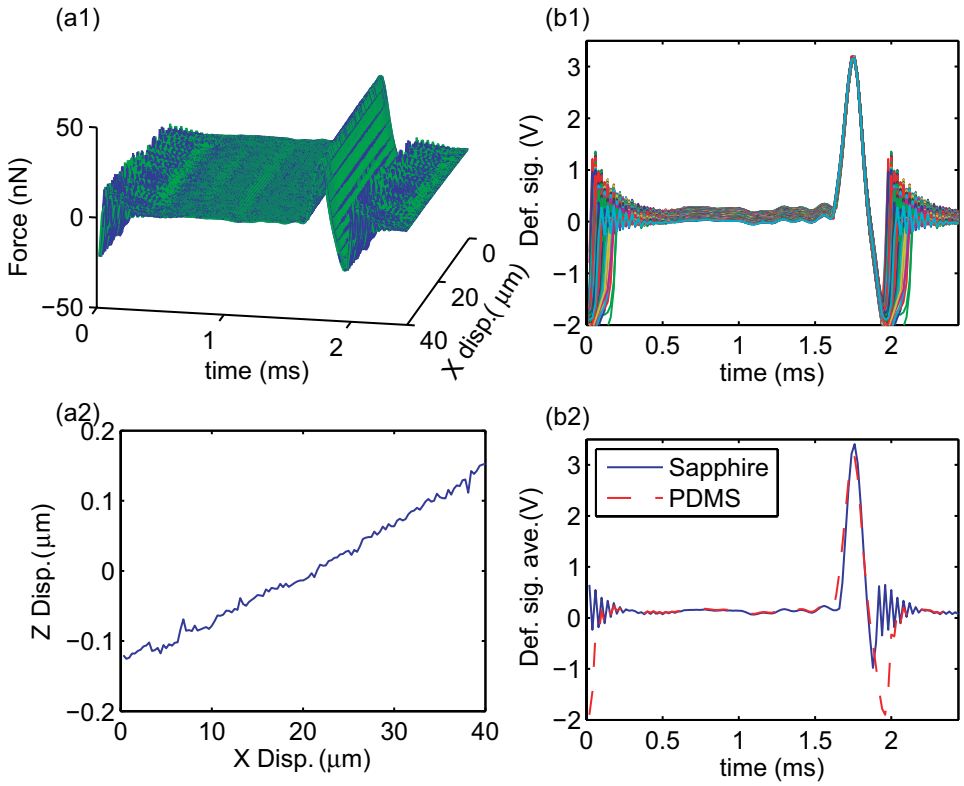

Figure 5.11 (a1) The 3-D plot and (b1) the side view of the force-volume mapping on the PDMS sample, (a2) the sample topography across the scan line, and (b2) the comparison of the force-time curve on the PDMS with that on a sapphire sample. The load rate is $4.1 mm/s$.

the sample topography effect on the force-volume mapping, was maintained even when the scan rate and the force load rate were increased by 10-fold, as shown in Fig. 5.11. Finally, we also compared the force-curves measured on the PDMS sample with those measured on the Sapphire sample for the same control input at the load rate of 0.41 mm/sec and 4.1 mm/sec, as shown in Fig. 5.10 (b2) and Fig. 5.11 (b2), respectively. The obtained experimental results show the rate-dependent elastic modulus of PDMS (K.-S. Kim. et al. (2007)). Note the slope of the force-curves shown in Fig. 5.10 (b2) and Fig. 5.11 (b2) is proportional to the elastic modulus of the material (H.-J. Butt. et al. (2005)). When the load-rate was slow, the PDMS sample tended to behave softer with a lower elastic modulus, i.e., the slope of the force curve is smaller—as shown in Fig. 5.10 (b2). As the load rate was increased, the PDMS sample tended to behave stiffer with a higher elastic modulus, i.e., the slope of the force curve was larger and close to that of sapphire—as shown in Fig. 5.11 (b2). Such a trend agrees with

our recent results reported in (K.-S. Kim. et al. (2007)). Therefore, the experimental results illustrate the efficacy of the proposed approach to achieve high-speed force-volume mapping.

5.5 Conclusions

In this chapter, high-speed force-volume mapping using switching-motion based force-volume mapping mode and model-less inversion based iterative control technique on atomic force microscopy is presented. The proposed approach was based on signal decoupling-superimposition and the elemental input signals were found by MIIC technique. The proposed methods is implemented to obtain the force-curve mapping of a PDMS sample on one scan line dealing with high-speed force-curve measurement at each sample point and rapid transition of the probe from one sample point to the next while compensating for the sample topography difference between the two points, with no sliding of the probe on the sample with seamless integration of the above two motions. The experimental results were presented and showed that the force mapping speed with precision force curve measurement can be increased by over 20 times.

CHAPTER 6. Conclusion

This dissertation presented a suite of systematic inversion-based feedforward control approaches to design and track output trajectory. At first, we discussed optimal scan trajectory design and control (OSDC) with application to atomic force microscope (AFM) based material property measurement. Based on active scan trajectory, optimum transition trajectory and the boundary conditions were found by OSDC technique. Since the piezo-electric actuator of the AFM system have lightly-damped resonant peaks, resulting in output transition trajectory with large oscillations. The adverse effect of the output oscillation was addressed. To minimize output trajectory oscillations, input energy minimization was transformed to the minimization of the output energy in frequency domain and the effect of the lightly-damped resonant peaks was minimized through the pre-filter design.

The development of inversion-based feedforward control techniques to track the desired trajectory is the main portion of this dissertation. The first control issue addressed was to remove or minimize the effect of the a modeling error, system uncertainty and repetitive disturbance. For this problem, we extended the iterative learning control approach. As the extension of the inversion-based iterative control (IIC) in frequency domain, enhanced IIC technique increased the range of convergence conditions and the speed of convergence better than conventional IIC technique. And the implementation into the adhesion force measurement and time-dependent elastic modulus measurement showed the effectiveness of the trajectory design by OSDC technique and its tracking performance by enhanced IIC technique. Model-less IIC was an extended development from the enhanced IIC. The model-less IIC technique doesn't require modeling process as a preparation. As a result, the model-less IIC removed every issues related with the modeling errors and introduced simplicity on its implementation. As a major difference from the other iterative learning control technique, model-less IIC guarantees one step convergence for the linear time invariant system without disturbance existence. The convergence analysis on the system

with the existence of disturbance was presented and gave a guideline of acceptable bound of noise for the better tracking performance. The experiments of the white noise type of complex trajectory and triangle trajectories tracking convinced efficacy of the proposed control technique and convergence of model-less IIC on the system with the hysteresis.

Then the implementation of model-less IIC technique was extended with the notion of superimposition to non-repetitive trajectory tracking. To make the control problem more simple, the desired trajectory was decomposed into several element desired trajectories. The element desired trajectory tracking was achieved by model-less IIC and superimposed to tracking given desired trajectory. Since the stable inversion theory implied that the required pre-actuation time for the nonminimum phase system is infinite, another practical issue that the limited finite pre-actuation time and the resulting tracking error was analyzed. For the precision trajectory tracking by the superimposition of the element trajectories, the tracking error caused by the pre-actuation time and the minimum superimposing time difference was quantified. Then each directional trajectory tracking signals were synchronized for the high-speed force-volume mapping on PDMS. The experimental results showed that the proposed tracking control technique can improve the measurement speed much better than current commercial device.

BIBLIOGRAPHY

S. Kawamura, F. Miyazaki, and S. Arimoto. (1988). Realization of robot motion based on a learning method. *IEEE Transactions on Systems, Man and Cybernetics*, *18*(1), 126-134

C. Atkeson, J. McIntyre. (1986). Robot Trajectory Learning Through Practice. *Proceeding of IEEE International Conference on Robotics and Automation*, *3*(), 1737- 1742

P. Bondi, G. Casalino, and L. Gambardella. (1988). On the Iterative Learning Control Theory for Robotic Manipulators. *IEEE Journal of Robotics and Automation*, *4*(1), 14-22

M. Uchiyama. (1978). Formation of high speed motion pattern of mechanical arm by trial. *Trans. of the Society of Instrumentation and Control Engineers*, *19*(), 706-712

S. Arimoto, S. Kawamura, and F. Miyazaki. (1984). Bettering Operation of Dynamic Systems by Learning: A New Control Theory for Servomechanism or Mechatronics Systems. *Proceeding of 23rd Conference on Decision and Control*, (), 1064-1069

L. R. Hunt, G. Meyer, and R. Su. (1996). Noncausal Inverses for Linear Systems. *IEEE Trans. on Automatic Control*, *41*(8), 608-611

L. Silverman. (1969). Inversion of multivariable linear systems. *IEEE Trans. on Automatic Control*, *14*(3), 270-276

R. M. Hirschorn. (1979). Invertibility of multivariable nonlinear control systems. *IEEE Trans. on Automatic Control*, *24*(6), 855-865

B. A. Francis. (1976). The linear multivariable regulator problem. *IEEE Conference on Decision and Control including the 15th Symposium on Adaptive Processes*, *15*(), 873-878

A. Isidori and C. I. Byrnes. (1990). Output regulation of nonlinear systems *IEEE Transactions on Automatic Control*, *35*(2), 131-140

R. Wiesendanger. (1994). *Scanning Probe Microscopy and Spectroscopy*, Cambridge University Press.

K. O. van Werf, C. A. J. Putman, B. G. de Grooth, and J. Greve. (1994). Adhesion force imaging in air and liquid by adhesion mode atomic force microscopy. *Applied Physics Letter*, *65*(9), 1195-1197.

F. Filhol, E. Defay, C. Divoux, C. Zinck, and M. Delaye. (2005). Resonant micro-mirror excited by a thin-film piezoelectric actuator for fast optical beam scanning. *SENSORS AND ACTUATORS A-PHYSICAL*, *123*(), 483-489

F. Zimmer, H. Grueger, A. Heberer, T. Sandner, A. Wolter, and H. Schenk. (2005). Scanning micro-mirrors: From bar-code-scanning to spectroscopy *OPTICAL SCANNING (S. Sagan and G. Marshall, eds.) 5873*(), 84-94

R.-F. Fung, J. S. Huang, C. G. Chien, and Y. C. Wang. (2000). Design and application of a continuous repetitive controller for rotating mechanisms. *International Journal of Mechanical Sciences*, *42*(), 1805-1819

S. Huang and W. Shen. (2005). Development of a multi-optical source rapid prototyping system. *INTERNATIONAL JOURNAL OF ADVANCED MANUFACTURING TECHNOLOGY*, *27*(1), 63-69

H. Perez, Q. Zou, and S. Devasia. (2004). Design and control of optimal scan trajectories: Scanning tunneling microscope example. *ASME Journal of Dynamic Systems, Measurement and Control*, *126*(1), 187-197

C. Cloet, M. Tomizuka, and R. Horowitz. (2001). Design requirements and reference trajectory generation for a copier paper-path. *IEEE/ASME International Conference on Advanced Intelligent Mechatronics Proceedings*, (), 911-916

A. Piazzi and A. Visioli. (2000). Minimum-time system-inversion based motion planning for residual vibration reduction. *IEEE/ASME Trans. Mechatron*, *5*(1), 12-22

A. V. Dowd and M. D. Thanos. (2000). Vector motion processing using spectral windows. *Control System Magazine, 20*(), 8-19

F. L. Lewis and V. L. Syrmos. (1995) *Optimal Control*, New York: John Wiley and Sons, second ed.

Q. Zou, K. K. Leang, E. Sadoun, M. J. Reed, and S. Devasia. (2004). Control issues in high-speed AFM for biological applications:Collagen imaging example. *Special Issue on "Advances in Nano-technology Control", Asian Journal Control*, *8*(2), 164-178

S. Tien, Q. Zou, and S. Devasia. (2005). Iterative Control of dynamics-coupling effects in piezo-actuator for high-speed AFM operation. *IEEE Trans. on Control Systems Technology*, *13*(6), 921-931

A. Isidori *Nonlinear Control Systems*, London: Springer-Verlag, 1995

W. Rudin. (1966) *Real and Complex Analysis*, New York: McGraw-Hill, third ed.

J. M. Ortega (1987) *Matrix Theory: A second course*, University series in mathematics (Plenum Press), New York: Plenum Press

J. Ghosh and B. Paden. (2000). Nonlinear repetitive control. *IEEE Trans. on Automatic Control*, *45*(5), 949-954

L. Moore, K. and J.-X. E. Xu. (2000). Special issue on iterative learning control. *International Journal of Control*, *73*(10), 819-823

Y. Wu and Q. Zou. (2007). Iterative control approach to compensate for both the hysteresis and the dynamics effects of piezo actuators. *IEEE Trans. on Control Systems Technology*, *15*(5), 936-944

B. Cappella and G. Dietler. (1999). Force-distance curves by atomic force microscopy. *Surface Science Reports*, *34*(1-3), 1-104

H.-J. Butt, B. Cappella, and M. Kappl. (2005). Force Measurements with the Atomic Force Microscope: Technique, interpretation and application. *Surface Science Reports*, *59*(), 1-152

M. D. Louey, P. Mulvaneyb, and P. J. Stewarta. (2001). Characterization of adhesional properties of lactose carriers using atomic force microscopy. *Journal of Pharmaceutical and Biomedical Analysis*, *25*(3-4), 559-567

O. H. Willemsen, M. M. E. Snel, K. O. van der Werf, B. G. de Grooth, J. Greve, P. Hinterdorfer, H. J. Gruber, H. Schindler, Y. van Kooyk, and C. G. Figdor. (1998). Simultaneous height and adhesion imaging of antibody-antigen interactions by atomic force microscopy. *Biophysical Journal*, *75*(5), 2220-2228

O. H. Willemsen, M. M. E. Snel, K. O. van der Werf, B. G. de Grooth, J. Greve, P. Hinterdorfer, H. J. Gruber, H. Schindler, Y. van Kooyk, and C. G. Figdor. (2004). Elasticity and adhesion force mapping reveals real-time clustering of growth factor receptors and associated changes in local cellular rheological properties. *Biophysical Journal*, *86*(), 1753-1762

S.-J. Marrink, O. Berger, P. Tieleman, and F. Jahnig. (1998). Adhesion forces of lipids in a phospholipid membrane studied by molecular dynamics simulations. *Biophysical Journal*, *74*(2), 931-943

M.-S. Tsai and J.-S. Chen. (2003). Robust tracking control of a piezoacuator using a new approximate hysteresis model. *ASME Journal of Dynamic Systems, Measurement and Control*, *125*(), 96-102

B. L. Weeks, M. W. Vaughn, and J. J. DeYoreo. (2005). Direct imaging of meniscus formation in atomic force microscopy using environmental scanning electron microscopy. *Langmuir*, *21*(), 8096-8098

K. Kim, Q. Zou, and C. Su. (2007). Iteration-based scan-trajectory design and control with output-oscillation minimization: Atomic force microscope example. *Proceedings of American Control Conference (New York City), July 2007*, (),

A. L. Weisenhorn and P. K. Hansma. (1989). Forces in atomic force microscopy in air and water. *Applied Physics Letter*, *54*(26), 2651-2653

P. P. Lehenkari, G. T. Charras, S. A. Nesbitt, and M. A. Horton. (2000). New technologies in scanning probe microscopy for studying molecular interactions in cells. *Expert reviews in molecular medicine*, (), 1-19

M. Radmacher, J. C. M. Fritz, D. Walters, and P. Hansma. (1994). Imaging Adhesion Forces and Elasticity of Lysozyme Adsorbed on Mica with the Atomic Force Microscope. *Langmuir*, *10*(), 3809-3814

A. L. Weisenhorn, P. Maivald, H.-J. Butt, and P. Hansma. (1992). Measuring adhesion, attraction, and repulsion between surfaces in liquids with an atomic-force microscope. *Physical Review. B*, *45*(19), 11226-11232

N. A. Burnham and R. J. Colton. (1989). Measuring the nano-mechanical properties and surface forces of materials using an atomic force microscope. *Journal of Vacuum Science* & *Technology, A: Vacuum, Surfaces, and Films*, *7*(4), 2906-2913

A-Hassan. Emad, William F. Heinz, Matthew Antonik, Neill P. D'Costa, Soni Nageswaran, Cora-Ann Schoenenberger and Jan H. Hoh (1989). Relative Microelastic Mapping of Living Cells by Atomic Force Microscopy. *Biophysical Journal*, *74*(), 1564-1578u

S. A. Syed Asif, K. J. Wahla and R. J. Colton (2001). Quantitative imaging of nanoscale mechanical properties using hybrid nanoindentation and force modulation. *Journal of Applied Physics*, *90*(3), 1192-1120

J. Zlatanovaa, S. M. Lindsay, and S. H. Leubac (2000). Single molecule force spectroscopy in biology using the atomic force microscope. *Progress in Biophysics* & *Molecular Biology*, *74*(), 37-61

E. Evans and K. Ritchie (1999). Strength of a Weak Bond Connecting Flexible Polymer Chains. *Biophysical Journal*, *76*(), 2439-2447

F. Schwesinger, R. Ros, T. Strunz, D. Anselmetti, H.-J. Guntherodt, A. Honegger, L. Jermutus, L. Tiefenauer, and A. Pluckthun (2000). Unbinding forces of single antibody-antigen complexes correlate with their thermal dissociation rates. *Proc. Natl. Acad. Sci. USA*, *97*(18), 9972-9977

T. Strunz, K. Oroszlan, R. Schafer, and H.-J. Guntherodt (1999). Dynamic force spectroscopy of single DNA molecules. *Proc. Natl. Acad. Sci. USA*, *96*(), 11277-11282

E.M. Lupton , C. Nonnenberg , I. Frank , F. Achenbach , J. Weis and C. Bräuchle (2005). Stretching siloxanes: An ab initio molecular dynamics study. *Chemical Physics, 414*(), 132-137

S. A. Syed Asif , K. J. Wahl and R. J. Colton (1999). Nanoindentation and contact stiffness measurement using force modulation with a capacitive load-displacement transducer. *Rev. Sci. Instrum, 70*(5), 2408-2413

W. C. Oliver and G. M. Pharr (1992). An improved technique for determining hardness and elastic modulus using load and displacement sensing indentation experiments. *Journal of Materials Research, 7*(6), 1564-1583

D. Abramovitch, S. Andersson, L. Pao, and G. Schitter (2007). A tutorial on the control of atomic force microscope. *Proceedings of American Control Conference, New York City, NY)*, (), 3499-3502

A. J. Fleming and S. O. R. Moheimani (2006). Sensorless Vibration Suppression and Scan Compensation for Piezoelectric Tube Nanopositioners. *IEEE Trans. on Control Systems Technology*, *14*(1), 33-44

Q. Zou and S. Devasia (2004). Preview-Based Optimal Inversion for Output Tracking: Application to Scanning Tunneling Microscopy. *IEEE Trans. on Control Systems Technology, 12*(3), 375-386

G. Schitter and A. Stemmer (2004). Identification and Open-Loop Tracking Control of a Piezoelectric Tube Scanner for High-Speed Scanning-Probe Microscopy. *IEEE Trans. on Control Systems Technology*, *12*(3), 449-454

G. Schitter, A. Stemmer, and F. Allgower (2003). Robust 2DOF-control of a piezoelectric tube scanner for high-speed atomic force microscopy. *Proceedings of American Control Conference (Denver, CO)*, (), 3720-3725

Ying Wu and Qingze Zou (2007). Robust-inversion-based 2DOF-control design for output tracking: Piezoelectric actuator example. *Proceedings of IEEE Conference on Decision and Control (New Orleans, LA)*, (), 2451-2457

Ying Wu and Qingze Zou (2007). Iterative Control Approach to Compensate for the Hysteresis and the Vibrational Dynamics Effects of Piezo Actuators. *Proceedings of American Control Conference (Minneapolis)*, (), 424-429

S. Salapaka, A. Sebastian, J. P. Cleveland, and M. V. Salapaka (2002). High bandwidth nano-positioner: A robust control approach. *Review of Scientific Instruments*, *73*(9), 3232-3241

D. Croft, G. Shedd, and S. Devasia (2001). Creep, Hysteresis, and Vibration Compensation for Piezoactuators: Atomic Force Microscopy Application. *Review of Scientific Instruments*, *123*(1), 35-43

M. Vanlandingham, S. McKnight, G. Palmese, J. Ellings, X. Huang, and T. B. (1997). Nanoscale indentation of polymer systems using the atomic force microscope. *Journal of Adhesion*, *64*(), 31-59

(2004). Dimension 3100 Manual, NanoScope software Version 5. *Journal of Adhesion*, (), 203-245

S. A. Chizhik, V. V. Gorbunov, I. Luzinov, N. Fuchigami, and V. V. Tsukruk (2001). Surface force spectroscopy of elastomeric nanoscale films. *Macromolecular Symposia*, *167*(), 167-175

A. Weisenhorn, M. Khorsandi, S. Kasas, V. Gotzos, and H.-J. Butt (1993). Deformation and height anomaly of soft surfaces studied with an AFM. *Macromolecular Symposia*, *4*(), 106-113

J.-N. Juang and M. Q. Phan (2001). Identification and Control of Mechanical Systems. *Identification and Control of Mechanical Systems*, Cambridge.

J. L. Hutter and J. Bechhoefer (1993). Calibration of atomic-force microscope tips. *Review of Scientific Instruments*, *64*(7),1868-1873

Heinrich. Hertz (1896). *Miscellaneous Papers; On the contact of elastic solids*,

K. S. K. Karuppiah, S. Sundararajan, Z.-H. Xu, and X. Li (2006). The effect of protein adsorption on the friction behavior of ultra-high molecular weight polyethylene. *Tribology Letters*, *22*(2),181-188

A. Mitchell and P. Shrotriya (2006). Onset of nanoscale wear of metallic implant materials: Influence of surface residual stresses and contact loads. *Wear*, *263*(7-12),1117-1123

K. Wahl, S. Asif, J. Greenwoodc, and K. Johnson (2006). Oscillating adhesive contacts between micron-scale tips and compliant polymers. *Journal of Colloid and Interface Science*, *296*(),178-188

H-W. Hu and S. Granick (1992). Viscoelastic Dynamics of Confined Polymer Melts. *Science*, *258*(5086),1339-1342

S. Granick, Z. Lin, and S. C. Bae (1992). Molecules squeezed and stroked. *Nature*, *425*(),467-468

J. D. Ferry (1980). *Viscoelastic Properties of Polymers.*, Wiley

C. White, M. VanLandingham, P. Drzal, N. Chang, and S. Chang (2005). Viscoelastic characterization of polymers using instrumented indentation. II. Dynamic testing. *Journal of Polymer Science Part B: Polymer Physics*, *43*(14),1812-1824

R. Horowitz, W. Messner, and J. B. Moore (1991). Exponential Convergence of a Learning Controller for Robot Manipulators. *IEEE Transactions on Automatic Control*, *36*(2),188-197

K. Krishnamoorthy and Tsu-Chin Tsao (2004). Iterative Learning Control Design Inspired by Repetitive Control. *IEEE Conference on Decision and Control*, (),

M. R. Graham and R. A. de Callafon (2006). An Iterative Learning Design for Repeatable Runout Cancellation in Disk Drives. *IEEE TRANSACTIONS ON CONTROL SYSTEMS TECHNOLOGY*, *14*(3),474-482

M. Verwoerda, G. Meinsmab, and T. de Vriesb (2006). On admissible pairs and equivalent feedback.-Youla parameterization in iterative learning control. *Automatica*, *42*(),2079 - 2089

Moore, Kelvin (1993). *Iterative learning control for deterministic systems*, Springer - Verlag, London

Jian-Xin Xu and Ying Tan (2003). *Linear and Nonlinear Iterative learning control*, Springer - Verlag, Berlin, New York

Gaspar, P. and Bokor, J. (1998). Iterative model-based mixed H_2 / $H\infty$ control design. *'98. UKACC International Conference*, *1*(),1-4

J. Ghosh and B. Paden (2002). A pseudoinverse-based iterative learning control. *IEEE Trans. on Automatic Control, 47*(5),831-836

Francois Padieu and Renjng Su (1990). An H_∞ Approach to Learning Control Systems. *International Journal of Adaptive Control and Signal Processing, 4*(),465-474

K. L. Moor, M. Dahleh, and S. P. Bhattacharyya (1992). Iterative Learnng Conrol: A Survey and New Results. *Journal of Robotic Systems, 9*(),563-594

Q. Zou, C. V. Giessen, J. Garbini, and S. Devasia (2005). Precision tracking of driving wave forms for inertial reaction devices. *Journal of Robotic Systems, 76*(),023701-023701-9

K.-S. Kim, Z. Lin, P. Shrotriya, and S. Sundararajan (2007). Iterative Control Approach to High-Speed Force-Distance Curve Measurement Using AFM: Time Dependent Response of PDMS. *UltraMicroScopy, 108*(9),911-920

Peter B. Goldsmith (2002). On the equivalence of causal LTI iterative learning control and feedback control. *Automatica, 38*(4),703-708

Kelvin L. Moor (1999). Iterative learning control–An expository overview. *Applied and Computational Controls, Signal Processing, and Circuits, 1*(),151-214

Guillaume T. Charras and Mike A. Horton,(2002). Determination of Cellular Strains by Combined Atomic Force Microscopy and Finite Element Modeling. *Biophysical Journal 83*(2)858-879

L. Ljung,(1999). *System identification* Springer Berlin / Heidelberg

K. Kim, and Q. Zou. (2008). A Model-less Inversion-based Iterative Control Technique for Output Tracking: Piezo Actuator Example. *Proceedings of American Control Conference, Seattle, WA, June 2008*, (), 2710-2715

Y. Li and J. Bechhoefer. (2008). Feedforward control of a Piezoelectric Flexure Stage for AFM. *Proceedings of American Control Conference, Seattle, WA, June 2008*, (), 2703-2709

M. Gardel, M. Valentine, and D. Weitz. (2005). *Microscale Diagnostic Techniques*, Springer-Verlag, Berlin

J. L. Hutter and J. Bechhoefer. (1993). Calibration of atomic-force microscope tips. *Review of Scientific Instrument*, *64*(7), 1868

N. Almqvist, R. Bhatia , G. Primbs , N. Desai , S. Banerjee and R. Laly. (2004). Elasticity and Adhesion Force Mapping Reveals Real-Time Clustering of Growth Factor Receptors and Associated Changes in Local Cellular Rheological Properties. *Biophysical Journal*, *86*( ), 1753-1762

Christian Rotsch and Manfred Radmacher. (2000). Drug-Induced Changes of Cytoskeletal Structure and Mechanics in Fibroblasts: An Atomic Force Microscopy Study. *Biophysical Journal*, *78*( ), 520-535

H. Suzuki and S. Mashiko. (1998). Adhesive force mapping of friction-transferred PTFE film surface. *Applied Physics A:Materials Science & Processing*, *66*( ), S1271-S1274

Marshall GW , Wu-Magidi IC , Watanabe LG , Inai N , Balooch M , Kinney JH and Marshall SJ. (1998). Effect of citric acid concentration on dentin demineralization, dehydration, and rehydration: Atomic force microscopy study. *Journal of Biomedical Material Research*, *42*( ), 500-507

M. Radmacher, J. P. Cleveland, M. Fritz , H. G. Hansma and P. K. Hansma (1994). Mapping Interaction Forces with the Atomic Force Microscope. *Biophysical Journal*, *6*(6), 2159-2165

David R. Baselta and John D. Baldeschwieler. (1994). Imaging spectroscopy with the atomic force microscope. *Journal of Applied Physics*, *76*(6), 33-8

Koleske, D. D., Lee, G. U., Gans, B. I., Lee, K. P., DiLella, D. P., Wahl, K. J., Barger, W. R., Whitman, L. J. and Colton, R. J. (1995). Design and calibration of a scanning force microscope for friction, adhesion, and contact potential studies. *Review of Scientific Instruments*, *66*(9), 4566-4574

B Cappella and P Baschieri and C Frediani and P Miccoli and C Ascoli. (1997). Improvements in AFM imaging of the spatial variation of force-distance curves: on-line images. *Nanotechnology*, *8*(), 82-87

Kyong-Soo Kim , Qingze Zou and Chanmin Su. (2008). A New Approach to Scan-Trajectory Design and Track: AFM Force Measurement Example. *Nanotechnology*, *130*(), 151005

K. K. Leang and S. Devasia. (2006). Design of hysteresis-compensating iterative learning control for piezo-positioners: application in atomic force microscopes. *Mechatronics*, *6*(), 141-158

Srinivasa M. Salapaka , Tathagata De2 and Abu Sebastian. (2005). A robust control based solution to the sample-profile estimation problem in fast atomic force microscopy. *INTERNATIONAL JOURNAL OF ROBUST AND NONLINEAR CONTROL*, *15*(), 821-837

Georg E. Fantner , Paul Hegarty , Johannes H. Kindt , Georg Schitter , Geraldo A. G. Cidade and Paul K. Hansma (2005). Data acquisition system for high speed atomic force microscopy. *Review of Scientific Instruments*, *76*(), 026118-1-4

Mark A. Lau and Lucy Y. Pao (2003). Input shaping and time-optimal control of flexible structures. *Automatica*, *39*(), 893-900

A. Serrani , A. Isidori and L. Marconi (2001). Semiglobal nonlinear output regulation with adaptive internal model. *IEEE Trans. on Automatic Control*, *46*(8), 1178-1194

Paul K. Hansma , Georg Schitter , Georg E. Fantner and Craig Prater (2006). APPLIED PHYSICS: High-Speed Atomic Force Microscopy. *Science*, *314*(5799), 601 - 602

Ying Wu , Qingze Zou and Chanmin Su (2008). A current cycle feedback iterative learning control approach to AFM imaging. *Proceedings of American Control Conference (Seattle, WA)*, (), 2040-2045

Hans-Jurgen Butta , Manfred Jaschkea and William Duckerb (2008). Measuring surface forces in aqueous electrolyte solution with the atomic force microscope. *Bioelectroehemistry and Bioenergetics*, *38*(), 191-201

Devasia, S., Chen, D. and Paden, B. (1996). Nonlinear Inversion-Based Output Tracking. *IEEE Trans. on Automatic Control*, *41*(7), 930-942

Devasia, S. and Paden, B. (1998). Stable inversion for nonlinear nonminimum-phase time-varyingsystems. *IEEE Trans. on Automatic Control*, *43*(2), 283-288

Devasia, S. and Paden, B. (2007). Precision preview-based stable-inversion for nonlinear nonminimum-phase systems: The VTOL example. *Automatica*, *43*(), 117-127

Zou, Q. and Devasia,S. (1999). Preview-Based Stable-Inversion for Output Tracking of Linear System. *ASME Journal of Dynamic Systems, Measurement and Control*, *121*(), 625-630